Thesis: Mengyang Qu (2025) "Fully Solution Processed Method to Fabricate ZnO Nanoparticles Devices for Sensing Application", University of Southampton, name of the University Faculty or School or Department, PhD Thesis, pagination.

University of Southampton

Faculty of Engineering and Physical Sciences

School of Electronics and Computer Science

Fully Solution Processed Method to Fabricate ZnO Nanoparticles Devices for Sensing Application

by

Mengyang Qu

ORCID ID 0009-0003-3685-8658

Thesis for the degree of Doctor of Philosophy

June 2025

University of Southampton

Abstract

Faculty of Engineering and Physical Sciences

School of Electronics and Computer Science

Doctor of Philosophy

Fully Solution Processed Method to Fabricate ZnO Nanoparticles Devices for Sensing Application

by

Mengyang Qu

This thesis presents a cost-effective, solution-based methodology for the fabrication of zinc oxide nanoparticles (ZnO NPs) devices aimed at pH sensing applications. ZnO NPs were dispersed in methanol and subsequently spin-coated onto glass substrates. Experimental results indicate that ZnO deposited directly from the solution is susceptible to defects, evidenced by a high sheet resistance of 10^10 Ω/□ in the absence of light, as well as sensitivity to environmental changes, low electrical stability, and vulnerability to water etching.

To mitigate these limitations, a novel processing technique involving exposure of ZnO to ultraviolet (UV) vacuum heating (UVVH) was developed. In pursuit of long-term stability, various polymers were evaluated as passivation materials, including polyvinyl alcohol/polydimethylsiloxane (PVA/PDMS) bilayers, ethylene-vinyl acetate (EVA), and ethylene-vinyl alcohol (EVOH).

The intrinsic high resistivity of ZnO NPs is attributed to ionized oxygen molecules adsorbed on the nanoparticle surface. These adsorbed oxygen molecules act to trap free electrons within the nanoparticle, serving as scattering centers that decrease both carrier concentration and mobility, thereby increasing film resistivity. The UVVH process effectively removes the ionized adsorbed oxygen molecules, while the passivation layer prevents re-adsorption, maintaining a low resistivity level for the ZnO NPs. This enhanced process yields resistivity values comparable to those achieved through traditional physical and chemical vapor deposition techniques.

The proposed method involves exposing the solution-processed ZnO NP film to 365 nm UV light and encapsulating it with an 80 μm layer of EVOH under vacuum conditions. The manufacturing process reaches a maximum temperature of 190 °C, making it suitable for flexible substrates such as polyimide. The resulting ZnO film exhibits a sheet resistance of 2.5×10^4 Ω/□ and a thickness of 2.35 μm. The EVOH passivation layer significantly enhances film stability, demonstrating resilience upon exposure to ambient conditions, with resistivity remaining consistent after 60 days.

Various thicknesses of EVOH passivation were also applied to evaluate their effects on the electrical stability of the nanoparticle films. The implementation of the UVVH process facilitates the production of a highly sensitive ZnO NP semiconductor pH sensor, wholly realized through a solution-based process that eschews high-energy consumption methods. The sensor exhibits diode-like electrical characteristics, with an increase in threshold voltage corresponding to decreases in the pH of the measured solution, yielding a sensitivity of 360 mV/pH. Maximum processing temperature is recorded at 120 °C, utilizing the UVVH technique.

The waterproof and oxygen-isolating polymer EVOH effectively passivates the ZnO NPs. The operational principle of the sensor, alongside its diode-like attributes, is closely linked to the adsorption of ionized oxygen molecules on the surface of the ZnO NPs. Furthermore, a mathematical model derived from the adsorption isotherm closely correlates with the experimental data. This fully solution-based manufacturing approach holds significant promise for applications in medical sensing and flexible wearable electronics.

Table of Contents

Table of Contents

Table of Tables

Table of Figures

Research Thesis: Declaration of Authorship

Print name: Mengyang Qu

Title of thesis:

I declare that this thesis and the work presented in it are my own and has been generated by me as the result of my own original research.

I confirm that:

1. This work was done wholly or mainly while in candidature for a research degree at this University;
2. Where any part of this thesis has previously been submitted for a degree or any other qualification at this University or any other institution, this has been clearly stated;
3. Where I have consulted the published work of others, this is always clearly attributed;
4. Where I have quoted from the work of others, the source is always given. With the exception of such quotations, this thesis is entirely my own work;
5. I have acknowledged all main sources of help;
6. Where the thesis is based on work done by myself jointly with others, I have made clear exactly what was done by others and what I have contributed myself;
7. Parts of this work have been published as:
   1. M. Qu, S. Yong, B. D. Rowlinson, A. A. Green, S. P. Beeby, H. M. H. Chong, and M. R. R. Planque, 'Solution-Processed Low Resistivity Zinc Oxide Nanoparticle Film with Enhanced Stability Using EVOH', *ACS Appl. Electron. Mater.*, May 2024, doi: 10.1021/acsaelm.4c00355.
   2. M. Qu, S. Yong, B. D. Rowlinson, A. A. Green, S. P. Beeby, H. M. H. Chong, and M. R. R. Planque, 'Solution-processed low resistivity zinc oxide nanoparticle film with enhanced stability using UV-Vacuum-Heat (UVVH) treatment and polyvinyl alcohol/ polydimethylsiloxane passivation', presented at The 50th MNE (Micro and Nano Engineering) International Conference (16/09/24 - 19/09/24), Sep. 2024.
   3. M. Qu, H. Dai, O. R. Kapur, S. P. Beeby, and H. M. H. Chong, 'Solution-Processed Diode-like ZnO Nanoparticle Device with Tunable Threshold Voltage and Super-Nernstian Ion Sensitivity', Small, p. 2504332, doi: 10. 1002/smll.202504332

Signature: ....Date:.........................

Acknowledgements

First, I thank my supervisors, Prof. Harold Chong and Prof. Steve Beeby, for their professional support and help. After Maurits passed away, you gave me the greatest help, so that I could get the results I never imagined. I also want to thank you, Maurits de Planque, for bringing me into the door of research. Although I will never see you again, I will never forget you.

Thanks to those who trained me. Dr. Abiodun Komolafe, thank you for teaching me to use the source meter. Dr. Daniel Newbrook, thank you for teaching me to use the Hall measurement and MEMS probe station. Dr. Junjie Shi, Dr. Yi Li, thank you for your consumables. Dr. Russel Torah, thank you for teaching me how to use chemicals properly. Dr. Sheng Yong, you taught me most of the things in PEM Lab. Thank you for your valuable advice on passivation materials. Dr. Tom Greig, thank you for teaching me how to use the dispensor printer. Thank you for your time and effort.

Amanda Green, thank you for your SEM images, they are really beautiful. Dr. Ben Rowlinson, thank you for your XPS measurements and thank you for helping me complete the publication. Dr. Huanghao Dai, thank you for the contact angle measurements. PhD students in SEMS and SET groups, Alexandar Todorov, Bingkai Ding, Boyuan Zhao, Yixuan Sun, it was nice to meet you.

Finally, thank you to my father, mother and Fanshu for your care and love. Without your encouragement and company, I would not be able to accomplish all this. Thank you for your greetings when I was tired and for your guidance when I was in trouble. Thank you very much.

Thus Spoke Mengyang Qu.

Definitions and Abbreviations

ZnO NPs	Znic oxide nanoparticles
UVVH	UV-vacuum-heating
PVA	Polyvinyl alcohol/polydimethylsiloxane
PDMS	Polydimethylsiloxane
EVA	Ethylene-vinyl acetate
EVOH	Ethylene-vinyl alcohol
IGZO	Indium gallium zinc oxide
PVD	Physical vapour deposition
CVD	Chemical vapour deposition
ALD	Atomic layer deposition
MOSFET	Metal oxide semiconductor field effect transistor
TFT	Thin film transistor
EDLT	Electrical double-layer transistor
ECT	Electrochemical transistor
TLM	Transfer Length Measurement
XPS	X-ray photoelectron spectroscopy
SEM	Scanning electron microscopy
FEP	Fluorinated ethylene propylene
DMSO	Dimethyl sulfoxide
$Ti(acac)_2$	Titanium diisopropoxide bis(acetylacetonate)

LR ZnO	Low-resistivity Zinc Oxide
HR ZnO	High-resistivity Zinc Oxide
PBS	Phosphate-buffered saline
SAW	Surface acoustic wave
APTES	(3-aminopropyl)triethoxysilane

List of publications arising from this work:

1. M. Qu, S. Yong, B. D. Rowlinson, A. A. Green, S. P. Beeby, H. M. H. Chong, and M. R. R. Planque, ‘Solution-Processed Low Resistivity Zinc Oxide Nanoparticle Film with Enhanced Stability Using EVOH’, *ACS Appl. Electron. Mater.*, May 2024, doi: 10.1021/acsaelm.4c00355.
2. M. Qu, S. Yong, B. D. Rowlinson, A. A. Green, S. P. Beeby, H. M. H. Chong, and M. R. R. Planque, ‘Solution-processed low resistivity zinc oxide nanoparticle film with enhanced stability using UV-Vacuum-Heat (UVVH) treatment and polyvinyl alcohol/ polydimethylsiloxane passivation’, presented at The 50th MNE (Micro and Nano Engineering) International Conference (16/09/24 - 19/09/24), Sep. 2024.
3. M. Qu, H. Dai, O. R. Kapur, S. P. Beeby, and H. M. H. Chong, ‘Solution-Processed Diode-like ZnO Nanoparticle Device with Tunable Threshold Voltage and Super-Nernstian Ion Sensitivity’, Small, p. 2504332, doi: 10. 1002/smll.202504332

Chapter 1

Introduction

Solution-processed electronics have raised great interest as an alternative fabrication method to replace the conventional cleanroom process [1]. These kinds of devices have the potential application in human-computer interface [2], point-of-care equipment [3], [4], wearable devices [5], and light-emitting devices [6]. This fabrication method can significantly simplify the process and reduce the cost during organic or inorganic material deposition. The solution-processed electronics technology can be used on some flexible substrates such as conductive textile and also some fixed substrates such as glass. With the development of printing technology, an increasing number of printed semiconductor devices are reported as research study, such as printed OLED on textile [7], supercapacitors as the energy storage[8], and thin-film transistors. Printed semiconductor device can use an organic channel layer, for example, (poly(3,4-ethylenedixothiophene)- poly(styrene sulfonate) (PEDOT:PSS)[9] [10], 2,7-dihexyl-dithieno[2,3-d;2',3'-d']benzo[1,2-b; 4,5-b']dithiophene (DTBDT-C6) [11]). For Printed Inorganic material channel layer, single-walled carbon nanotubes (SC-SWCNTs) [12], (In_2O_3 [13],[14],[15], IZO[16], IGZO[17], [18], ZnO[19], [20], [21]). Although some materials may require glove box processing, it provides a low-cost, low-temperature method with inherently lower environmental impact than cleanroom-processed films [1]. The choice of functional materials used in the deposited film is critical to its behavior and its suitability for solution processing. This thesis focuses on the area of solution-deposited inorganic semiconductor materials.

ZnO NPs, as an inexpensive, easy-to-synthesize, intrinsic n-type semiconductor material, has received extensive research attention and is a potential semiconductor biosensor material [22].

At the same time, studies in recent years have shown that solution-deposited nano-zinc oxide has also received widespread attention because of its simple and direct production process.

Before 2010, the main material for the channel layer is alloyed (IZO, IGZO). There was more pure metal oxide TFT reported after 2010 like In_2O_3 or ZnO. One of the possible reasons is that with the application and popularization of more efficient synthetic manufacturing methods [23], the fabrication cost of pure metal oxide is cheaper than before. Although the alloy has better electrical properties, it is more difficult to synthesize the alloy than pure metal oxide. With more development and research about metal oxide semiconductors, the properties of pure metal oxide semiconductors have been increased and the cost of fabrication has been decreased.

Most of the solution-processed metal oxide semiconductor devices are partially deposited from solution with lithography-determined electrodes [13], [14], [15]. The Indium oxide active layer and the gate dielectric was ink-jet printed but the drain, source, and gate electrodes were photolithography structures. The majority of the solution-processed deposition ZnO as a channel layer is spin-coating [20], [24], [25]. In 2019, José reported a full-screen printed ZnO field-effect transistor [21].

ZnO possesses a direct band gap of 3.37 eV and a significant free exciton binding energy, which facilitates effective photon absorption and exciton generation. From the previous study [25], the ZnO NPs would adsorb the oxygen molecules from the air, the oxygen molecules can trap the electrons from the nanoparticles and form the surface depletion layer, causing the high resistivity of the film. This adsorbed species is easily influenced by environmental factors such as light and moisture, leading to the unstable electrical properties of the nanoparticle film. UV light can temporarily remove the adsorbed oxygen molecules, but the nanoparticles can re-adsorb them in the atmospheric environment. This study presents a novel UV-vacuum-heating fabrication method (UVVH process) that involves exposing ZnO NPs to vacuum ultraviolet (VUV) radiation to promote the desorption of ionized oxygen molecules from the surface of ZnO NPs. To prevent exposure of the ZnO NPs to oxygen again, three encapsulation materials—ethylene-vinyl acetate (EVA), polyvinyl alcohol (PVA), and ethylene vinyl alcohol (EVOH)—were employed. The study highlights the significant impact of adsorbed ionized oxygen molecules on the resistivity of ZnO NPs films. By altering the types and thicknesses of applied passivation layers, the adsorption process can be further modulated, thus influencing the resistivity of ZnO NPs through the substances adsorbed on their surfaces. The findings reveal that, without a passivation layer, the resistivity of ZnO NPs increases markedly, with a dramatic surge—by a factor of 10^6—in resistivity observed just one day after UVVH treatment compared to immediately after the process. Conversely, ZnO NPs films with a thin EVOH passivation layer displayed a gradual increase in resistivity. As the thickness of the passivation layer increased, the rate of resistivity change decreased. Notably, with an 80 μm EVOH passivation layer, the resistivity remained stable after 60 days of storage in darkness. The results suggest that the resistivity of ZnO NPs can be controlled by regulating the amount of adsorbed ionized oxygen molecules on their surfaces. Given the ionized nature of oxygen adsorption, it is hypothesized that the surface charge of ZnO NPs influences both the adsorption and desorption of ionized oxygen molecules, thereby affecting resistivity. Furthermore, the surface charge of ZnO NPs changes in solutions with varying pH levels, indicating the potential application of UVVH-treated ZnO NPs as pH-sensing materials.

The pH value of human body fluids serves as a crucial biological indicator with significant implications for clinical diagnosis. The normal pH range of human blood is between 7.3 and 7.5. A pH level below 7.3 is indicative of acidosis, while a pH level above 7.5 suggests alkalosis [26]. In the context of cancer diagnosis, the extracellular environment of cancerous cells exhibits a slightly lower pH than normal cells due to its acidic nature The pH of the human body serves as a valuable indicator for diagnosing chronic diseases. For instance, chronic wounds exhibit a more alkaline pH than healthy skin. This alteration is attributed to the proliferation of bacteria and mold within the wound environment [27]. Nonetheless, the sensitivity of traditional pH sensors is limited by the Nernst limit (59 mV/pH), which can restrict diagnostic efficacy. Consequently, overcoming the Nernst limit to develop high-sensitivity pH sensors has garnered considerable research interest.

Due to their distinctive physical and chemical properties, ion-sensitive metal oxides exhibit considerable potential for application in pH sensing. These materials can adsorb charges on their surfaces in solution, resulting in a surface potential that is contingent upon ion concentration. Additionally, they are characterized by chemical stability, biocompatibility, and cost-effective manufacturing, facilitated by environmentally friendly synthesis processes. In the field of pH sensors, their high surface area-to-volume ratio enhances ion adsorption from the solution, thereby improving sensitivity [28]. Recent advancements have focused on developing pH sensors that utilize metal oxides, such as ZnO [29], RuO_2 [30], WO_3 [31] and IrO_2 [32] as sensing layers.

Compared with other metal oxides, ZnO is a common substance in the earth's crust and has low toxicity, is recyclable, and is easy to synthesize. As an ion-sensitive metal oxide, ZnO is also a promising material for pH measurement in solutions, which serves as a crucial indicator in medical diagnostics. [29], [33], [34], [35] However, the sensitivity of conventional ZnO pH sensors is also constrained by the Nernst limit of 59 mV/pH [29], [34]. Studies have indicated that this Nernst limit can be surpassed by employing field-effect transistors[36] or charge-coupled devices [37]. However, these methods typically involve complex structures and manufacturing processes. Previous research suggests incorporating nanoparticles can increase the number of active surface sites in pH sensors, subsequently enhancing sensitivity [35]. ZnO NPs thin films are characterized by convenient synthesis, safe manufacturing practices, and cost-effectiveness [38].

Various techniques exist for depositing ZnO, including but not limited to atomic layer deposition (ALD) [39], sputtering [40], spin-coating [41], [42] and printing [43], [44]. Nonetheless, achieving ZnO films with superior properties often necessitates relatively high temperatures (exceeding 300 °C) [43] or stringent fabrication conditions such as vapor deposition [45]. Among the various methods employed, solution-processed technology is recognized as a cost-effective and efficient deposition technique. In this approach, the target substance is dissolved or dispersed in an appropriate solvent and subsequently deposited onto the selected substrate using printing or spin coating methods. In contrast to conventional vapor deposition techniques, the solution-processed deposition of ZnO NPs does not impose stringent requirements regarding the deposition environment or energy consumption. While solution-processed ZnO NPs are straightforward and compatible with diverse substrates, the resulting films generally exhibit high electrical resistivity and low electrical stability [41]. To date, there are no reports of pH sensors utilizing ZnO NPs that exceed the Nernst limit.

1.1 Research Aim and Objectives

The main aim of this study is to develop a low-cost and high-performance solution-based ZnO NPs device fabrication method for detecting pH levels in the medical device field. Furthermore, as the study progresses, the ZnO NPs fabricated from the UVVH process show diode-like behavior, and this diode-like device can be used as the pH sensor whose sensitivity is beyond the Nernst limit. This finding also provides another possible direction for the study, which is to develop a wearable human health detector.

In order to achieve the main aim, the following objectives were formulated.

1. Develop a method to optimize the electrical property of solution-processed ZnO NPs. The as deposited ZnO NPs films show the resistivity at the level of 10^6 Ω·cm. The targeted resistivity is at the range between 10^0 to 10^3 Ω·cm to ensure the sensor can operate at least at currents in the microampere range.

2. Develop a passivation method that does not require a clean room process to ensure that the ZnO NPs device can work in different pH solution environments (pH 9 -4).

3. Ensure that the ZnO NPs deposited by this method have sufficient stability to work for at least 5 pH values.

4. Realise the super-Nernst limit (beyond 59 mV/pH) detection of different pH level solutions by the sensor

1.2 Statement of Novelty

This thesis has achieved the following novelty:

1. A new fabrication technology was developed to obtain high-performance ZnO by exposing nanoparticles to a UV-vacuum-heating environment (UVVH), to reduce the resistivity of the ZnO NPs film.

2. Realised the long-term stability of ZnO NPs through polymer (EVOH) film packaging. The device has low resistivity (5.8 Ω·cm), which is one million times smaller than the as-deposited film. The low resistivity status can be kept for at least 60 days in an ambient environment.

3. Fabricate a diode-like ZnO NPs device using UVVH process and the EVOH passivation. The device shows an on/off ratio of 10^5. The diode-like behaviour is achieved by modulating the surface adsorption of the oxygen molecules, and this has never been reported before.

4. The diode-like ZnO NPs device can work as pH sensors with threshold voltage shifts under different pH conditions. The sensitivity is 360 mV/pH and beyond the Nernst limit. The current value follow-through device was modelled by a combination of electrical and absorption equations and fitted with the experimental data.

1.3 Thesis Structure

This thesis can be mainly divided into the following parts.

Chapter 2 is mainly about the literature review. The parts mentioned in the second chapter mainly include the fabrication methods of ZnO NPs, the methods of semiconductor deposition by solution and their possible device applications, solution composition and their specific functions, different printed electronic technologies and methods for the characterization of semiconductors. Besides, the oxygen adsorption mechanism is also included in.

Chapter 3 mainly talks about the specific experimental fabrication process, including the composition of the ZnO NPs solution, the material of the silver electrode and the printing process. The most important part of the third chapter is to introduce a new manufacturing process to improve the performance of ZnO NPs by vacuum UV exposure (UVVH), as well as its passivation materials. The process for diode-like ZnO NPs pH sensor will also be introduced.

Chapter 4 introduces the electrical properties of the UVVH-treated ZnO NPs and their stability by passivating different materials. The method includes SEM, XPS, hall measurement, transfer length measurement, IV measurement and long-time stability measurement. The results from three passivation materials EVA, PVA and EVOH will be introduced. The fabricated ZnO film has a sheet resistance of 2.5 x 10^4 Ω/□ and a thickness of 2.35 μm. The EVOH passivation layer enhanced film stability, protecting it when exposed to the ambient environment. The resistivity of the ZnO NPs layer with EVOH passivation remains unchanged after 60 days in the ambient environment.

Chapter 5 introduces the characterization of the ZnO NPs pH sensor. The sensor demonstrates diode-like electrical characteristics, with its threshold voltage increasing as the pH of the measured solution decreases, yielding a sensitivity of 360 ± 11 mV/pH. The maximum processing temperature is 120°C, and the manufacturing procedure employs a UV-vacuum-heating (UVVH) technique. The working principle of the sensor, as well as its diode-like characteristics, are also included Finally, the mathematical model derived from the adsorption isotherm effectively correlates with the experimental data.

Finally, the conclusions and the future work are in chapter 6.

Chapter 2

Literature Review

Introduction

This chapter provides a comprehensive summary of the pertinent literature at this research stage. Key topics covered include the solution deposition method for semiconductor fabrication and related manufacturing processes, advancements in printed electronics technology, significant device applications, and the effects of UV ray absorption by ZnO NPs. Additionally, the characterisation techniques for semiconductor materials, including Hall measurements and Transfer Length Measurement (TLM) analysis, are discussed. Given that the primary application of solution-deposited semiconductors at this stage is in the fabrication of transistors, related device technologies are also presented in this chapter.

Nanostructured ZnO is recognized as a low-toxicity and sustainable semiconductor material with significant applications in electronic devices, including transistors [46], [47], ultraviolet (UV) photodetectors [48] and memristors [49], [50], [51]. Its appeal in semiconductor electronics arises from its wide bandgap, thermal stability, and high carrier mobility [38], [52]. In addition, ZnO exhibits considerable potential in sensing applications, such as gas sensors [53], [54], attributable to its excellent electrical properties and elevated surface-to-volume ratio [33]. ZnO is also a promising material for pH measurement in solutions, which serves as a crucial indicator in medical diagnostics [29], [33], [34], [35]. However, the sensitivity of conventional ZnO pH sensors is also constrained by the Nernst limit of 59 mV/pH [29], [34]. Notably, studies have indicated that this Nernst limit can be surpassed by employing field-effect transistors [36] or charge-coupled devices [37]; however, these methods typically involve complex structures and manufacturing processes. Previous research suggests incorporating nanoparticles can increase the number of active surface sites in pH sensors, subsequently enhancing sensitivity [35]. ZnO NPs thin films are characterized by convenient synthesis, safe manufacturing practices, and cost-effectiveness [38].

Various techniques exist for depositing ZnO, including but not limited to atomic layer deposition (ALD) [39], sputtering [40], spin-coating [41], [42] and printing [43], [44]. Nonetheless, achieving ZnO films with superior properties often necessitates relatively high temperatures (exceeding 300 °C) [43] or stringent fabrication conditions such as vapour deposition [45]. Among the various methods employed, solution-processed technology is recognized as a cost-effective and efficient deposition technique. In this approach, the target substance is dissolved or dispersed in an appropriate solvent and subsequently deposited onto the selected substrate using printing or spin coating methods. In contrast to conventional vapour deposition techniques, the solution-processed deposition of ZnO NPs does not impose stringent requirements regarding the deposition environment or energy consumption. While solution-processed ZnO NPs are straightforward and compatible with diverse substrates, the resulting films generally exhibit high electrical resistivity and low electrical stability [41]. To date, there are no reports of pH sensors utilising ZnO NPs that exceed the Nernst limit.

2.1 Vapor Deposition

Traditional deposition methods are classified into two categories: physical vapor deposition (PVD) and chemical vapor deposition (CVD)

PVD primarily involves the conversion of a material into a vapor phase, followed by its transfer to a substrate to achieve deposition or coating. The predominant methods for material excitation in PVD are evaporation and sputtering. Evaporation entails the conversion of the material into vapor through high-temperature heating, whereas sputtering involves bombarding the target material with ionized gas, resulting in the ejection of its atoms or molecules. While PVD is widely utilized across various applications, it is generally more challenging to control the uniformity of the films produced compared to those obtained via CVD [55]. A simplified PVD (sputtering) diagram is shown in **Figure 2.1**. Argon ions bombard the target material to generate sputtered atoms, which diffuse to the substrate surface and deposit on it.

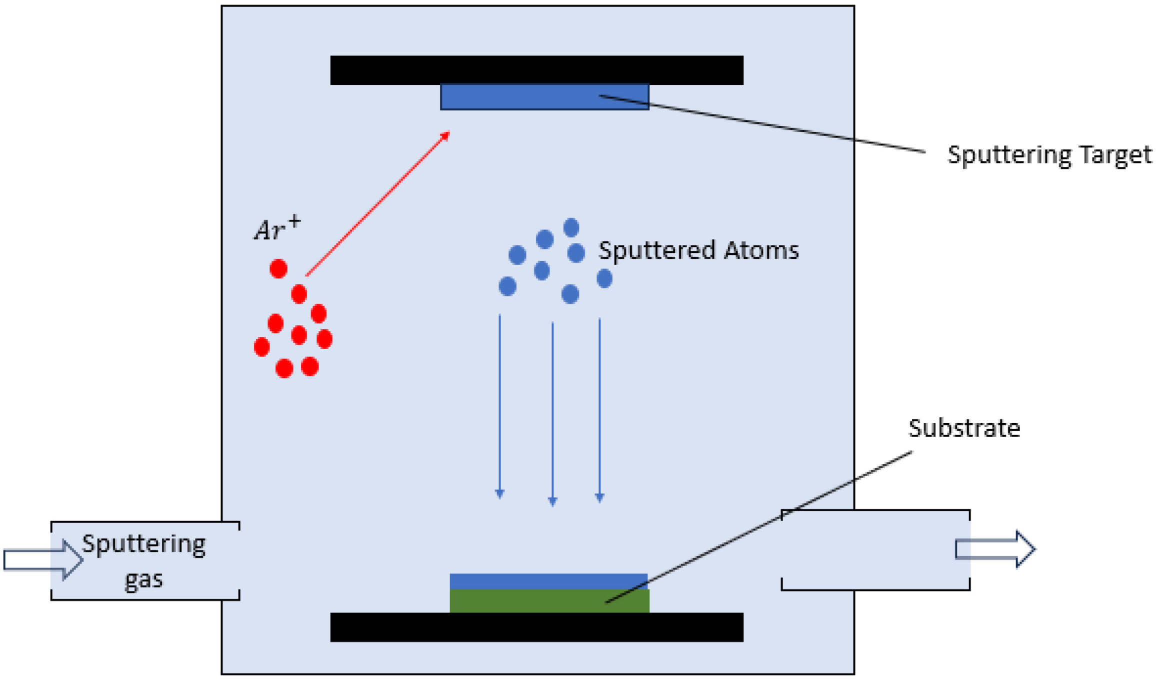

Figure 2.1: Diagram illustration for PVD process reproduced from [55].

The fundamental principle of CVD involves exposing the substrate to gaseous precursors of the target material, facilitating the deposition of the material on the substrate surface via chemical reactions. Under controlled temperature and pressure conditions, the precursors undergo synthesis or decomposition reactions on the substrate, resulting in the formation of deposits that adhere to the substrate surface, thus completing the deposition process [56]. Compared to PVD, films produced via CVD tend to exhibit greater uniformity. However, the involvement of chemical reactions in the deposition process may lead to longer deposition times. Furthermore, due to the need for precise control over the reaction conditions, the CVD process and the associated equipment can be comparatively more complex. Additionally, the requirement for specific precursors may influence the overall fabrication process. During the chemical reaction, various by-products are generated; while most of these by-products are typically removed by the airflow, they may still impact the final fabrication outcomes.

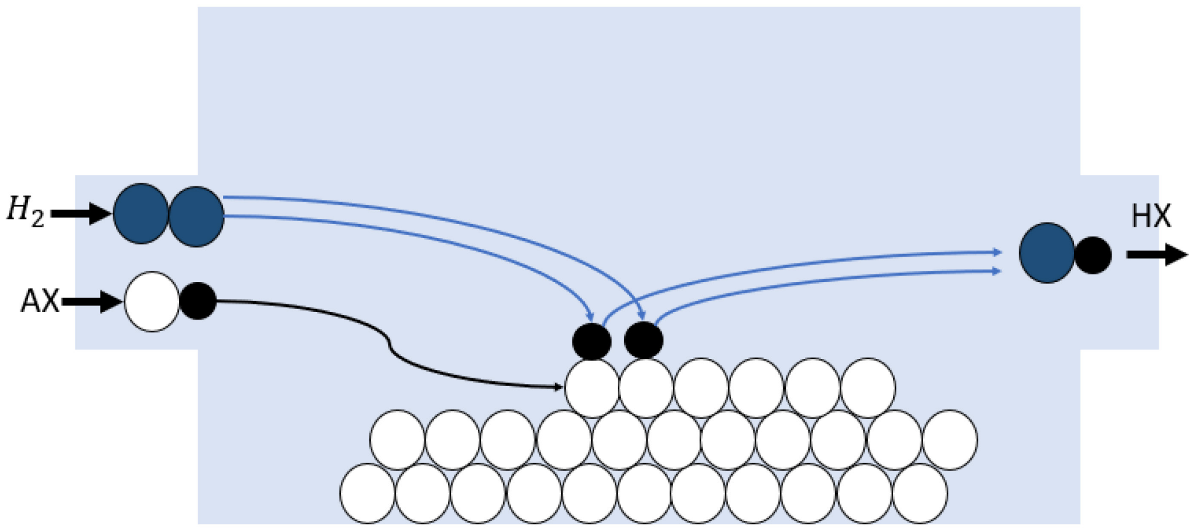

Figure 2.2: The basic principles of CVD are derived from [56]. H_2 represents the hydrogen gas and AX represents the precursors of material A, and HX represents the additional substances generated during the deposition process.

As shown in **Figure 2.2**, the principle of CVD was presented. The substance AX is the precursor of solid A. In the reaction chamber, hydrogen reacts with AX to generate HX gas and A precipitate. The A precipitate is deposited on the substrate, and the HX gas leaves the reaction chamber with the gas flow, thus completing the deposition process.

2.2 Solution-processed deposition

The deposition of semiconductors via solution processes primarily involves the dispersion of semiconductor materials into appropriate solvents, which may include organic solvents or water. This mixture is subjected to thorough homogenization through techniques such as ultrasonic vibration, heating, or mechanical stirring. Following this, the resultant ink is uniformly applied to the substrate using methods such as spin coating or printing, and subsequently dried.

For organic semiconductor materials, it is imperative to maintain the annealing temperature below 100°C to prevent thermal degradation that could compromise their semiconducting properties. In contrast, inorganic metal semiconductors can theoretically withstand annealing temperatures exceeding 1000°C [57]. However, in practice, most researchers opt to restrict the annealing temperature to below 500°C to minimize energy consumption during the manufacturing process.

The solution-based deposition method offers several advantages, including cost-effectiveness, high efficiency, and recyclability. The synthesis of nanoparticles within this framework is predominantly categorized into two methodologies: bottom-up and top-down approaches [57]. The top-down approach involves the reduction of larger particles into nanoscale dimensions through physical extrusion. However, due to its significant energy requirements, this method has garnered limited attention. Conversely, the bottom-up approach facilitates the assembly of nanoparticles by integrating various atoms via chemical reactions, which can occur in either solvent-based or vapor environments. The lower energy demands associated with atom integration have led to increased research interest in this technique. An overview of the process is illustrated in **Figure 2.3**.

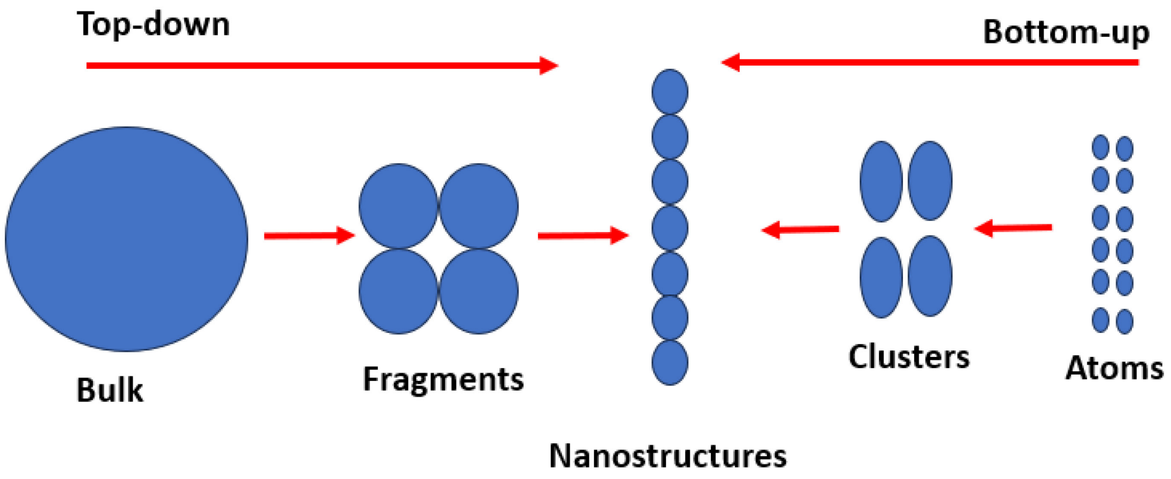

Figure 2.3: The metal oxide fabrication process for both bottom-up and top-down reproduced from [57].

It is not a specific type of semiconductor shown in **Figure 2.3**, just used to distinguish the deposition and aligned method from the conventional fabrication process. The solution process has a relatively direct fabrication process in comparison with photolithography and etching. Most of the solution-processed semiconductor is using intrinsic doping material such as some organic polymer or some metal oxide. Organic material is more reported as the channel layer than the inorganic material from the latest report.

There are two main methods for the synthesis of zinc oxide solution: direct mixing of nanoparticles and synthesis with precursors. Synthesizing directly with nanomaterials is the simplest and most direct way. It is by mixing a certain proportion of nano-zinc oxide particles into the organic solvent and stirring evenly by means of ultrasonic vibration. Synthesis via precursors can be divided into two directions:

1. Use Zinc acetate dihydrate (Zn(CH3COO)2·2H2O) [58]
2. Use Amminehydroxo zinc aqueous solution Zn(OH)2(NH3)x [59]

The first process is in organic solution. The second process is all in water. The stirring time is very long. Most of the reported times are more than 10 hours.

In terms of the deposition method, there are two major types which are spin coating and printing. Most of the ZnO nanoparticle semiconductors was using spin coating because it can produce a better morphological property. But Liu reported that after three times of inkjet printing, they achieve the same property with spin coating ZnO layer transistor [60]. The geometric properties of the printed work also depend on the resolution of the printer. During the printing process, the layer can be cured by directly heating or precursor reaction.

2.2.1 Metal oxide nanoparticle semiconductor functional layer by direct deposition or precursor deposition

Precursor deposition primarily involves the chemical reaction of two or more substances to achieve the desired deposit. For ZnO deposition, ZnO is typically synthesized by reacting zinc acetate with an alkali followed by heating [59]. Theoretically, precursor deposition can produce homogeneous films; however, a potential downside is the presence of impurities arising from incomplete reactions.

In metal oxide nanoparticle semiconductors, current flows only between adjacent particles. The n-type conductivity observed in metal oxide semiconductors is attributed to oxygen vacancies within the metal lattice, which exhibit three charge states: 0, +1, and +2. These charge states are influenced by the length and angle of the metal-oxygen bond. For instance, in ZnO lattices, an oxide vacancy with a +2 charge state is 26% more outward than one with a neutral state [52].

Most metal oxide transistors employ metal drain and source electrodes to create a Schottky barrier. When a gate bias is applied, the semiconductor's conduction band minimum decreases, reducing the barrier enough to permit current flow through the channel. However, such transistors face challenges, preventing them from fully meeting industry standards. Two primary issues are hysteresis and the variation of the threshold voltage.

During both forward and backward bias scanning of these transistors, varying drain currents are generated in the channel, as demonstrated in **Figure 2.4**. This behavior, known as hysteresis, was reported by Vidor as being caused by charged groups in the dielectric material, such as hydroxyl groups [25]. As depicted in **Figure 2.5**, in the absence of gate bias, hydroxyl groups remain non-polarized. Some molecules migrate to the surface, attracting electrons in the nanoparticle layer and causing electron trapping in the channel. Upon application of gate bias, generated holes migrate to the surface, releasing adsorbed hydroxyl groups and consequently freeing trapped electrons within the channel layer, thereby enhancing conductivity. The polarization of hydroxyl groups occurs gradually, leading to transistor hysteresis. **Figure 2.6** shows the specific structure of this transistor with hysteresis properties. PVP stands for Polyvinylpyrrolidone, a water-soluble polymer dielectric material. This hysteresis effect is not only reflected in transistors. Based on Greenham et. al, [61] applying varying offset voltages to both ends of ZnO NPs influences the adsorption and desorption dynamics of ionised oxygen molecules on their surface. This phenomenon is hypothesized to result from the migration of positively charged oxygen vacancies within the ZnO NPs under the applied bias voltage. This migration modulates the surface adsorption charges, consequently altering the resistance of the ZnO NPs. Moreover, the annealing temperature is noted to significantly affect electron trapping under natural conditions. The higher annealing temperature usually shows high current and less hysteresis [21].

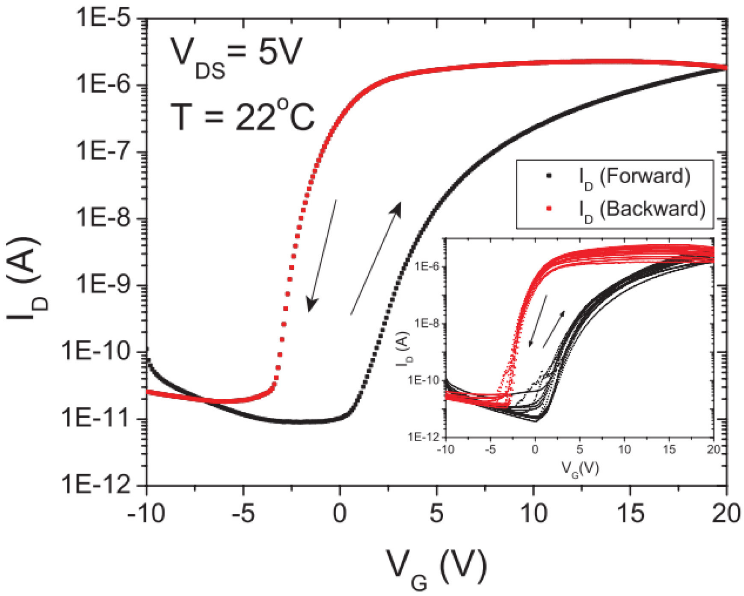

Figure 2.4: The IV curve shows the hysteresis phenomenon of ZnO NPs transistor [25]. After the forward bias, the PVP dipoles were polarised and release the trapped electron and causing the high current level.

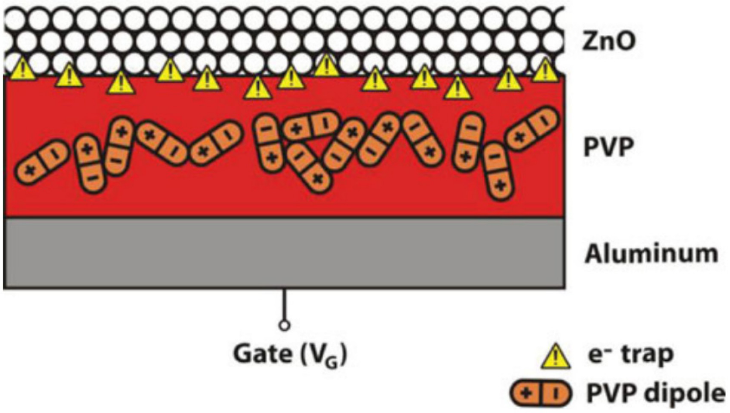

Figure 2.5: A bottom gate structure ZnO nanoparticle transistor with PVP as the dielectric layer and aluminium as the electrode [25]. Polyvinylpyrrolidone, a water-soluble polymer dielectric material.

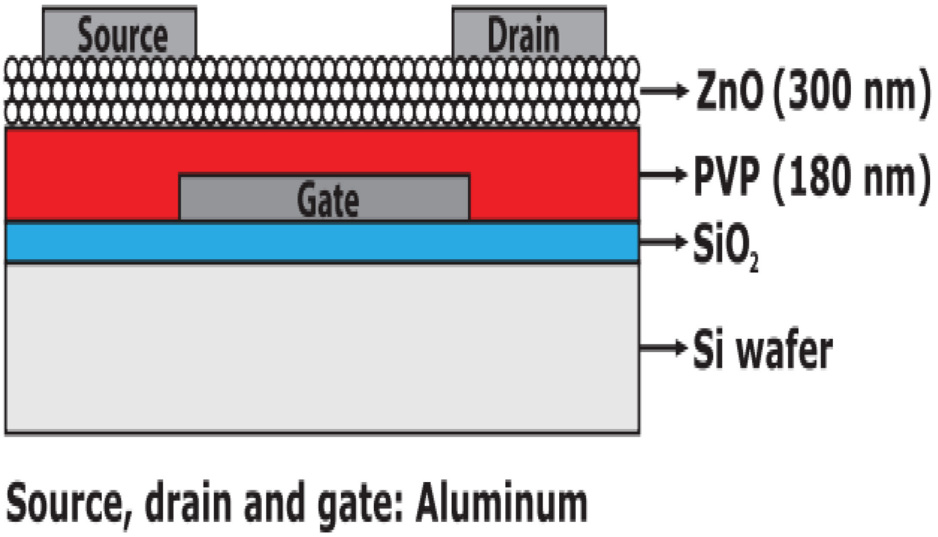

Figure 2.6: The full structure of the ZnO nanoparticle transistor [25]**.**

The annealing temperature plays a critical role in the performance of functional layers. To enhance performance, a higher temperature is necessary during the fabrication process. Marques reported a fabrication method for printing a logic gate utilizing indium oxide as the channel layer [15]. Their work necessitates an annealing temperature of 400°C to convert the precursor into the semiconductor layer. The required annealing temperature can be decreased by utilizing nanoparticles directly. Carvalho reported that an increased weight percentage of ZnO can effectively reduce the annealing temperature [21]. They reported that a film transistor constructed with 40% weight ZnO nanoparticles, when annealed at 150 °C, exhibits properties comparable to those of a film with 15% ZnO annealed at 400 °C.

The underlying cause of the threshold voltage shift remains inadequately understood, as it tends to change with prolonged use of the transistors. Akrofi et al. [22] have reported a method to mitigate this issue by employing a three-layer dielectric stack to eliminate threshold voltage shifts. However, the fabrication process outlined in their study relies on conventional lithography, which is more complex than direct printing methods.

2.2.2 Solution-processed organic semiconductor functional layer.

Solution-Processed organic semiconductor transistors are more commonly reported than their inorganic counterparts. Similar to inorganic printed transistors, organic transistors also employ Schottky barrier junctions to achieve their structural configurations. Typically, carbon or metal is utilized as the drain and source electrodes, while polymer compounds serve as the semiconductor material. The ease of processing carbon-based polymers, which can be cured at low temperatures, contributes to their widespread use in printed transistor research. These transistors have been reported in various applications, including sensors, logic gates, and amplifiers. Kanh introduced an electrolyte-gated transistor designed for glucose sensing [62]. Singh reported a printed dual-gated transistor used as logic or gate [11].

2.3 Electronic Printing Technology: a method for solution-processed deposition

For solution-processed semiconductor devices, inkjet printing is the most commonly utilised deposition method due to its higher resolution and lower operational complexity. The resolutions associated with various printing techniques are presented below.

Table 2.1: Resolution of different printing techniques [1].

Printing Method	**Resolution (μm)**	**Speed (m/min)**	**Thickness (μm)**	**Viscosity (mPa·s)**
Inkjet printing	0.4 - 50	1 – 100	0.3 – 20	1 - 40
Transfer printing	0.1 – 90			
Screen printing	50 – 100	10 – 100	3 – 100	500 – 50000
Gravure printing	20 – 75	20 – 1000	0.1 – 5	1 – 200
Knife coating	50 – 100	1 – 10	0.1 – 5	1 – 200

The data presented in the table indicate that the accuracy of the majority of printing technologies does not surpass 1 μm. Furthermore, with the exception of screen printing, these technologies do not necessitate highly viscous solutions.

2.3.1 Ink-jet printing

As described in **Figure 2.7**, inkjet printing involves using a computer to design the device structure, which is then printed through a nozzle, similar to traditional commercial printers. This process, known as drop-on-demand, allows ink droplets to be expelled based on signals from a computer program. There are two primary methods for ejecting ink droplets from the nozzle. The first method employs heating to create a bubble that forces the ink out, while the second method utilizes a piezoelectric element to press the ink out of the nozzle.

The primary advantage of inkjet printing lies in its high precision; however, it is also associated with significant drawbacks, particularly in terms of cost. For the Dimatix inkjet printer, the cartridges are typically designed by manufacturers for single use and cannot be reused, leading to high expenses associated with cartridge replacement.

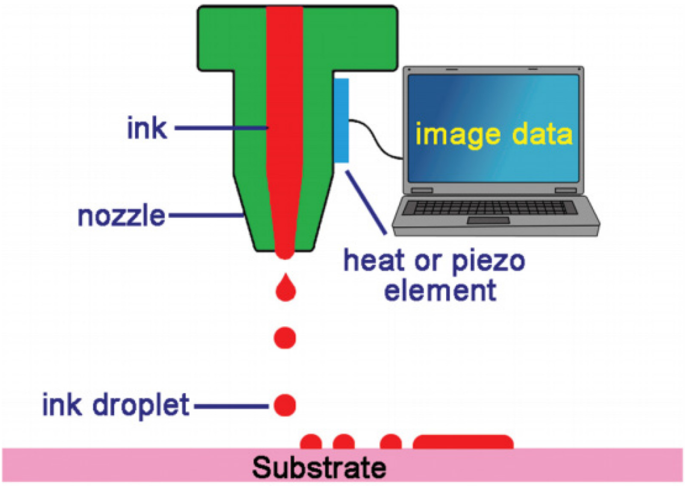

Figure 2.7: Process of inkjet printing [63].

Several types of electronic devices fabricated by the inkjet printer were reported. Whittow et, al. [64] proposed a inkjet printed antennas deposited on textile. The antennas was printed on a pre-deposited interface layer aching an efficiency of 53%. Li et, al. [65] proposed a fully inkjet printed capacitor. The PVP dielectric material was used to for the insulator layer. The ink was cured by UV light after printing and exhibit good insulating behaviour.

2.3.2 Screen printing

Screen printing typically offers lower resolution compared to inkjet printing. **Figure 2.8** shows the fundamental process involving using a pre-designed mesh as a mask positioned over the substrate, onto which the ink material is poured. A squeegee is then employed to press the ink through the mesh, facilitating its deposition onto the substrate. The ink is subsequently cured through either oven heating or UV exposure. This process is repeated until all device structures are fully realized.

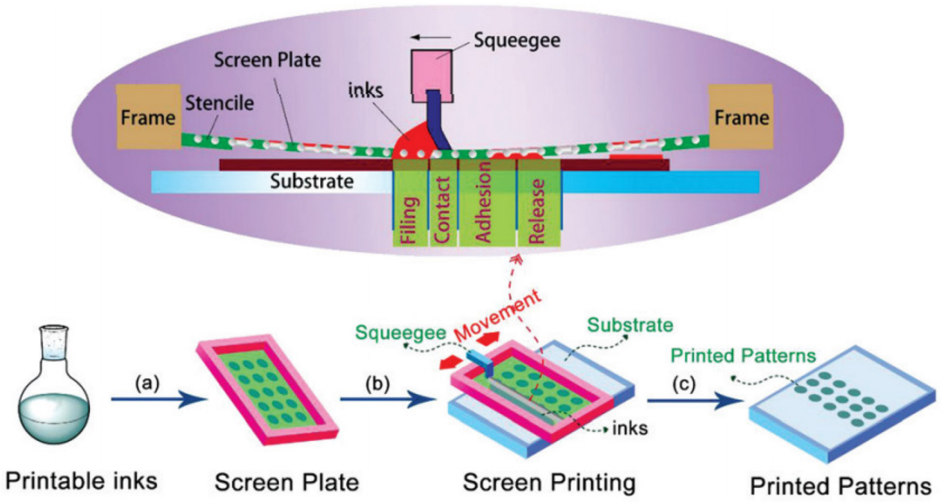

Figure 2.8: The working principle of screen printing entails the following steps a) preparation of the ink from precursors or bulk materials; b) fixation of the screen template onto the substrate, followed by the use of a squeegee to press the ink through the template according to the designed structure; c) post-annealing of the ink to form the desired layer [63].

Figure 2.9 shows the a fully screen-printed transistor [21]. The carbon electrode was printed on the flexible substrate as the interdigitated structure forming source and drain electrodes. Secondly, a ZnO NPs layer were printed on the top of the carbon electrode working as the active semiconductor layer. Then, the solid electrolyte layer was printed on the top of the ZnO NPs layer to generate the dielectric layer. Finally, the silver gate electrode was printed on the top of the electrolyte dielectric layer.

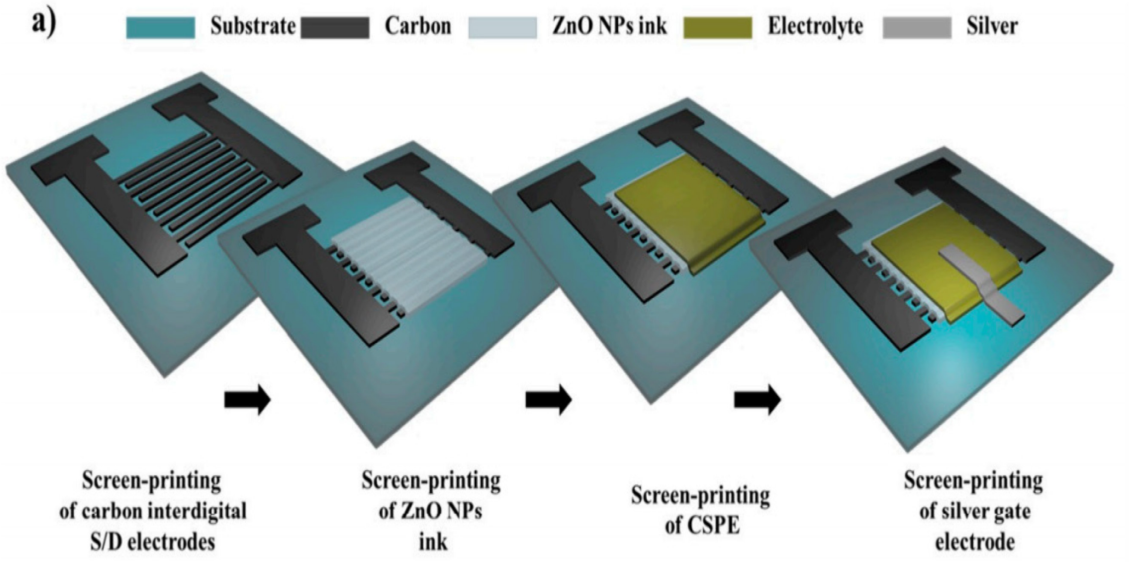

Figure 2.9: The structure of the fully screen-printed ZnO FET [21].

2.3.3 Dispenser printing

Similar to inkjet printing, dispenser printing is a computer-controlled printing method; however, it can process inks with significantly higher viscosities. In principle, the viscosity range for dispenser printing can reach up to 10^6 mPa·s [66]. However, dispensing printing has a lower resolution. The highest resolution of dispensing is around 100 micrometres.

As depicted in **Figure 2.10**, the system comprises two main components: the air compressor and the robotic arm holding the syringe. The air compressor facilitates ink ejection through the needle onto the substrate. The computer program controls the robotic arm to produce the device figure. The resolution of the printed work is contingent upon the inner diameter of the needle and the accuracy of the robotic arm, which typically measures hundreds of micrometres. During the printing, because the diameter of the needle is hundreds of micrometres, the solvent at the edge of the needle quickly evaporates, leading to the blockage of fluid flow. The oil-based solvent is preferred over the water-based solvent in this printing system to avoid this unwanted phenomenon. Besides, to prevent the unintended deposition of low-viscosity ink onto the substrate, the air pump can also generate a vacuum above the ink, effectively lifting it.

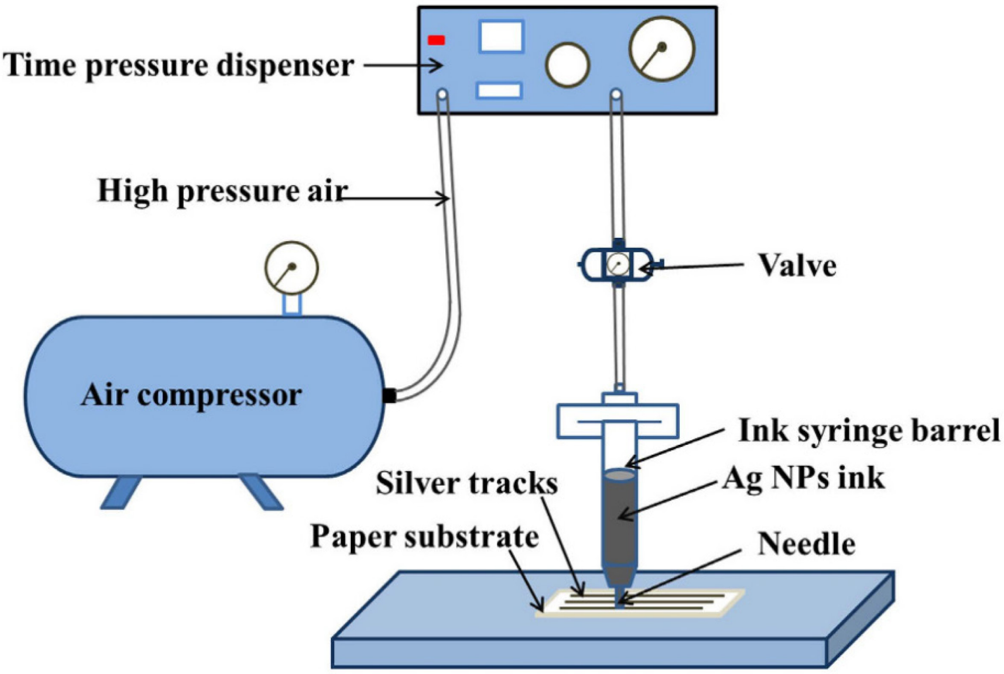

Figure 2.10: The pneumatics dispenser printer system [67].

Chen et al. [44], proposed a fully dispenerosolrer printed memristor with Ag /ZnO/ Ag structure. The silver electrodes were printed on the glass substrate with a 1 mm gap between them. Then, the ZnO NPs ink was printed on the silver electrode as a dispenser, followed by a second silver electrode printed on the ZnO NPs layer. The structure is shown in **Figure 2.11.** It shows volatile characteristics and can be applied in artificial synapses as short-term memory devices. Meijing et al. [68] proposed a fully dispenser-printed device structure for healthcare applications. The structure was printed on the textile as a wearable device. The fabrication process is shown in **Figure 2.12.** The structure contains an interface layer on the textile to form the substrate layer, avoiding ink penetration through the textile. Then, the silver conductive track was printed on the interface layer, followed by an encapsulation layer printed on its top to protect it. Finally, a carbon pad was printed on the encapsulation layer, forming the skin contact. The structure was proposed as the potential solution for a bio-signal monitor.

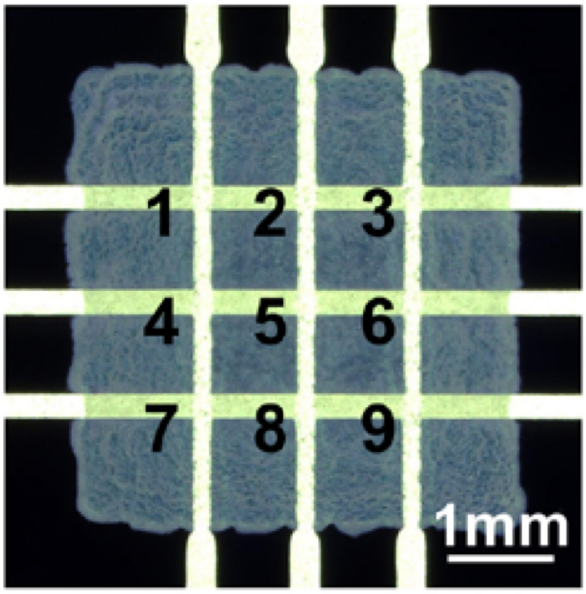

Figure 2.11: A fully dispenser-printed memory device [44].

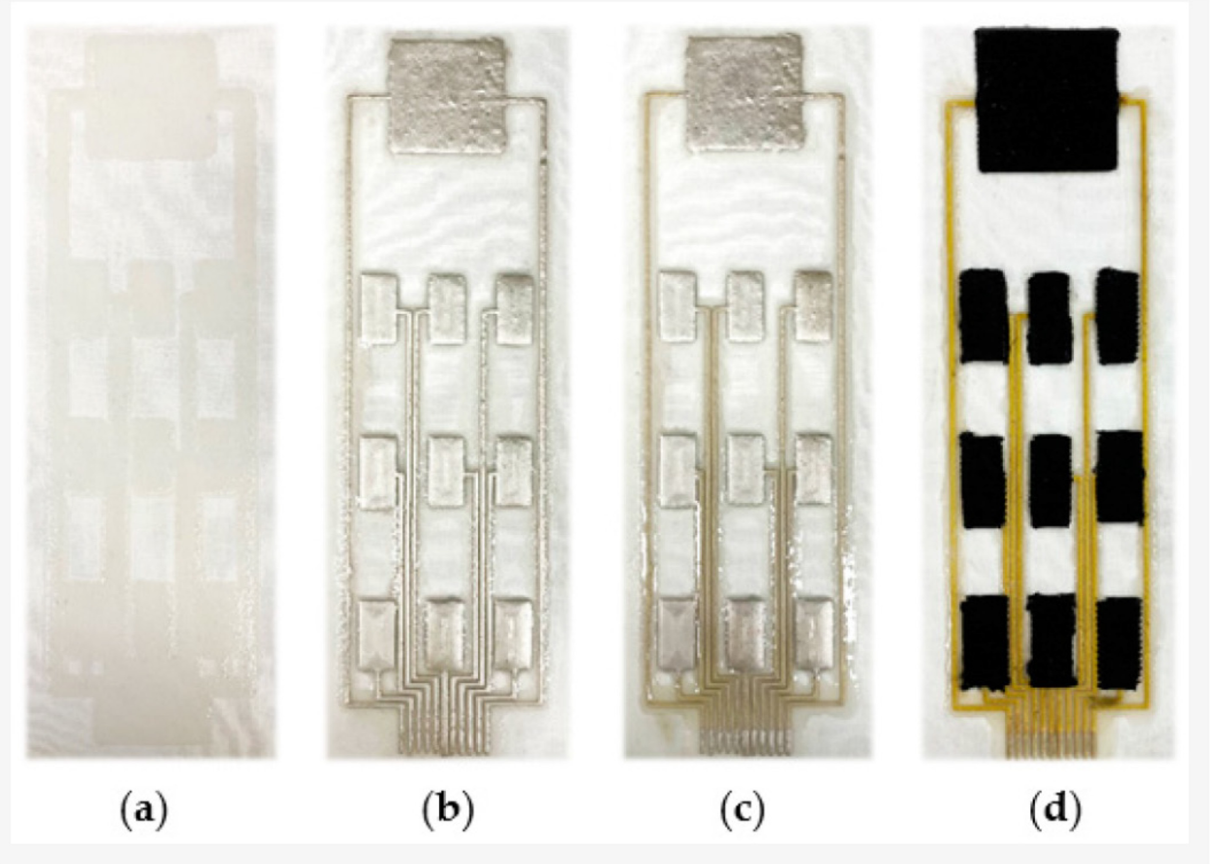

Figure 2.12: Dispenser-printed electrode structure for healthcare applications [68], a) interface layer, b) silver layer, c) encapsulation layer, d) carbon layer.

2.4 Material for the solution-processed semiconductor channel layer

The solution-processed deposited semiconductor can be divided into organic and inorganic types. The organic semiconductor material includes but not limit (poly(3,4-ethylenedixothiophene)- poly(styrene sulfonate) (PEDOT:PSS)[9] [10], 2,7-dihexyl-dithieno[2,3-d;2',3'-d']benzo[1,2-b; 4,5-b']dithiophene (DTBDT-C6) [11]). For solution-processed inorganic material channel layer, single-walled carbon nanotubes (SC-SWCNTs) [12], (In_2O_3[13],[14],[15], IZO[16], IGZO[17], [18], ZnO[19], [20], [21]). Although some materials may require glove box processing, it provides a low-cost, low-temperature method with inherently lower environmental impact than cleanroom-processed films [1]. The choice of functional materials used in the deposited film is critical to its behaviour and its suitability for solution processing.

The characteristics of printed semiconductor devices utilising state-of-the-art technology are as follows. Most printed semiconductor devices operate at the microscale, with the highest resolution typically not exceeding 1 µm. The thickness of the channel layer is inconsistently reported in the literature, ranging from 50 nm in inkjet printing to 20 µm in screen printing. This parameter is critical for printing, particularly in layer-by-layer structures like thin-film transistors. Additionally, the channel width is generally more significant than the channel length, exhibiting considerable variations across studies, which enhances the drain current. This design is analogous to traditional semiconductor devices but features significantly larger dimensions than cleanroom-fabricated counterparts. Inkjet printing is predominantly utilised for solution-processed semiconductor devices due to its operational simplicity and higher resolution. Moreover, the equipment required for inkjet printing is relatively more affordable compared to that used for photolithography. Some solution-processed transistors are partially printed, featuring electrodes defined by lithography or dielectric materials applied via spin coating. Table 2.2 summarises the dimensions and materials of 10 different solution-processed fabricated field-effect transistors (FETs).

Table 2.2: Channel width and length of solution-processed semiconductor layer from literature.

Fabrication process	**Channel Width**	**Channel Length**	**Channel Material**
Partially printed with photolithography defined electrode [69]	200 to 600 µm	10 to100 µm	Crystalline indium oxide
Ink-jet printed [13]	200 µm	90 µm	Crystalline indium oxide
Screen printed [21]	4 cm	330 µm	ZnO NPs
Photolithography [20]	500 µm	1.5 to 5 µm	ZnO NPs
Doctor-Blade printed [19]	2 mm	5 µm	ZnO NPs
Ink-jet printed [60]	600 µm	10 – 100 µm	ZnO NPs
Partially printed with photolithography defined electrode [70]	4 cm	90 µm	Indium oxide
Ink-jet printed [62]	500 µm	1 mm	PEDOT:PSS
Ink-jet printed [11]	500 µm	1.2 mm	DTBDT-C6
Screen printed [71]	500 µm	200 µm	PEDOT:PSS

2.4.1 Material for the electrode

The material for the printed electrode can be concluded as:

Most of the electrodes fabricated using spin-coating and printed inorganic metal oxide semiconductor are structured by photolithography [13], [14], [15], [20], [25], [69]. The material includes ITO[13], [70], Ag nanoparticle[72], carbon and Al [73]. For the top gate, PEDOT: PSS [14], Al+Ti alloy, Ag[21]. But PEDOT: PSS has higher resistance than the metal material [14]. PEDOT: PSS, Ag nanoparticle, ITO, and carbon nano power can be printed

2.4.2 Material for dielectric layer

For printed thin-film transistors, there are not too many choices in the printed dielectric. It is hard to solution process the dielectric layer. An alternative solution is to deposit an electrolyte layer as the dielectric layer. When fabricating printed transistors, all of the material used as a dielectric is electrolyte polymer. This kind of electrolyte is ion conductive and electron insulated [74]. When printing, the electrolyte should be liquid. After curing, it becomes solid. There are some transistors reported using liquid electrolytes without curing [62].

This kind of transistor's working function is not clear now. Wang divided this kind of transistor into two types: electrical double layer transistor (EDLT) and electrochemical transistor (ECT) [75]. As shown in **Figure 2.13** The different idea between them is the permittivity of the semiconductor channel material.

Huang reported a different idea from Wang. She reported the injection of the ion from the gate dielectric to the channel depends on the relationship between gate voltage and threshold voltage [74]. As **Figure 2.14** shows, when the gate voltage is higher than the threshold voltage, the working function is equal to EDLT mentioned before; when the gate voltage is lower than the threshold voltage, the working is equal to ECT mentioned before.

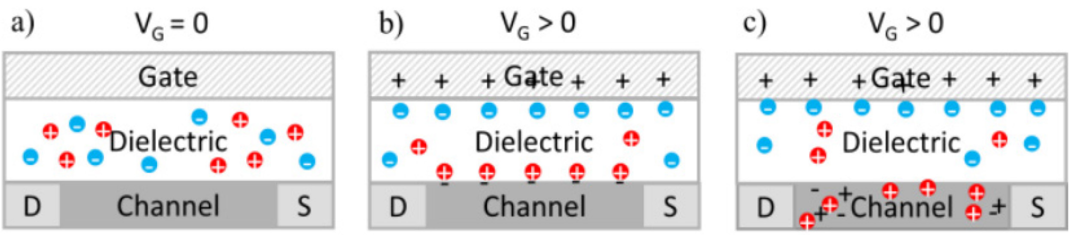

Figure 2.13: The working function of electrolyte gated field-effect transistor:
a) When no gate voltage is applied, the carriers(ion) in the electrolyte is not orientational, the transistor is off; b) when there is a biased voltage, an electrical double layer will be formed in the dielectric material and attract the carriers inside the channel; c) When the biased voltage, the ion will be injected into the semiconductor material and improve the conductivity of channel layer (ECT) [75].

Electrolyte dielectric deposition is reported by both screen printing and ink-jet printing. This is because it can be thicker than insulator dielectric. The most common electrolyte dielectric material is called CSPE (composite solid polymer electrolyte). This is commercially available.

However, there are also some solution-processed gate insulator layers published using Aluminium Oxide [76] [77]. The depositions are both done by spinning coating to achieve a highly homogeneous layer. Compared with organic electrolyte dielectric layer, the inorganic layer can achieve a thinner layer with similar dielectric properties.

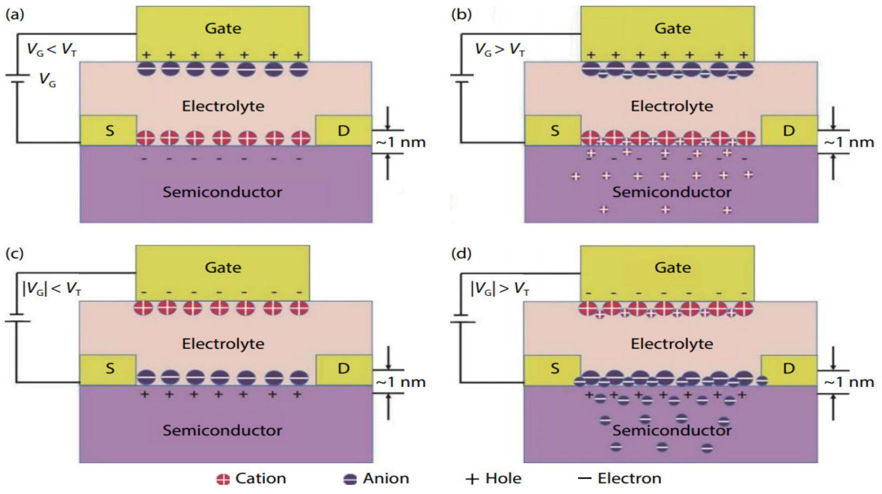

Figure 2.14: Different models about the electrolyte-gated transistor working function [74].

2.4.3 Material for solvents.

For the Printing process, it is important to use reliable dispersion for the nanoparticles. Two types of dispersions can be used as the ink for ZnO film: precursor ink and nanoparticle ink.

The precursor ink normally contains different types of substances. After printing, they will react with each other by heating on the substrate to form the target material. For ZnO, normally the precursor is zinc acetate [78]. The main advantage of the precursor process is more homogenised printed film after annealing. However, the reaction is difficult to control which leads to uncertain results on the substrate. The film possibly contains both product and unreacted reactants from the chemical reaction. This effect may also lead to discontinuing film, where the unreacted reactants are located between two product nanoparticles.

The nanoparticle ink is normally colloid: a kind of mfixture where one type of substance disperses into the medium rather than dissolve[78]. It is normally made by adding the nanoparticle powder into the solvents and only contains the nanoparticles which needed to be printed on the substrate. The process to fabricate the nanoparticle powder has been introduced in the previous section of this paper. The substance size of the colloid is larger than that in the solution. The advantage of nanoparticle ink is the direct printing process without any chemical reaction needed to form the film. The disadvantages mainly focus on the less homogenizer film than the fabricated film from precious. Because the nanoparticles in the dispersion easily aggregate to each other to form a larger particle. The aggregation process is random and unpredictable causing the non-uniform thickness of the film and finally leading to the bad properties of the devices. Therefore, the nanoparticle ink normally contains surfactants to avoid aggregation. For example, Lee used titanium diisopropoxide bis(acetylacetonate) (Ti(acac)2) as the surfactants for the ZnO ink, which has been proven to improve the ink stability [79].

In general, the roles of different materials in the ink includes solvent, surfactants and viscosity modifier [80]. The solvent normally works as the dispersion medium contributes to the solution environment. The basic properties of the solvent include not reacting with the nanoparticle, being easily evaporated and can dispersing the nanoparticles. The most common solvents are water, alcohol, and the mixture from polar and non-polar solvents. The surfactants normally are used to avoid the aggregation of the nanoparticles.

2.4.4 Material for encapsulation

Currently, there are limited studies on the encapsulation of ZnO nanoparticles. In 2018, Sun introduced a method for encapsulating ZnO micro-array UV sensors using polyvinyl alcohol (PVA) glue [81]. PVA is a non-toxic, cost-effective, and versatile polymer material. As illustrated in **Figure 2.15**, the PVA solution is evenly applied to the surface of ZnO microwires and allowed to dry. Once the PVA is completely dry, the PVA film, along with the ZnO, is peeled off. Subsequently, gold is deposited on the ZnO as an electrode. The ZnO photoresistor is fabricated by heating zinc to 950°C for oxidation. Upon completion of heating, the ZnO microstrips are placed on glass to undergo the described encapsulation process. Due to the weak adhesion of ZnO to the glass, the ZnO can be easily separated. However, a significant issue with this encapsulation method is that, while the substrate is bendable, the bent device's performance is not very stable [81]. Both the light resistance and dark resistance of the bent device are higher than in the flat state. This instability may stem from incomplete drying of water molecules within the PVA, which adhere to the ZnO surface and alter its properties. The interaction with water molecules increases the carrier concentration in ZnO. This principle will be further explored in the subsequent section. During bending, because of the piezoelectric field modifies the energy band and the surface charge of ZnO , the polarity of the water molecules is altered, influencing the interaction between ZnO and water and ultimately affecting the carrier concentration within the ZnO [81].

Although PVA is an excellent encapsulation material, it cannot be used alone as an encapsulation material in solution pH sensors due to its water-soluble properties. It may need to be used with a water-insoluble encapsulation material, such as polydimethylsiloxane (PDMS) [82]. PDMS is a widely used bioelectronic material with biocompatibility, chemical stability, and insolubility in water [83]. It is usually used in the field of medical devices. Due to its good hydrophobicity, PDMS has also been used in the field of semiconductor encapsulation [82]. However, since its oxygen barrier ability is not as good as that of PVA, it may not stabilize the electrical properties of ZnO NPs as an encapsulation material, which will be described in detail in the following sections.

Similar to PVA, EVOH as an oxygen-barrier polymer has also been used in the field of semiconductor encapsulation [84]. Unlike PVA, EVOH not only has excellent oxygen barrier properties but is also insoluble in water and can well isolate moisture. However, due to hydroxyl functional groups, EVOH still absorbs water molecules. As the relative humidity of the air increases, the oxygen barrier properties of EVOH will decrease [85]. Ji et al. [86] proposed a novel encapsulation method using EVOH for perovskite solar cells to reduce the moisture effect on the functional material.

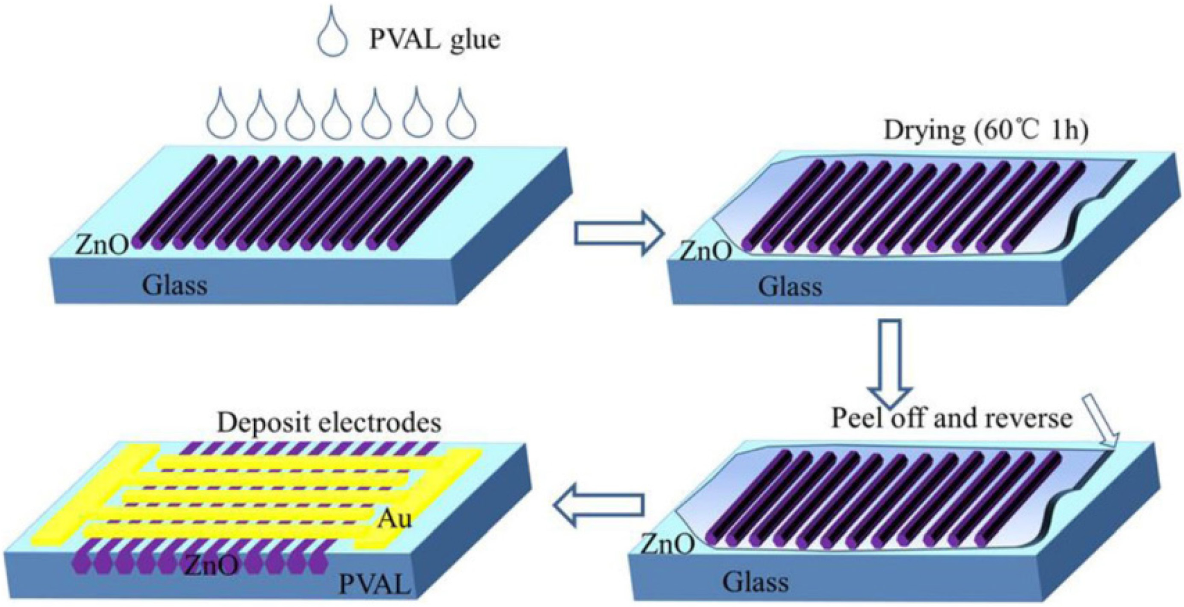

Figure 2.15: Encapsulation method for ZnO micro array UV sensor [81].

Some other packaging methods have also been proposed in other flexible electronics fields. In 2019, Sheng proposed a method of encapsulating flexible capacitors by hot-pressing ethylene-vinyl acetate (EVA) film with fluorinated ethylene propylene(FEP) [87]. EVA is a hot-melt packaging material, often used in flexible packaging. It has excellent corrosion resistance, flexibility and recyclability. However, its oxygen barrier property is much worse than that of PVA and EVOH. As shown in **Figure 2.16**, the FEP is covered on the surface of the EVA, and the pressure is applied to the heated EVA through the FEP, so that the EVA film is tightly attached to the textile. After the EVA is cooled, the FEP film is torn off from the surface of the EVA to complete the package. Due to the material properties, the cooled EVA will not stick to the surface of the FEP film.

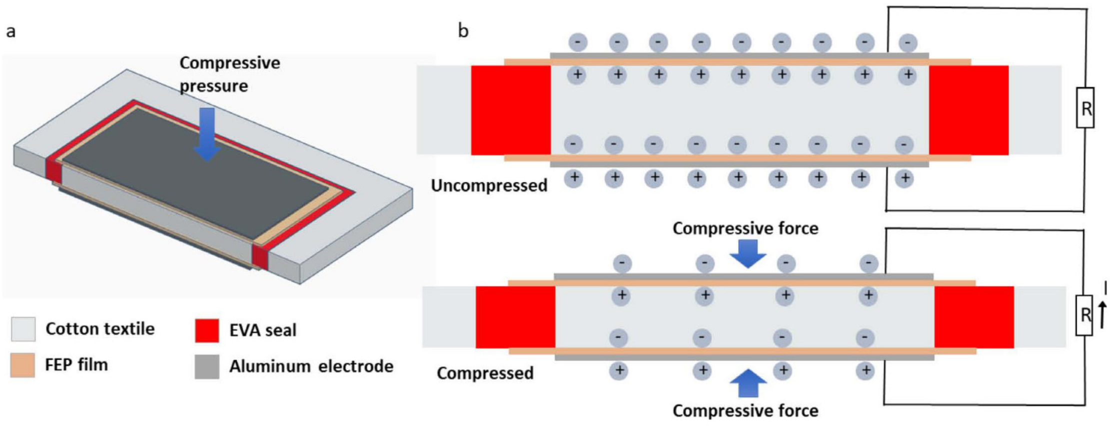

Figure 2.16: Encapsulation method using EVA and FEP film [87].

There is also a part of research published by mixing EVA puree with ZnO nanoparticles to make a thin film [88], [89], [90]. There is also a part of research published by mixing EVA puree with ZnO NPs to make a thin film. These films are used in the packaging of solar panels[88], materials for purifying greenhouse gases[89], and pressure-sensitive materials[90]. However, these EVA nano ZnO films have a common manufacturing defect. That is, the performance of ZnO cannot be improved by annealing. Since EVA melts at around 90°C, annealing the composite film is impossible. This also indicates that the possibility of making ZnO sensors by this method is not very high.

2.6 UV and oxygen molecules effect on ZnO NPs film

ZnO exhibits high sensitivity to UV light absorption at approximately 360 nm. The phenomenon of resistance change in ZnO when exposed to UV light is attributed to the absorption and subsequent release of oxygen molecules at its surface [91]. As shown in **Figure 17**, exposure of ZnO to UV light generates electron-hole pairs within the material. The generated holes recombine with electrons bound to oxygen molecules, facilitating the release of oxygen molecules from the surface of the nanoparticles. Consequently, the carrier concentration in ZnO increases. Conversely, when the UV light is turned off, oxygen molecules in the air, recombine with the surface of the ZnO, resulting in a decrease in carrier concentration [91] [92] [93]. The following equations can show the function [91]:

O_2 (g) + e^- → O_2^-(ad) (2.1)

hv → e^- + h^+ (2.2)

O_2^- (ad) + h^+ → O_2 (g) (2.3)

O_V is the lattice oxygen of the ZnO. V_0 is the oxygen vacancy. Since these reactions are reversible and in dynamic equilibrium, the reaction can proceed more rapidly by reducing the concentration of the corresponding substances in the environment. The attachment of water molecules to the surface of ZnO will increase the carrier concentration inside ZnO, which the following equation can explain[94].

H_2O + 2Zn + O_V → $2Zn^+$ - OH + V_o + $2e^-$ (2.4)

It has been documented in the literature [24] exposing ZnO to UV light in humid air can enhance the carrier concentration within the material. However, to achieve the desired performance gains, ZnO must be maintained in an environment with relative humidity exceeding 50 percent. Consequently, ZnO produced via this method may not reliably exhibit high performance in ambient air. Additionally, related studies have investigated the effects of exposing ZnO to UV light in various environments [95]. They placed ZnO in a pure nitrogen environment and exposed it to UV light, which can also increase the carrier concentration of ZnO. However, long-term working stability was not mentioned.

Based on the interaction between adsorbed oxygen molecules and ZnO NPs, Yihao et al. [96] proposed a surface acoustic wave (SAW) UV sensor based on ZnO. The sensor uses the change in resistivity of ZnO under UV and non-UV conditions to cause the sensor's resonant frequency to change. They also mentioned that moisture in the air will have a very large impact on the measurement results. So, they also proposed a packaging method to avoid the influence of moisture on the sensor. **Figure 2.18** shows the structure of the ZnO SAW UV sensor. The working principles are similar to the ones mentioned in equations 2.1 to 2.3. The oxygen molecules adsorbed on the ZnO surface trapped the electrons, forming the ionised oxygen molecules and increasing the resistivity of the ZnO layer. After the ZnO layer is exposed to UV light, the adsorbed ionised oxygen molecules are released from the surface of the ZnO, and the film's resistivity decreases, which changes the resonant frequency of the SAW device. The hydrophobic layer was deposited on the ZnO layer to avoid the influence of moisture on the resistivity of the ZnO functional film.

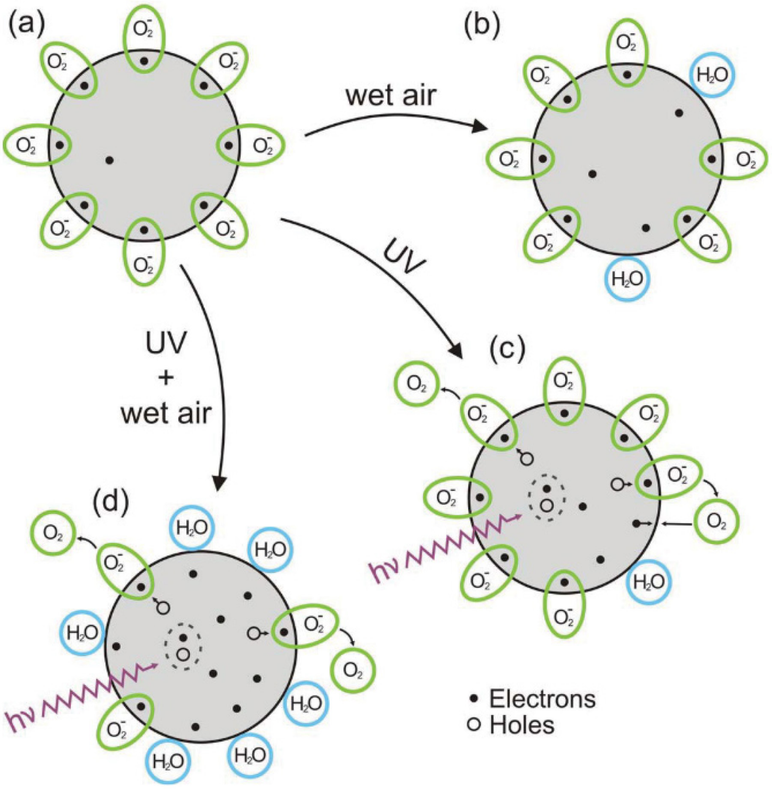

Figure 2.17: Schematic diagram of the influence of UV rays and water molecules on ZnO [24].

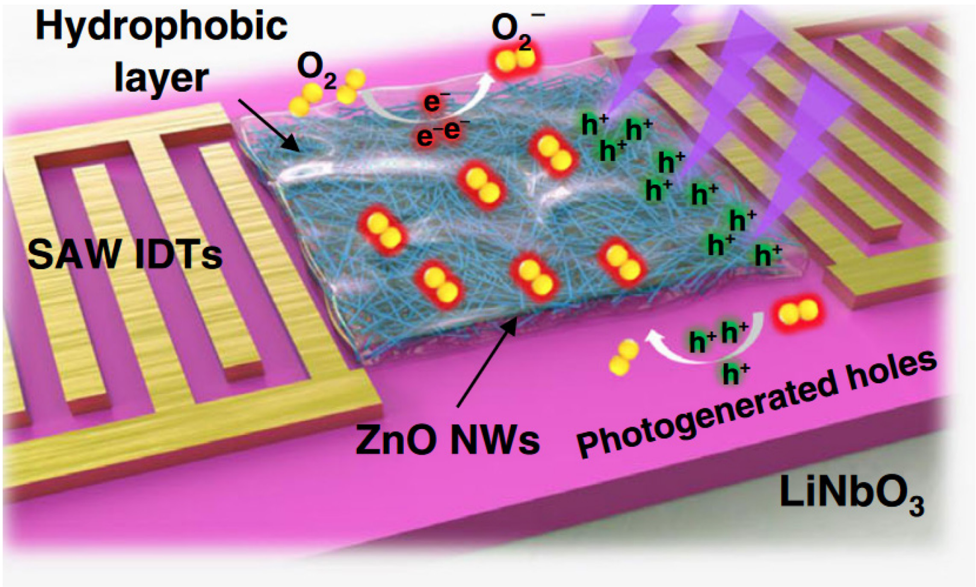

Figure 2.18: Structure of the ZnO surface acoustic wave UV sensor with the hydrophobic layer for moisture isolation [96].

Greenham et al. [92] proposed a ZnO UV sensor that operates based on changes in current related to this principle. They observed that, following exposure, the resistivity of the ZnO device does not return rapidly to its pre-exposure state. Subsequently, they developed a memory device utilising this adsorption principle [61]. This device is illustrated in **Figure 2.19**. The fabrication involves spin-coating a ZnO nanoparticle solution onto pre-deposited indium tin oxide (ITO), followed by heating and drying. An aluminium electrode is then deposited onto the surface of the ZnO nanoparticles using physical vapour deposition.

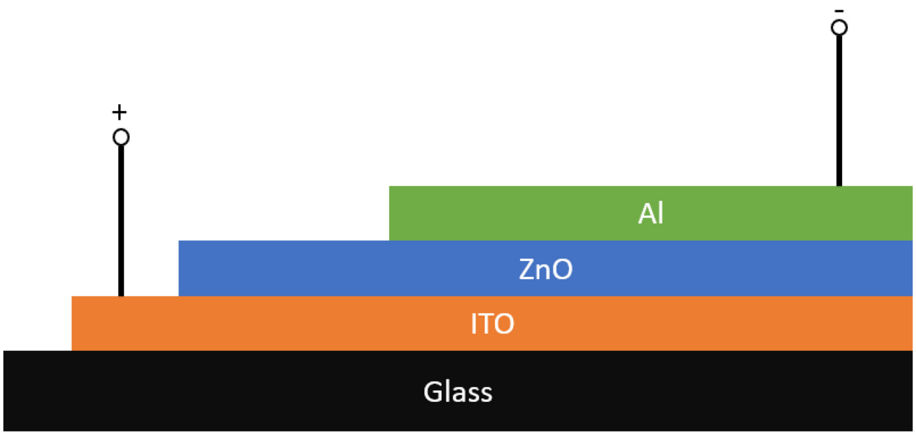

Figure 2.19: Structure of the ZnO memory device reproduced from [61].

The electrical characterisation of the memory device is presented in **Figure 2.20**. The voltage range from -3 V to 3 V represents the forward process, while the same range represents the reverse process. As indicated in the figure, the current during the forward process is more significant than that during the reverse process. This observation is explained by the fact that applying a positive voltage to the ITO electrode creates additional oxygen molecule adsorption sites at the Al/ZnO interface, leading to increased adsorption of oxygen molecules and an associated rise in resistivity, thereby transitioning the device into a high-resistance state. Conversely, applying a negative voltage decreases the number of adsorption sites for oxygen molecules, resulting in a reduced number of adsorbed oxygen molecules, which in turn lowers the resistance and transitions the device into a low-resistance state. Their research shows that not only UV can affect the adsorption process of oxygen molecules, but voltage can also have an impact.

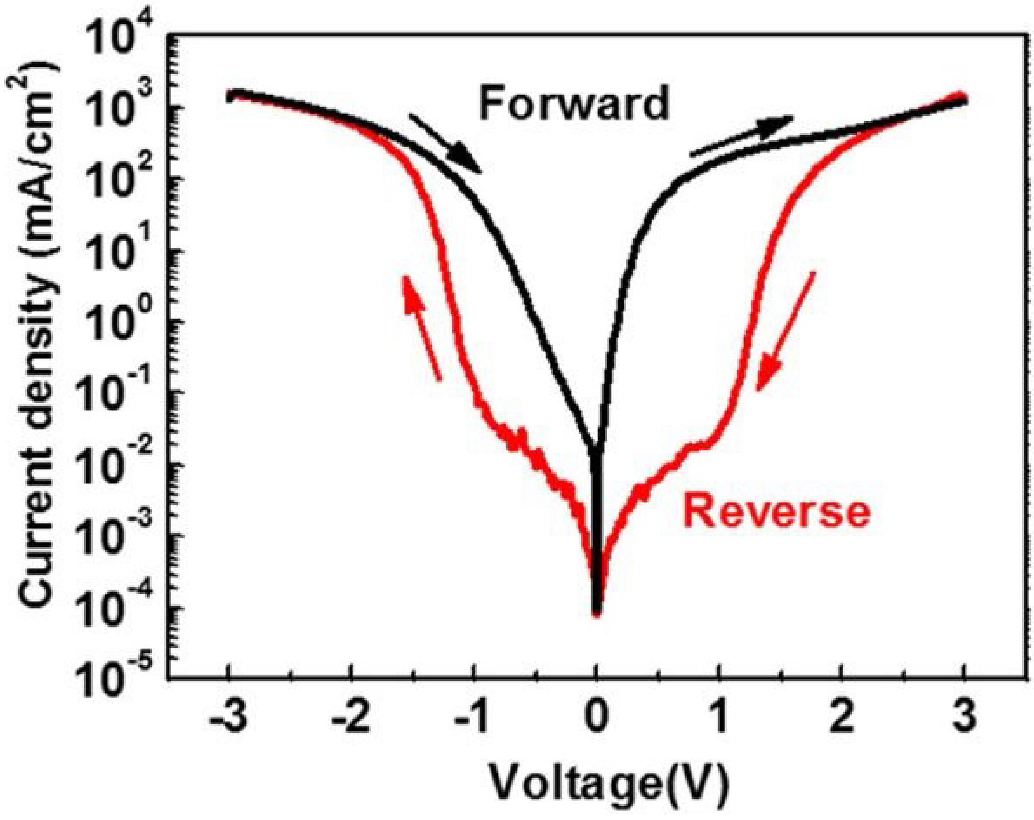

Figure 2.20: I-V characterisation of ZnO memory device [61].

2.7 pH sensor

pH, defined as the potential of hydrogen, is a critical indicator for assessing the acidity and alkalinity of a solution. It is determined by the concentration of hydrogen ions present in the solution. At room temperature, a pH value greater than 7 indicates an alkaline solution, while a pH value below 7 signifies an acidic solution. The measurement of pH is essential for evaluating the rate of chemical reactions, conducting biological environmental assessments, and performing medical monitoring.

2.7.1 Glass electrode pH sensor

The glass electrode sensor is the most commonly used commercial pH sensor [97]. As shown in **Figure 2.21**, it consists of a glass electrode and a reference electrode. When the glass electrode is immersed in a solution, the hydrogen ions in the solution are adsorbed to the surface of the glass membrane, forming a surface potential. The potential formed is related to the pH value of the solution. By comparing it with the potential of the reference electrode typically inside a standard pH solution, the pH value of the solution is measured. The ceramic junction ensures the ionic strength is the same in testing and reference electrodes. Glass electrodes are widely used because of their stable chemical properties, wide applications, and simple operation. Its disadvantages are that it is fragile, has a long response time, and is easily affected by temperature. Besides, the glass electrode has a theoretical maximum sensitivity, the Nernst limit. The voltage change per pH between the internal electrode and the reference electrode has a maximum value of approximately 59 mV. So, the sensitivity of this type of pH sensor can not be beyond 59 mv/pH.

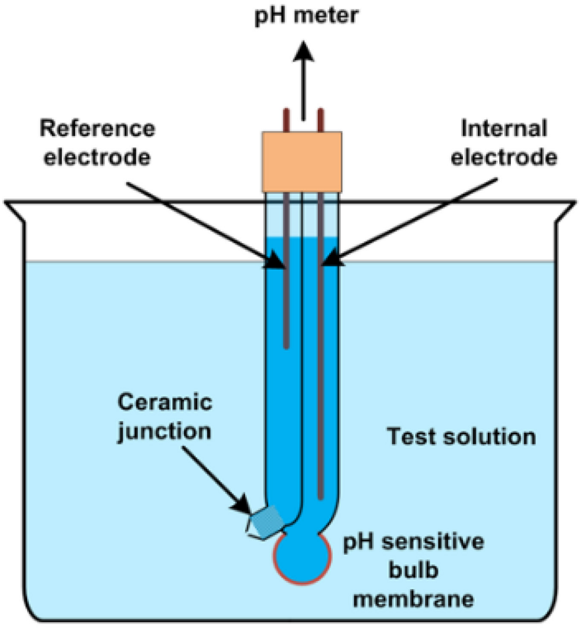

Figure 2.21: pH measurement using the glass electrode [98].

2.7.2 Polymer and carbon pH sensor

Some conductive polymers like poly(1,2-diaminobenzene) and carbon nanotubes can also be used as the pH sensor material [99]. The advantages of using polymers as the pH sensors are including but not limiting: high flexibility and suitable for wearable device, stretchable and bendable, can be deposited through solution processed deposition method and suitable for many types of substrate, and highly biocompatible. Their disadvantages includes: bad chemical stability and small pH sensing range, poor reproducibility and short life time [28].

2.7.3 Metal oxide pH sensor

Compared with glass electrodes, metal oxide pH sensors have the characteristics of fast response, high thermal stability, low cost, high integration and miniaturisation. In the field of pH sensors, their high surface area-to-volume ratio enhances ion adsorption from the solution, thereby improving sensitivity [28]. However, metal oxides are easily affected by environmental factors, such as light, which sometimes causes their electrical properties to be unstable, thus affecting the detection accuracy [28]. Recent advancements have focused on developing pH sensors that utilize metal oxides, such as ZnO [29], RuO_2 [30], WO_3 [31] and IrO_2 [32] as sensing layers.

As shown in equation 2.5, the operating principle of metal oxide pH sensors is based on the ability of hydroxyl groups on the metal oxide surface to function as adsorption sites for anions and cations, facilitating ion adsorption and generating surface potential. Different ions produce distinct potentials; specifically, the adsorption of hydrogen ions results in the formation of positive charges, whereas the adsorption of hydroxide ions leads to the development of negative charges [100]. These adsorbed charges are cheap, recyclable, and low-toxic metal oxide, and ZnO has critical potential applications in this field.

$$MOH_2^+ \overset{H^+}{\Leftrightarrow} MOH \overset{OH^-}{\Longleftrightarrow} MO^- \quad (2.5)$$

Compared with other metal oxides, ZnO is a common substance in the earth's crust and has low toxicity, is recyclable, and is easy to synthesize. As an ion-sensitive metal oxide, ZnO is also a promising material for pH measurement in solutions, which serves as a crucial indicator in medical diagnostics [29], [33], [34], [35]. Traditional ZnO pH sensors primarily determine the pH value of a solution by establishing contact between a ZnO electrode and the solution, and subsequently measuring the potential difference between the ZnO electrode and a reference electrode as shown in **Figure 2.22**. In this ZnO pH sensor microfluidic chip, the pH solution to be tested flows from the inlet to the outlet. When the solution reaches the ZnO layer, the hydrogen ions in the solution are adsorbed by zinc oxide, thereby generating a surface potential. The pH of the solution is determined by measuring the potential difference between the ZnO electrode and the reference electrode [34].

Figure 2.23 shows a flexible ZnO electrode pH sensor. The manufacturing process of this design sputters ZnO onto a flexible PCB board that has been pre-plated with gold electrodes. A layer of (3-aminopropyl) triethoxysilane (APTES) is drop-cast on the ZnO as a protective layer to prevent ZnO from being over-etched in the solution. Similar to the above principle, this sensor also measures the pH of the solution by comparing the potential difference between the ZnO and gold electrodes [29].

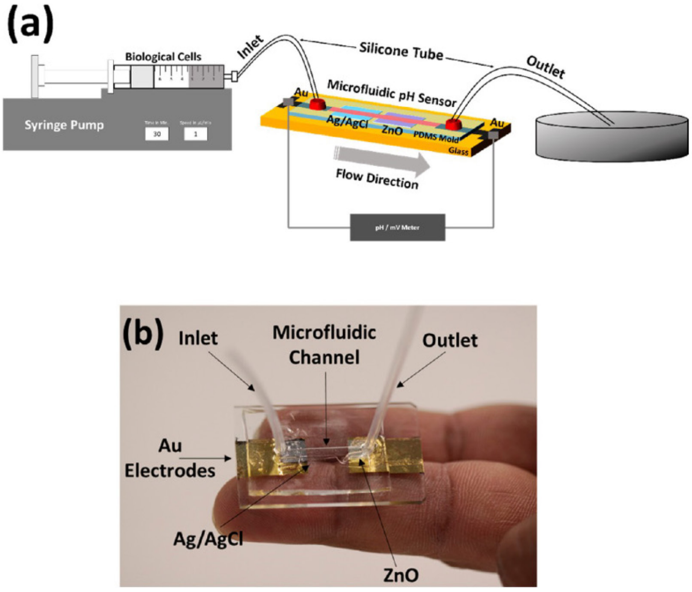

Figure 2.22: ZnO microfluidic pH sensor **a)** scheme and **b)** photograph [34].

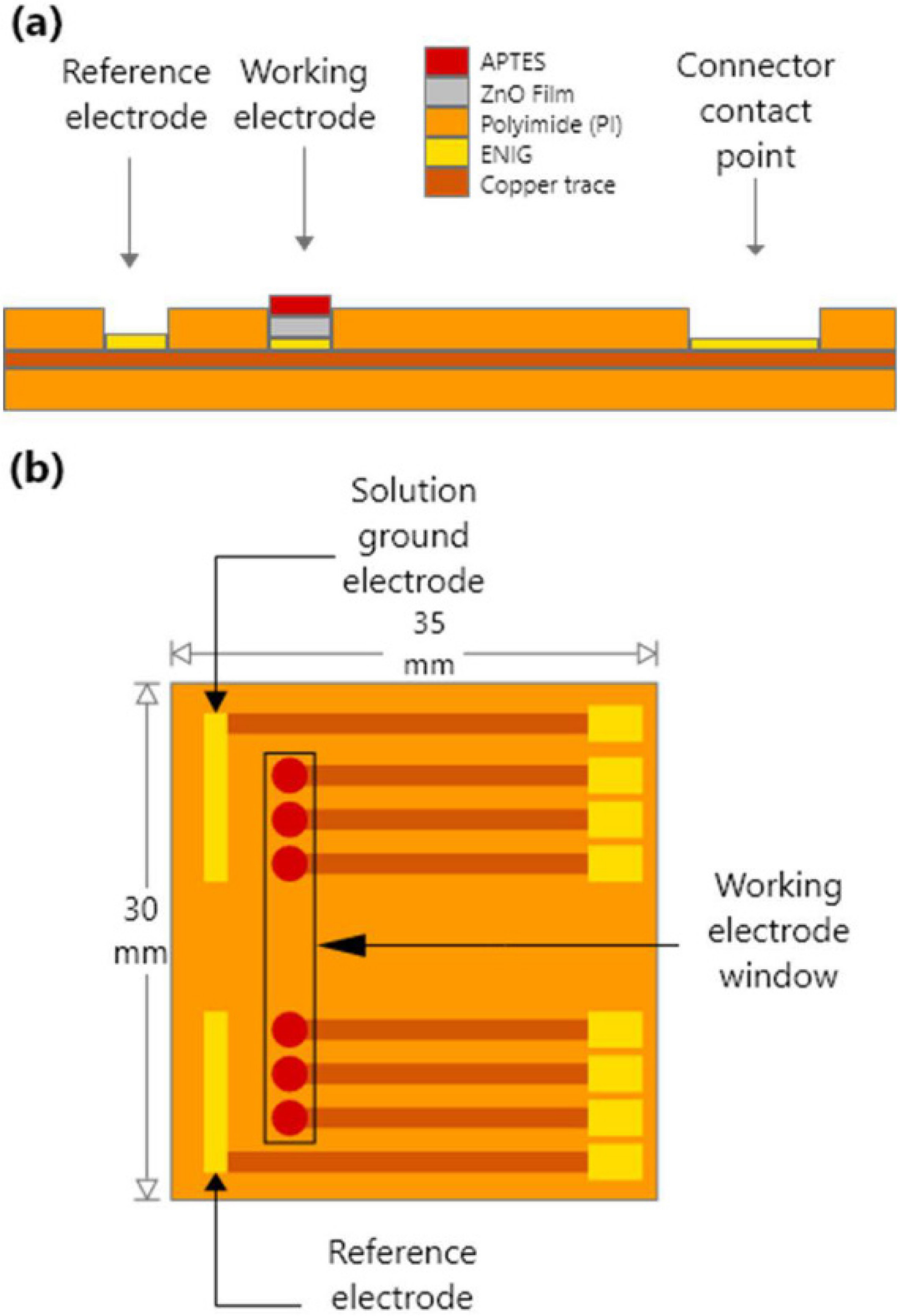

Figure 2.23: Flexible ZnO pH sensor **a)** cross-view and **b)** top-view [29].

However, the sensitivity of this type of sensor is constrained by the Nernst limit, which establishes a theoretical maximum of 59 mV/ pH unit. The table shows the comparison between the different metal oxide pH sensors.

Table 2.3: The sensitivity of different metal oxide pH sensors.

Senor types	**Sensor material**	**Sensitivity (mV/pH)**
Field effect transistor[101]	ZnO	38
Field effect transistor[102]	ZnO/silicon nanowire	46
Electrochemical[103]	Iridium oxide	51.7
Interdigitated electrode array[104]	ZnO	3.72
Extended gate sensing[105]	ZnO nanorod	53.55

Existing literature indicates that various channel materials and charge coupling devices have been studied and designed to achieve sensitivity surpassing the Nernst limit [36], [37]. As shown in **Figure 2.24,** A field effect transistor type pH sensor was simulated [36], which is different from the electrode type pH sensor mentioned above. The ele This sensor has a more complex structure. The dielectric layer under the gate electrode of this transistor contacts the pH electrolyte. Since the electrolyte changes the surface potential of the dielectric material, the threshold voltage of this transistor will also change. The IV curve of this sensor is shown in **Figure 2.25**. As electrolyte solutions of different pH values come into contact with the gate dielectric layer, the current in the channel is affected accordingly, and its threshold voltage changes accordingly. They claim that the sensitivity of their sensor is 180 mV/pH, which exceeds the Nernst limit. Shogo et al. also [37] proposed a wearable pH sensor using metal oxide beyond the Nernst limit. The device is shown in **Figure 2.26** and the sensitivity of the devices is claimed as 240 mV/pH. They used a Schottky-barrier-based charge-coupled device structure. However, the complexity of this device design poses significant challenges in the fabrication.

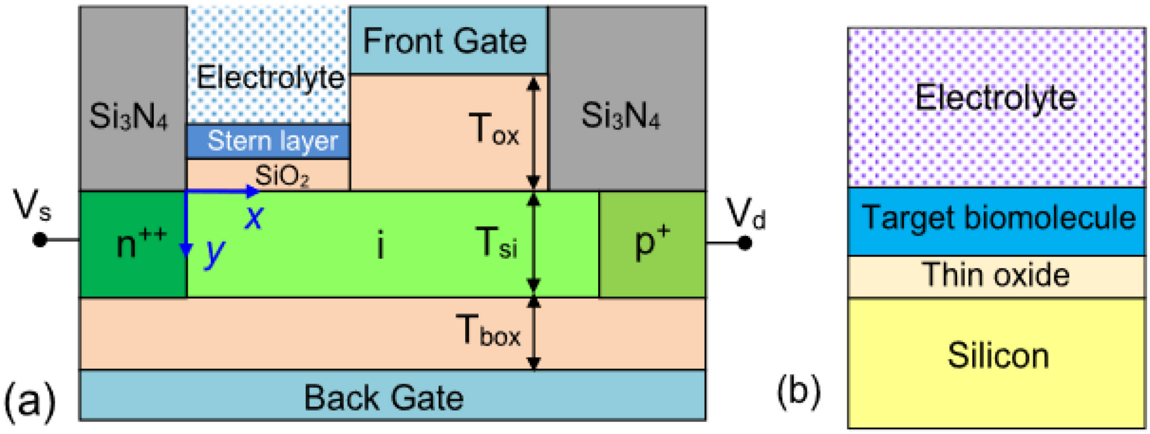

Figure 2.24: a) Design of the FET sensor across the Nernst limit **b)** View of the detection layer [36].

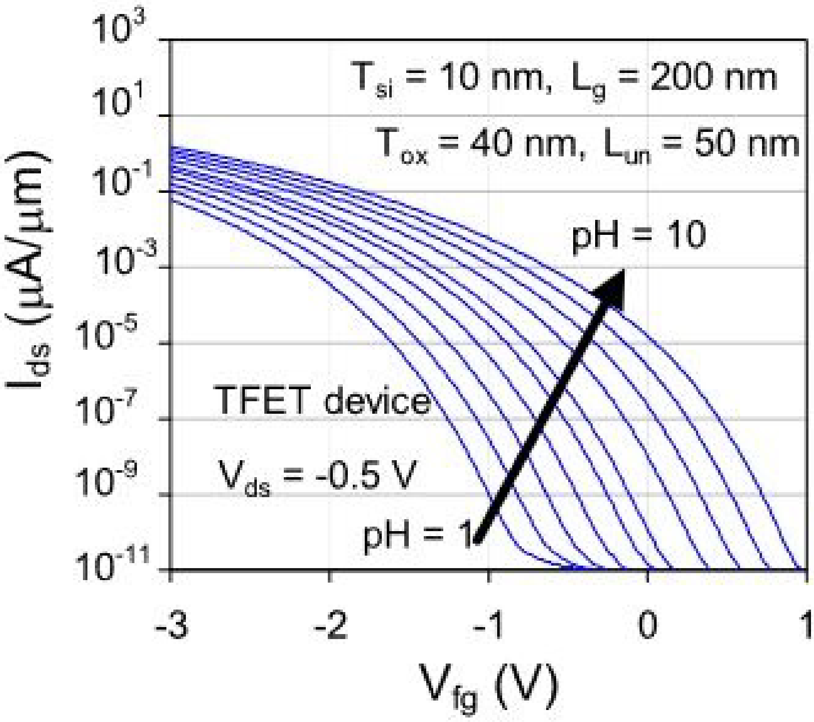

Figure 2.25: The IV curve of the field effect transistor pH sensor [36].

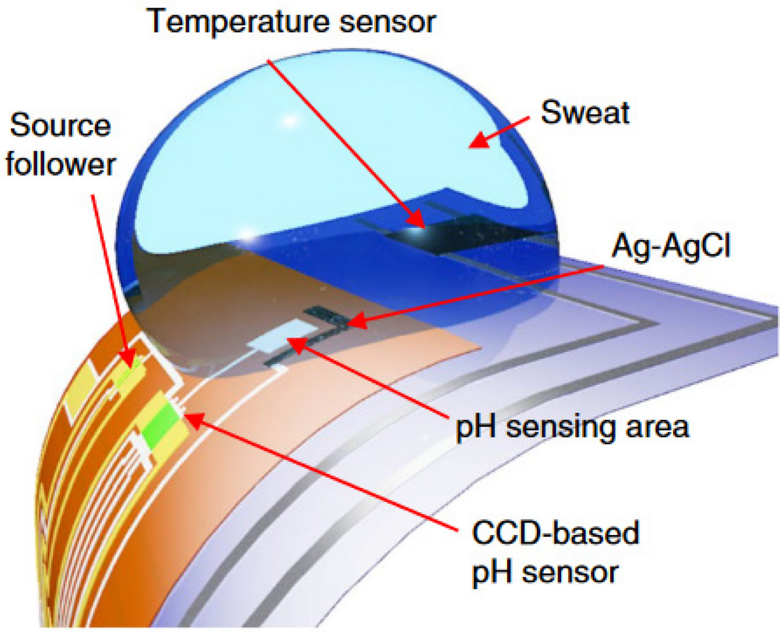

Figure 2.26: Charge coupling device across the Nernst limit [37].

2.7.4 Super Nernstian Sensitivity

Yujian et al. demonstrated a possible model of super-Nernstian sensitivity, which innovatively explains the mechanism of action of pH sensors [106]. In their equation, the Nernst sensitivity was written as $\frac{1}{r} \times 59.12$ mV/pH. They added an adjustment coefficient 1/r to the traditional Nernst formula. This coefficient is the ratio of the number of hydrogen ions involved in the interaction to the number of transferred electrons during the sensor's detection process. When the amount of hydrogen ions is greater than the transferred electrons due to chemical reactions, such as acid doping, the coefficient is greater than 1, and the device sensitivity is greater than 59 mV/pH.

2.8 Measurement method

2.8.1 Transmission length measurement (TLM)

TLM is to measure the contact resistance and sheet resistance of materials by measuring samples of the same width but different spacing. As shown in the equation below, when measuring semiconductor resistance, the measured quantity can be divided into three parts as shown in the following equation:

$$R_{total} = 2R_{metal} + 2R_{contact} + R_{semi} \qquad (2.5)$$

Where R_{metal} is the metal resistance, which can be ignored with very small amount. $R_{contact}$ is the contact resistance and R_{semi} is the semiconductor resistance.

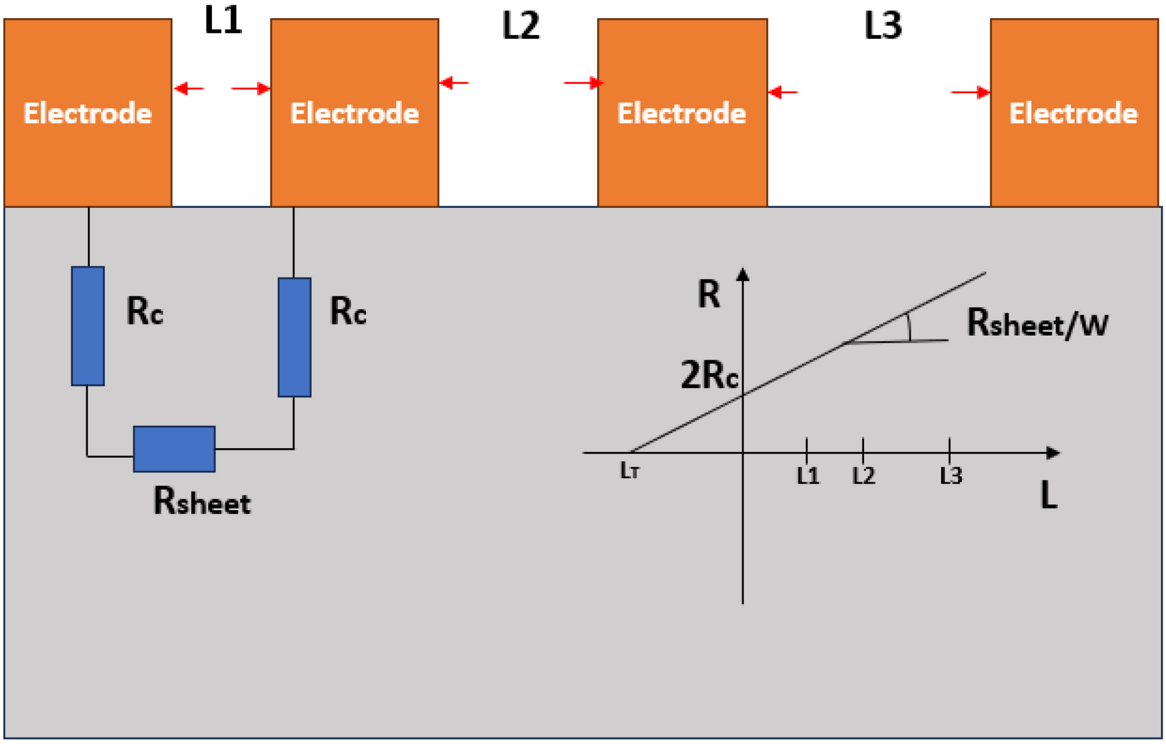

Figure 2.27: TLM structure for measurement.

As shown in **Figure 2.27**, the method is by depositing the same conductor material on the semiconductor surface. A data table as shown in **Figure 2.27** is obtained by measuring the resistance of different spacings. The slope in the function expression of the resulting straight line is the quotient of sheet resistance and width. The intercept is twice the contact resistance. The equation can be written as follows:

$$R_{total} = \frac{R_{sheet}}{W}(2L_T + L) \qquad (2.6)$$

W is the equal width of the metal. According to formula 11, it can be judged that the intercept of the linear function obtained after sorting and summarising the measured data is twice the contact resistance, and the slope is the quotient of the semiconductor sheet resistance and the metal width. The intersection of the straight line and the horizontal axis is twice the transfer length.

2.8.2 Hall measurement

Hall measurement is used for the carrier mobility in the semiconductor film. The measurement system is based on the hall effect. When electrons in a solid are driven by voltage and pass through a directional magnetic field, they are deflected by the Lorentz force and move to both ends of the solid, where they continue to accumulate. The accumulated electrons form an electric field and exert a force on the electrons moving in the conductor. When the applied electric field force is sufficient to offset the Lorentz force generated by the magnetic field, the electric field at both ends of the solid no longer increases. At this time, the voltage generated by the electric field is the Hall voltage.

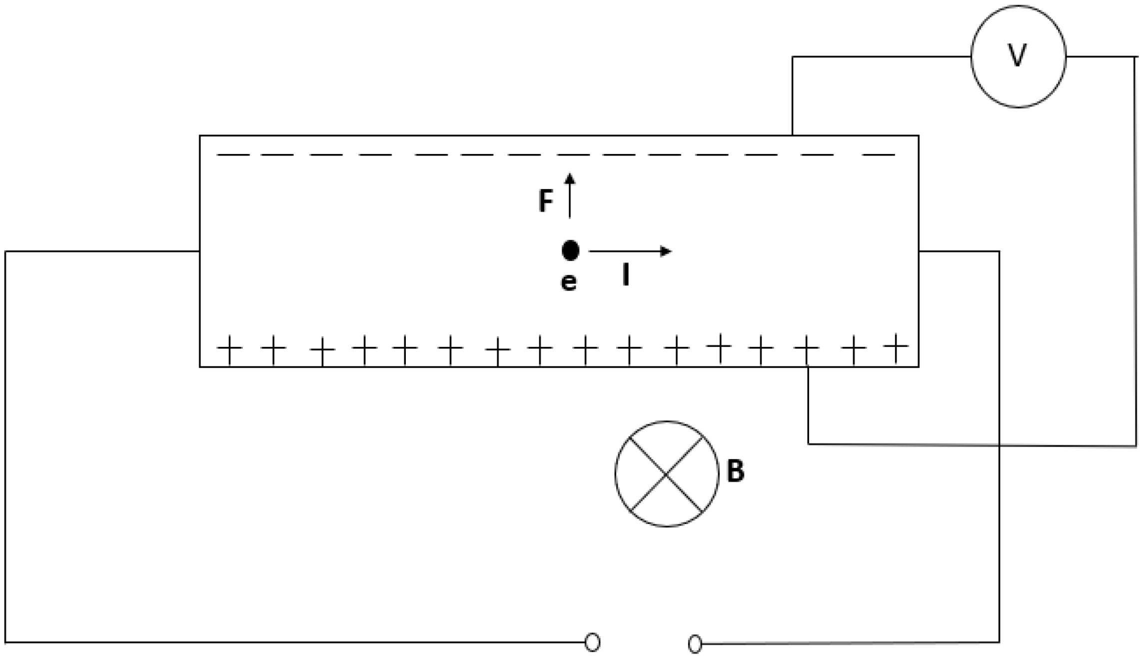

Figure 2.28: The working function of hall effect measurement.

As shown in the **Figure 2.28**, B is the applied magnetic field, and V is the voltmeter for measuring the Hall voltage. e is the carrier (electron), and I is the current which is opposite direction of electron movement. F is the direction of the Lorentz force on the electron. When a current passes through an applied vertical magnetic field, a force perpendicular to the current line is applied to the carriers. At this time, the carriers will move to the direction perpendicular to the current and accumulate continuously. This newly formed electric field will also exert an electric field force on the carriers, which is in the opposite direction to the Lorentz force experienced by the carriers moving in the horizontal direction. When accumulated to a certain extent, the newly formed electric field force will cancel out the Lorentz force generated by the movement of carriers along the horizontal direction. This allows carriers to pass through the sample normally. At this time, the newly generated electric field potential is measured as the Hall voltage.

$$n_s = \frac{IB}{q|V_H|} \qquad (2.7)$$

$$\mu = \frac{1}{q n_s R_s} \qquad (2.8)$$

n_s is the sheet carrier concentration. R_s is the sheet resistance and μ is the carrier mobility. q is the charge of the electron. The sheet carrier concentration and carrier mobility of the measured sample can be deduced and calculated by the above formula.

2.8.3 XPS measurement

X-ray Photoelectron Spectroscopy (XPS) is a technique employed to analyze the composition and chemical states of functional groups at the surface of materials. This characterization method is based on the phenomena of photoemission. When X-rays are directed onto the sample surface, they excite electrons (photoelectrons) within the material. These excited electrons are subsequently released into a vacuum, and their kinetic energy is directly related to the binding energy between the electrons and the atoms in the sample. By measuring this kinetic energy, information regarding the binding energies can be obtained, allowing for the inference of the original chemical states present on the surface of the solid sample [108].

2.9 Conclusions of Chapter 2

This chapter provides a comprehensive summary and review of the pertinent knowledge documented in the literature. The solution processed ZnO NPs shows high resistivity and low electrical stability. The topics covered include, but are not limited to, methods of solution-deposited semiconductors, printing techniques, solution compositions, relevant application devices, and the response of ZnO to UV light. The conventional pH sensor shows the Nernst limit sensitivity. Some pH sensors beyond this limit but the fabrication process is relatively complex. ZnO is a promising material for this type of sensing, however, its electrical properties are affected and limited by the adsorbed oxygen molecules. The strategies discussed herein for enhancing the performance of ZnO through UV exposure present numerous insights for this study. UV exposure is known to temporarily reduce the resistance of ZnO by disrupting the electrostatic attraction between ZnO nanoparticles and atmospheric oxygen. Water molecules play a pivotal role by liberating the charge carriers bound by oxygen within the ZnO. These principles exhibit similarities, suggesting that ZnO performance can be enhanced by exposure to an environment containing solely water molecules. Additionally, to maintain ZnO in a high-energy state, it must be encapsulated in a low-oxygen environment during manufacturing to prevent oxygen from reattaching to the ZnO surface. However, these experiments were all conducted in air. It is reasonable to speculate that the efficiency of this physical phenomenon can be improved in a vacuum environment, so that the target molecules can more fully contact the surface of ZnO NPs. This led to the subsequent UV-Vacuum-Heating (UVVH) manufacturing technology. The following chapter 3 will outline the fabrication methods derived from these methods.

Chapter 3

Solution-Processed Fabrication Method and UVVH Treatment with Different Passivation

Introduction

Solution-processed functional films have been demonstrated in many applications, including human-computer interface [2]. point-of-care equipment [3], [4], wearable devices [5], and light-emitting devices [6]. These spin-coated or printed films have been utilized in numerous sensing applications, such as gas [109], biomarkers [62], and moisture [110]. Solution processed-deposition method at room temperature in ambient conditions offer a low-cost, low-temperature fabrication method with reduced environmental impact compared to chemical or physical vapor deposition process [1]. These functional films are categorized into organic and inorganic materials; however, in this thesis, we focus on the fabrication of solution-processed inorganic semiconductor layer.

Inorganic semiconductor materials, such as metal oxides, including Indium Oxide (In_2O_3) [13], [15], Indium Zinc Oxide (IZO) [16], Indium gallium zinc oxide (IGZO) [17], [18], and Zinc Oxide (ZnO) [20], [21], [111], [112], [113], [114], are compatible with solution-based deposition manufacturing processes. For example, metal oxide precursors or particles would be added to a dispersion agent formulated to the correct rheology for printing [13], [69], [115] or spin coating [92], [116] onto a substrate, followed by a suitable drying/curing step to form semiconductor layer. Semiconducting ZnO NP sensors that change resistance have gained widespread attention due to their low cost, high electron mobility and robust chemical and thermal stability [117]. The predominant sensing mechanism by which the ZnO functional layers respond to a measurand is chemical surface adsorption [117]. For n-type ZnO NP, the adsorption of chemical analytes on the nanoparticle's surface influences carrier binding or release, thereby modulating its resistance [118]. Oxygen molecules, for example, bind free electrons within ZnO NPs forming highly active oxygen species increasing the film resistivity [118], [119], [120], [121]. The sensing mechanism within ZnO NPs for reducing substances is closely tied to surface oxygen, whereby reducing substances undergo oxidation by oxygen species, releasing trapped electrons and consequently reducing the resistivity of ZnO NPs [118], [119]. Even with low target molecule concentration of 1 ppm, chemiresistive sensors can exhibit a resistance change of over 50% [118]. Studies have indicated that chemical analytes are not required to be in direct contact with the ZnO surface; rather, deposition of a dielectric layer such as aluminum oxide, silicon oxide, or APTES on the ZnO surface allows analyte adsorption to alter ZnO resistance through a field effect [22], [29], [96], [122].

However, ZnO NP presents two primary drawbacks: high resistivity and susceptibility to environmental influences, resulting in unpredictable electrical behavior of devices. Therefore, improving the ZnO device's electrical stability is critical in this research area [123]. While solution-processed metal oxide semiconductor materials are resilient to decomposition in ambient environments, their electronic properties remain susceptible to environmental influences [124]. Molecules from the ambient environment with weak hydrogen bonds can become dissociated leading to electron binding within the ZnO, influencing its resistivity [91]. Additionally, resistance measurements are likely conducted immediately after film deposition due to the propensity of ZnO film resistance to increase upon exposure to ambient conditions. Limited studies have explored the long-term stability of the electrical properties of ZnO NP films. According to the literature [24], [91], [93], [117], the elevated resistivity of ZnO NP correlates with oxygen molecules adsorbed on its surface, which diminishes the carrier concentration of ZnO NPs. While high-resistivity ZnO films exhibit improved semiconductor response rates, their electrical characteristics are more influenced by environmental factors such as light and moisture. To mitigate high resistivity and enhance electrical stability, UV light can temporarily revert adsorbed oxygen to the gas phase, facilitating its removal from the surface of ZnO NP films under negative pressure condition. After being stored in a dark environment, the resistivity of the samples would increase considerably [125]. Preventing oxygen re-adsorption requires the use of passivation layers composed of hydroxyl groups, such as water molecules. Therefore, a passivation layer with low oxygen permeability and high thermal stability is essential to sustain low resistivity over time.

Several polymer passivation layers have demonstrated capability in meeting the aforementioned requirements [126], with Ethylene Vinyl Alcohol (EVOH) being particularly prominent. Ethylene Vinyl Alcohol (EVOH), derived from Ethylene Vinyl Acetate (EVA) [127], serves as a widely utilized flexible oxygen barrier in various applications [127], [128], [129], including its role as an airtight encapsulant for sensitive electronic materials. This polymer film finds extensive use as a passivation layer in electrical applications, including solar cells [86], [130], supercapacitors [87] and thin film transistors [131]. EVOH is an environmentally friendly, durable, and a low toxicity polymer that can be used as a cost-effective gas barrier material [127], [128], [129]. The presence of hydroxyl functional groups within its molecular structure enables facile adsorption onto the surface of ZnO NPs. Additionally, the oxygen permeability of EVOH barrier films can be modulated by adjusting the heating temperatures. Elevating the film temperature to within the range of 180–200°C, where 200°C represents the melting point, enhances the oxygen permeability of EVOH, allowing oxygen to escape from the ZnO film surface [132]. After cooling, the film regains its exceptional oxygen barrier properties.

Therefore, in this chapter, we introduce a novel solution-based UV-Vacuum-Heating (UVVH) fabrication process to passivate ZnO NP films that reduces film resistivity and enhances electrical stability. The method involves spin-coating ZnO NP onto a patterned silver electrode, followed by heating the solution-processed ZnO NP film in a vacuum environment while continuously exposing it to UV light to eliminate the oxygen molecules. UV light aids in disrupting the bond between oxygen molecules and ZnO NP, while negative pressure aspiration and heating extract the oxygen molecules from the ZnO NP film. To assess the electrical stability of the ZnO NP films and prevent reabsorption of oxygen molecules, surface passivation is essential [133]. The passivation effect of water and polymers EVA, EVOH and polyvinyl alcohol (PVA) polydimethylsiloxane (PDMS) composite layer have been investigated. The theory and physics behind the fabrication method will be introduced in the next chapter.

3.1 Electrode printing

For the electrode printing, The commercial silver ink TC-C4007 was speed mixed at 3000 rpm for 1 minute before the printing. The Fisnar F7300NV dispenser printer was used for the device fabrication. The printed is shown in **Figure 3.1**.

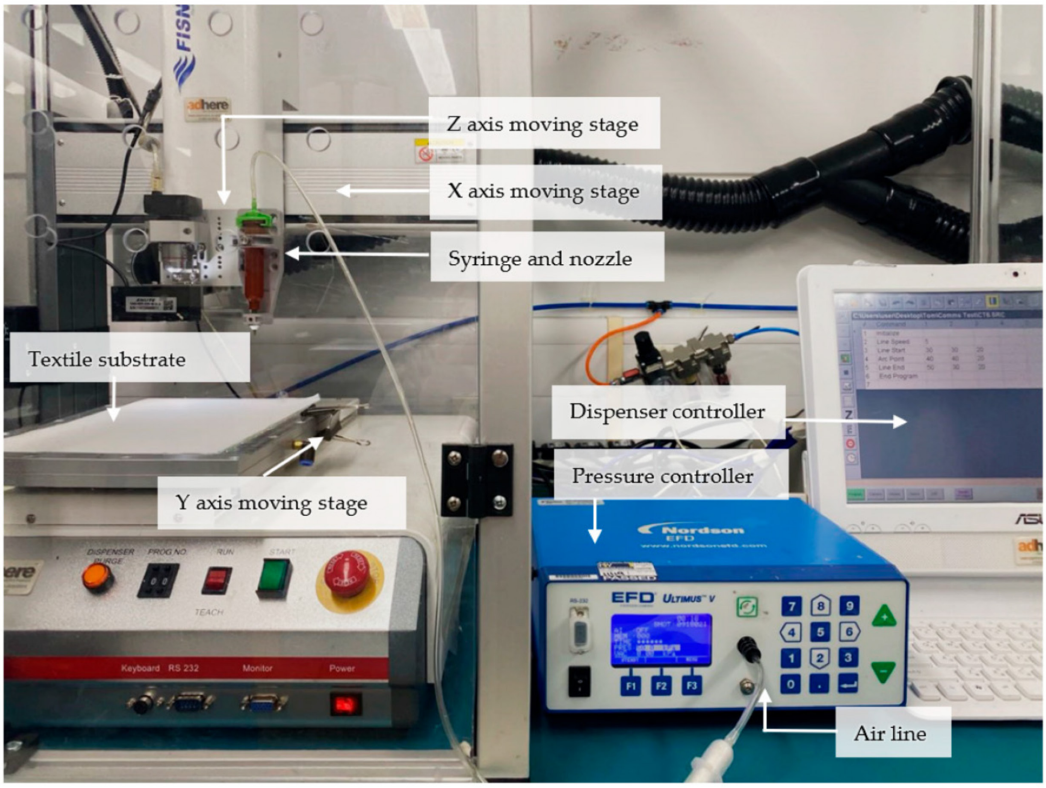

Figure 3.1: Schematic diagram of Fisnar F7300NV dispenser printer. The figure is reproduced from the research group members' publication [68].

The specific use parameters of the dispensing printer in this study are: air pressure of 200 to 400 kpa, needle tube moving speed of 0.8mm/s and needle tube radius of 0.1mm. The specific use process is, first of all, in order to ensure the sustainability of printing, the needle must be as close as possible to the substrate. According to the measurement, the distance between the needle and the substrate is between 0.08 mm and 0.1 mm. After adjusting the distance, pour the silver ink into the syringe. In order to examine the effect of different air pressures on silver electrodes, air pressures of 200 kPa, 300 kPa and 400 kPa were used to print the electrodes, respectively. Finally, for consistency, the needle should not move too fast. Otherwise, it will leave different ink dots at the beginning and end of printing. The smallest width of each pressure was shown as follows:

Table 3.1 The smallest width of the silver contact with different air pressure. The resolution was measured using microscope.

Air pressure using in the printing (kPa)	**Highest resolution of silver line (mm)**
200	0.13
300	0.16
400	0.19

After printing the silver electrodes, a methanolic zinc oxide solution was spin-coated on the glass substrate. The ZnO thin films were formed by spin coating at 2000 rpm for 20 seconds upon the sliver contact.

There were three silver electrodes patterns printed on the glass. The printing pressure is 200 kpa and the speed is 3 mm/s. First, to test the time-dependent stability, an interdigitated electrode structure was used, with an effective channel width (W) and length (L) as shown in the schematic diagram **Figure 3.2 a and 3.2b** with a W/L ratio of 90 ± 5 mm : 0.85 ± 0.06 mm = 105. For TLM, six 10 mm long, 0.25 mm wide lines were printed on the glass with the distance between the adjacent lines being 2 mm, 4 mm, 6 mm, 8 mm and 10mm. Figure 3.3 shows the TLM lines with 4 mm and 6 mm wide spacing. These films were used for measuring the contact resistance, sheet resistance and the transfer length. For Hall measurements on separate samples, four additional silver contacts were printed on the corners of the 15 mm × 15 mm square glass substrates. The carbon electrodes used for the pH sensor were printed as the 2.5 mm x 15 mm on each side of the glass substrate.

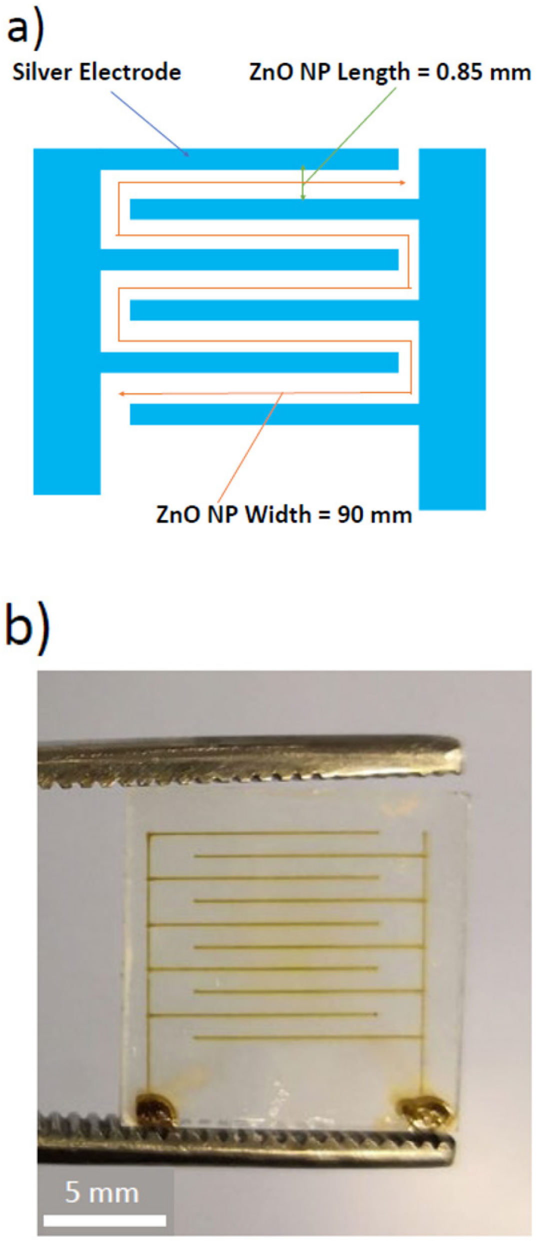

Figure 3.2: a) Geometry design parameter of the interdigitate electrode device and the length and width of ZnO NP film. **b)** ZnO NP film with interdigitated silver electrode after UV-vacuum-heat EVOH passivation. The effective electrode channel width is 90 mm and the length is 0.85 mm. The IDT is used to increased the measured material width and decrease the material length, this reduces the resistance of the sample and simplifies the measurement.

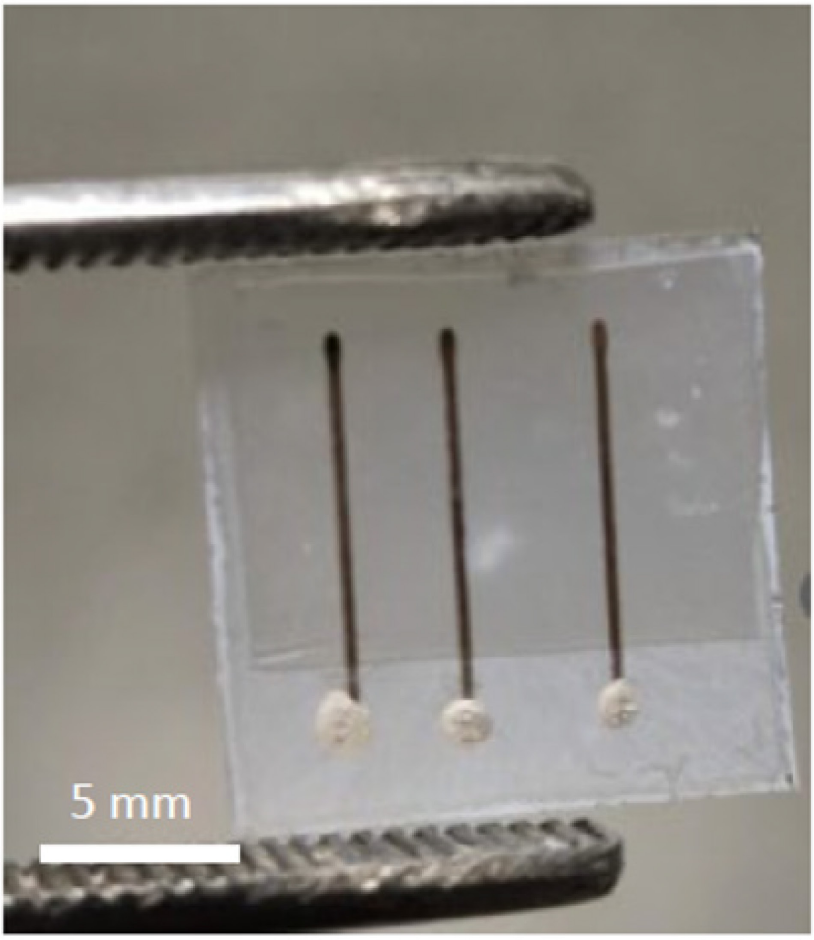

Figure 3.3: TLM structure with the gaps between lines of 4 mm and 6 mm and passivated by EVA.

3.2 UV Vacuum Process with Water

From Vidor's work [24], UV light can remove the adsorbed oxygen molecules on the surface of ZnO NPs, and water molecules can work as a passivation. His work was done in the atmosphere. It can be predicted that, under the vacuum environment, the adsorbed oxygen molecules can be more efficiently removed and the water vapour can contact the NPs surface without the influence of other gas.

For the investigation of water molecular interactions, the experimental setup and procedure are detailed in **Figures 3.4 and 3.5**. A customised vacuum chamber with two holes in the side wall was used to optimise the ZnO film. The UV lamp and the hot plate were connected to the power supply outside the chamber, and the humidity sensor was connected to the Arduino UNO. The connection holes were sealed using silicone gel.

Ten millilitres of deionised water were placed in a beaker adjacent to the ZnO, and both were subjected to heating under vacuum conditions. Once the relative humidity reached 70%, a 365 nm UV lamp was activated for one hour of exposure. The specific procedure is as follows: the vacuum box was evacuated to -0.98 bar, and the vacuum pump was subsequently heated to 50 °C using a hot plate. This heating process was maintained for approximately 20 minutes until the relative humidity within the cabinet achieved 70%. At this point, the UV lamp was switched on, and the exposure continued for an additional one and a half hours.

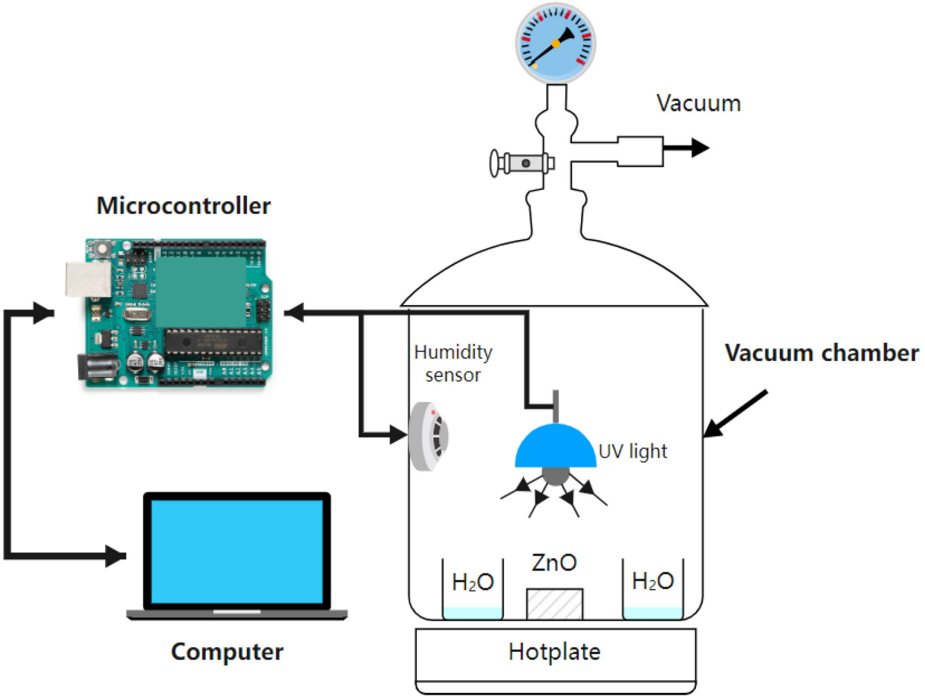

Figure 3.4: Schematic diagram of the vacuum ultraviolet light exposure system for water passivation. The UV lamp and humidity sensor inside the vacuum chamber are controlled by a microcontroller. An external power supply controls the hot plate. The UV light wavelength is 365 nm.

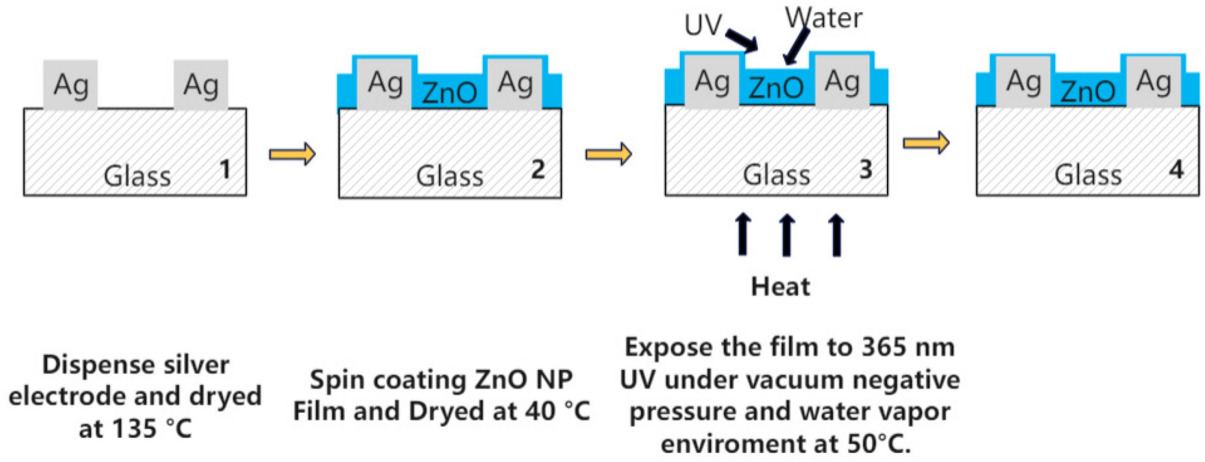

Figure 3.5: Schematic diagram of the fabrication process for the UV-vacuum-water process.

3.3 UVVH PVA and PDMS bi-layer passivation Process

The fabrication process for UVVH and PVA/PDMS passivation treatment is shown in **Figure 3.6**. The steps 4 to 6 show the UVVH process. During the UVVH process, the vacuum pump should always be turned on. The equipment used for the UVVH process is shown in **Figure 3.7**.

A dispenser printer deposited interdigitated silver electrodes onto a glass substrate. The electrodes had a gap width of 100 ± 5 mm and a gap length of 0.85 ± 0.06 mm. Following deposition, the electrodes were cured at 135 °C. For Hall measurements on separate samples, four additional silver contacts were printed on the corners of the 15 mm × 15 mm square glass substrates. ZnO NPs with a diameter of 100/20 nm (1:1, 0.2 g) were dispersed in 1.8 mL of methanol using ultrasonication. The resultant ZnO NP solution was spin-coated onto the pre-patterned glass substrate with silver contacts at 2000 rpm. The ZnO NP film was coated with 200 μL of a 15 wt% polyvinyl alcohol (PVA) solution in water, which was then dried at 50 °C for 30 minutes. A layer of polydimethylsiloxane (PDMS) solution was spin-coated onto the PVA layer at 3000 rpm and cured at 135 °C for 30 minutes. The samples were then placed in a vacuum chamber under 365 nm UV irradiation for one hour at 110 °C, then cooling for another hour. The vacuum pump was maintained throughout the process to ensure a low-pressure environment. Finally, the fabricated samples were stored in a vacuum in a dark, ambient environment.

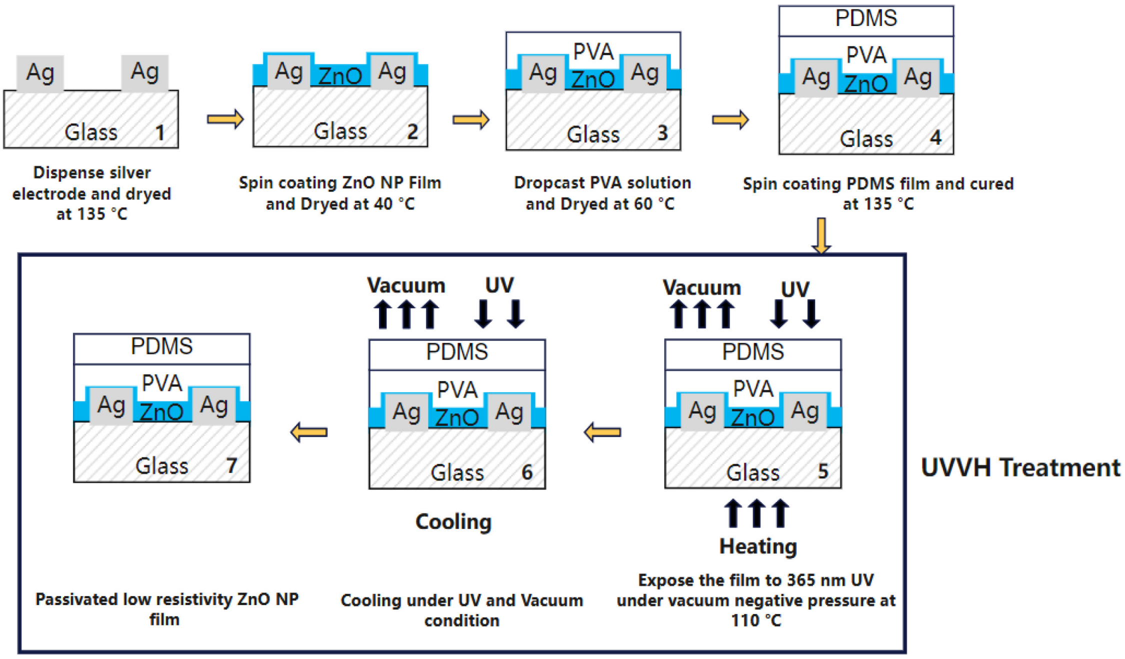

Figure 3.6: The fabrication process for the enhanced solution-processed ZnO device with PVA/PDMS passivation. Steps 4, 5, and 6 are the UVVH treatment process.

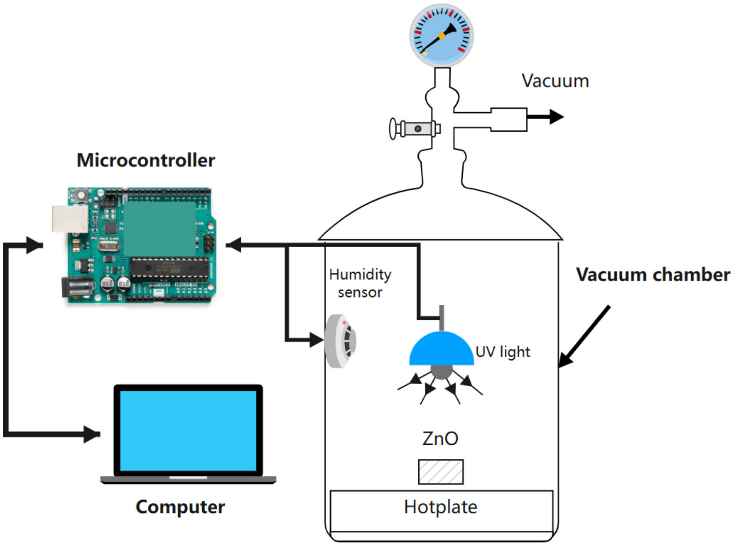

Figure 3.7: Schematic diagram of the vacuum ultraviolet light exposure system. The UV light and humidity sensor inside the vacuum box are controlled by a microcontroller. An external power supply controlled the hot-plate.

3.4 UVVH EVA Passivation Process

For the fabrication of the ethylene-vinyl acetate (EVA) film, 0.1 g of EVA stock was immersed in 1 ml of trichlorobenzene and allowed to soak for one day. Following this, the mixture was speed mixed at 3000 rpm for 1 minute and subsequently heated in a water bath at 100 °C. Once the solution was thoroughly mixed, it was evenly poured onto a glass substrate and heated in an oven at 135 °C for 1 hour to facilitate drying. Afterwards, the cooled film was carefully peeled off from the glass.

In the EVA passivation step (**Figure 3.8**), the EVA film was positioned atop the zinc oxide and silver contacts. The samples were then transferred into a vacuum chamber. Upon reaching a sufficient vacuum level, a UV LED was activated to facilitate the disconnection of oxygen molecules from the zinc oxide nanoparticles. The chamber was heated to 100 °C for 20 minutes to allow the EVA film to melt, followed by cooling in a vacuum. To ensure improved encapsulation, a hot-pressing step was performed within an argon glove box.

For the extrusion process, a fluorinated ethylene propylene (FEP) film was initially placed on a hot plate within the glove box and preheated to 135 °C. The EVA film was then placed on top of the FEP film, and pressure was applied. Finally, after the EVA film had cooled, the FEP film was removed to complete the packaging process.

3.5 UVVH EVOH Passivation Process

In Zhang's study [134], it was observed that a mixture of ZnO NPs with sizes ranging between 20-100 nm exhibited enhanced absorption of incident UV light, leading to increased removal of oxygen. In this work, two sizes of ZnO NPs (100 nm diameter NP from Merck, and 20 nm diameter NP from Thermo Scientific), were blended in a ratio of 1:1 by weight and 0.205 g of the blended particles were dissolved in 1.6 mL methanol (CH_4O, 99.8% from Merck). The solution was sonicated for 1 hour and then stored in a refrigerator at 4 °C to reduce precipitation effects due to solvent volatilisation.

For the EVOH passivation solution, 1 g Poly(vinyl alcohol-co-ethylene) (PVA-co-PE) with ethylene 32 mol% (Merck) and 10 mL dimethyl sulfoxide (DMSO from Merck) was stirred and heated at 80 °C on the hot plate under vacuum conditions for 4 hours. The EVOH solution is applied directly onto the ZnO film during the fabrication process.

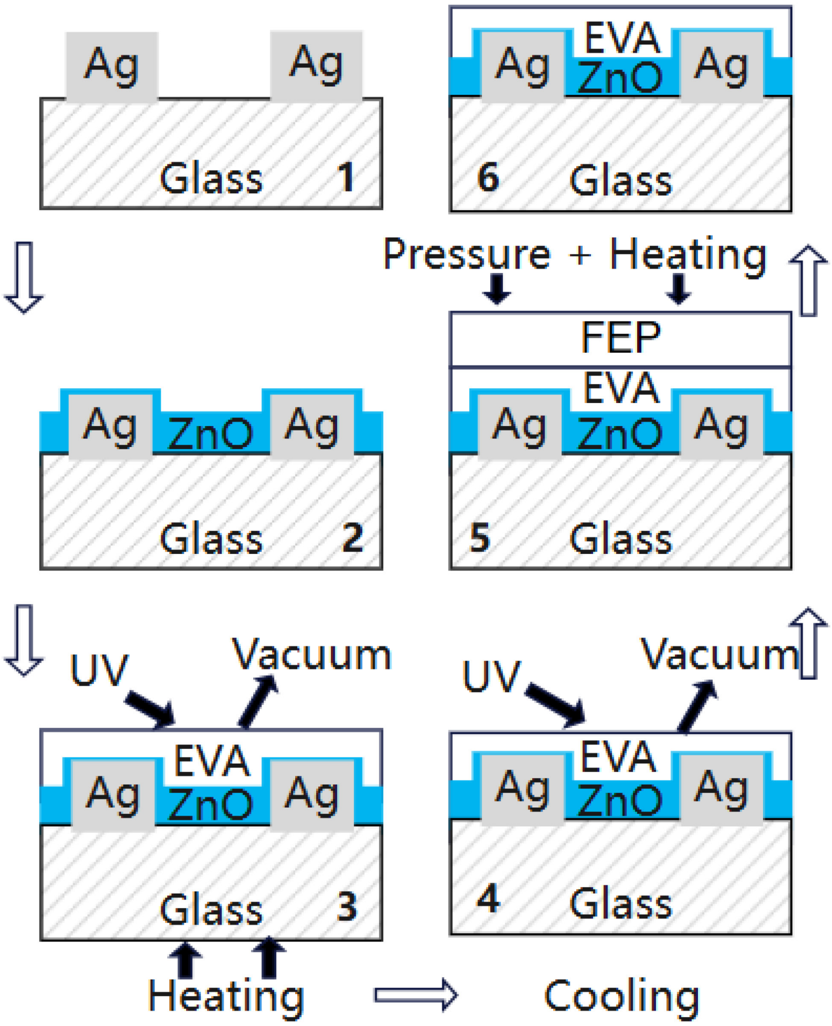

Figure 3.8: The fabrication process for the enhanced solution-processed ZnO device with EVA passivation.

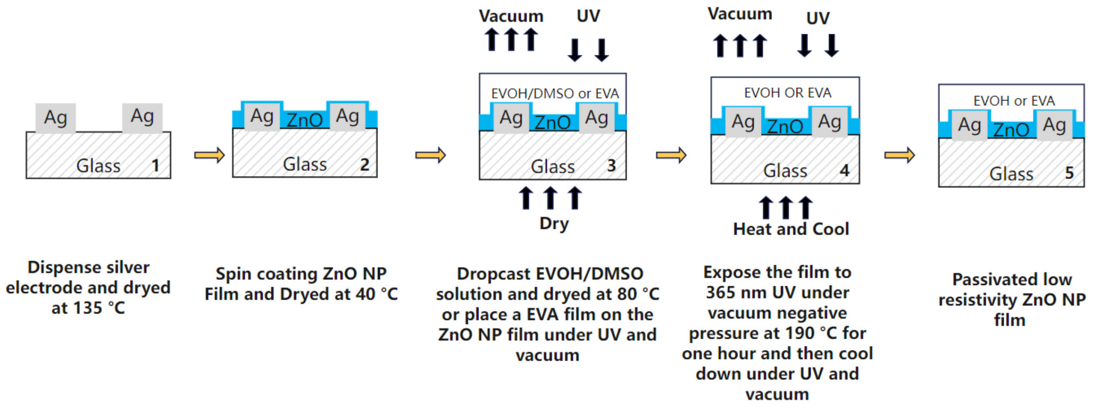

Figure 3.9: Schematic fabrication process flow for UVVH process and EVOH passivation. Starting from dispenser printing interdigitated silver electrode, spinning coating ZnO NP layer. The fabrication process in step 3 is to dry the DMSO/EVOH or hot melt the EVA film. The EVOH solution is drop cast, and the EVA film is directly applied on the ZnO surface. Steps 4 shows the passivation treatment using EVOH and EVA polymers under UV-vacuum-heat process for one hour and then cool down to room temperature under UV-vacuum condition.

For the EVOH passivation shown in **Figure 3.9**, 20-150 µL of EVOH/DMSO solution was drop-cast onto the surface of the ZnO NP, to achieve different thickness of passivation layer. The sample was then placed in the vacuum ultraviolet exposure equipment and heated to 80 °C for one hour to remove the DMSO solvent, after which the sample was heated to 190 °C for one hour. During the UVVH process, the vacuum pump was kept turned on to generate a negative pressure. EVA passivation layers can absorb 85% of the 365 nm wavelength UV light [135], and EVOH passivation can absorb 50% [136]. Finally, the sample was allowed to cool to room temperature whilst still being exposed to the UV light under vacuum.

3.6 ZnO NPs diode-like pH sensor fabrication process

Commercial carbon ink (Myldan Auto Design) was utilised for electrode printing. Zinc oxide nanoparticles (100 nm, Merck) were dissolved in methanol at a 10% weight ratio, and the resulting solution was subjected to sonication for one hour prior to spin-coating. For the preparation of the EVOH/DMSO solution, 1.5 g of poly(vinyl alcohol-co-ethylene) (ethylene 32 mol%, Merck) was dissolved in 10 mL of dimethyl sulfoxide (DMSO, Merck) and stirred at 90°C.

The titanium precursor, titanium diisopropoxide bis(acetylacetonate) (Merck), was diluted 20-fold in isopropanol (IPA) before use. Colloidal silica (30 wt% suspension in water, Merck) was diluted 100-fold in deionised water. Hydrochloric acid and sodium hydroxide were used to adjust the phosphate-buffered saline (PBS, 1×) to various pH levels, which were measured using a commercial pH sensor.

All the IV measurements were taken in darkness. The current-voltage (IV) characteristics of the sensor were measured using a Keithley 2401 Source Meter Unit (SMU). Each reading was taken five minutes after applying the pH solution to the detection area. Following measurements and evaporation of the pH solution, the sensors were rinsed with deionised water in preparation for subsequent testing.

Figure 3.10 illustrates the fabrication process of the ZnO NPs-based pH sensor. Carbon electrodes were dispenser-printed with dimensions of 2.5 mm in width and 15 mm in length onto a glass substrate. The ZnO NPs solution was spin-coated onto the substrate at 2000 rpm for 30 seconds. A layer of EVOH/DMSO (10 mm in width and 15 mm in length) was printed on the ZnO NPs and heated on a hot plate at 80 °C for one hour. The titania precursor, titanium diisopropoxide bis(acetylacetonate), was spin-coated on the ZnO NPs at 4000 rpm for 20 seconds and heated to 90 °C for 10 minutes to generate titania particle film. Metal acetylacetonate can be used to form metal oxide nanoparticles by heating [137]. The colloidal silica solution was then spin-coated onto the sample at 4000 rpm for one minute. Then, the samples were heated at 110 °C for 60 minutes to form the silica particle film. The titanium oxide and silica particle film, almost insoluble in weak acids and alkali solutions, protected the ZnO NPs while testing and cleaning pH solutions. After deposition, the samples were subjected to UVVH treatment at 120 °C for two hours, then cooled to room temperature under vacuum and UV conditions. The detection solution was applied to the ZnO NPs connected to the positive electrode. As previously reported [7], the UVVH process removes surface-adsorbed ionised oxygen, thereby reducing the resistivity of the ZnO NP film. The EVOH layer prevents the re-adsorption of oxygen, maintaining the low resistivity state (LR ZnO). Without EVOH passivation, ZnO NPs rapidly adsorb atmospheric oxygen molecules, leading to a high resistivity state (HR ZnO). **Figure 3.11** depicts the UVVH-treated ZnO NPs pH sensor.

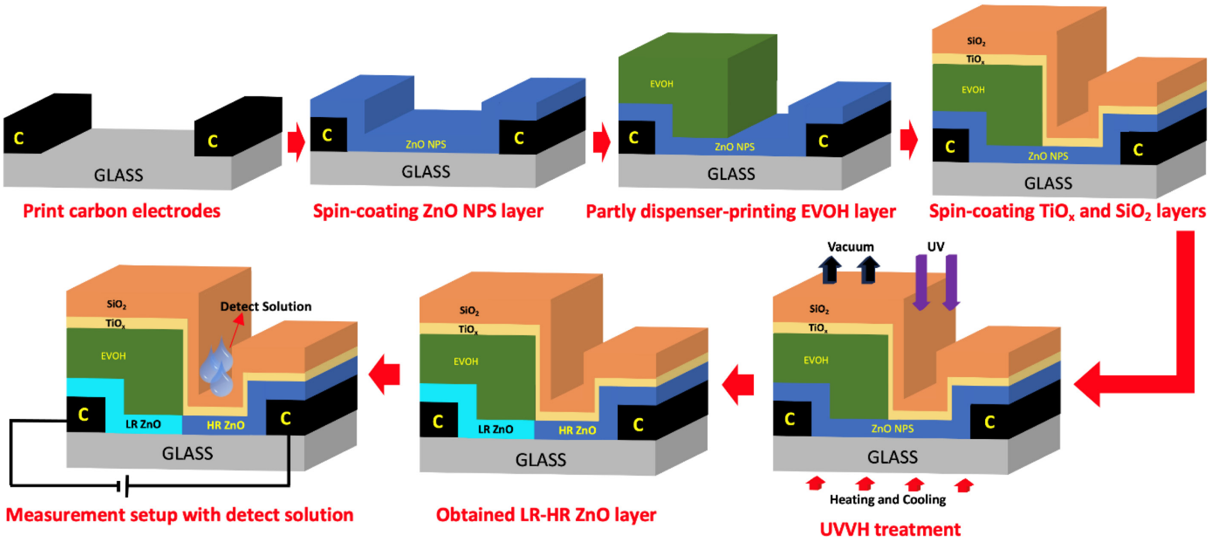

Figure 3.10: The fabrication process of UVVH-treated ZnO NPs pH sensor.

It begins with printing carbon electrodes and spinning the ZnO NPs onto the glass substrate. Dispensing prints the EVOH/DMSO solution on one side of the ZnO NPs and heated it to 80 °C. Step three shows the spinning coats of titanium oxide precursor and silica as the protection for ZnO NPs. Followed by UVVH treatment, heats for two hours and cools to room temperature. The region for the pH solution is the ZnO NPs that do not contain EVOH. Step five shows the measurement setup.

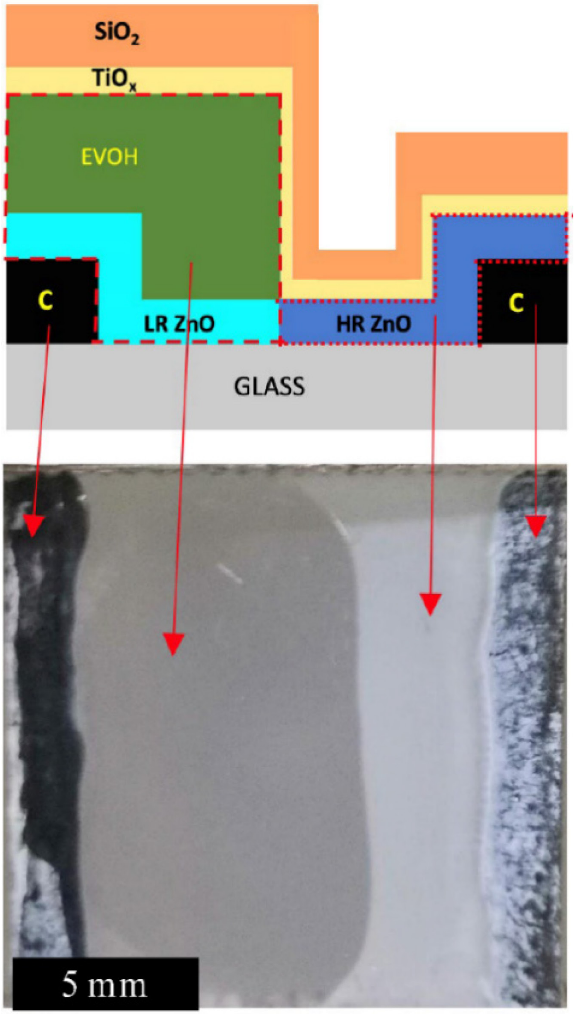

Figure 3.11: UVVH-treated ZnO NPs pH sensors. The length of the carbon electrode is 15mm. The EVOH passivation layer is a 15 mm x 10 mm rectangle. The structure was designed based on the phenomenon that adsorbed oxygen molecules can also be controlled by an electrical bias field, allowing the resistivity of ZnO at the LR-HR interface to be easily controlled by the applied voltage.

3.7 ZnO NPs intrinsic diode-like device fabrication process

To demonstrate that the intrinsic properties of the diode-like ZnO NPs enable characterisation in both solid and liquid electrode environments, The fabrication process is detailed in **Figure 3.12**. Following the deposition of ZnO NPs and EVOH with subsequent UVVH treatment, a carbon electrode solution was printed onto the high-resistance (HR) ZnO NPs (without EVOH) and dried at room temperature. The fabrication process details include: first, one carbon electrode was printed on the glass substrate with 2 x 15 mm size. Then the ZnO NPs film was spined coated on the substrate with 2000 rpm. After that, the EVOH solution was printed on the ZnO NPs film dried at 80 °C for one hour. Following by the UVVH treatment for 2 hours. After the UVVH treatment, the samples were stored in the vacuum chamber until another carbon electrode was printed on the LR and HR ZnO NPs interface. Finally, the carbon ink was evaporated under the vacuum in room temperature.

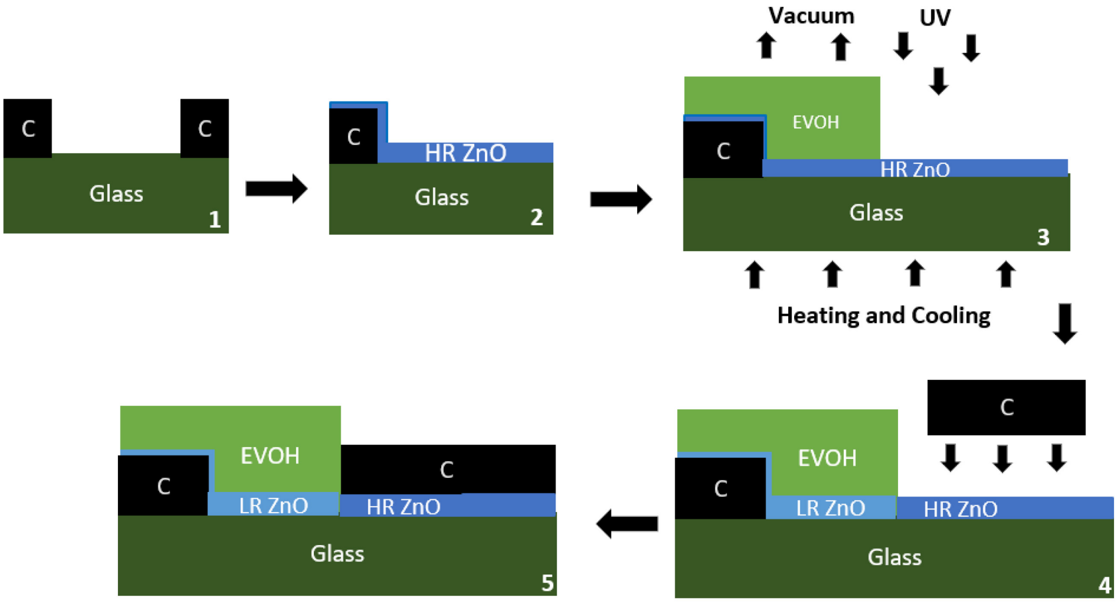

Figure 3.12: Fabrication process of the ZnO NPs diode-like device without liquid electrode.

3.8 Conclusions of Chapter 3

Chapter 3 details the fabrication equipment and process flow for the ZnO NPs device. All material deposition methods utilized are solution-based, with particular emphasis on the UVVH fabrication process. The fabrication method was developed based on the interaction between oxygen molecules and ZnO NPs affected by UV light exposure. The maximum temperature of the manufacturing process is 180 degrees Celsius, which is suitable for most flexible substrates. The vacuum level must be at least -0.98 mbar, and the vacuum pump must be running all the time to ensure uninterrupted vacuuming. The wavelength of ultraviolet light is 365 nm. This manufacturing method for reducing the resistivity of ZnO NPs has been published in the journal

ACS Applied Electronic Material and at the 50th Micro and Nano Engineering conference. The enhanced characterization of ZnO NPs achieved through this method will be discussed in Chapter 4, along with its manufacturing principles in subsequent chapters. Chapter 5 will introduce the characterization of diode-like ZnO NPs and its pH sensing application.

Chapter 4

Electrical Properties and Characterisation of UVVH Treated ZnO NPs Film

Introduction

This chapter introduces the measurement results of the ZnO NPs film with the UVVH treatment and polymer passivation. The characterisation includes scanning electron microscopy (SEM), X-ray photoelectron spectroscopy (XPS), Hall measurement, transfer length measurement (TLM), current-voltage (IV) measurement and time-based electrical stabilities. To assess the electrical stability of the ZnO NP films and prevent re-absorption of oxygen molecules, surface passivation is essential [133]. The passivation effects of water and polymers EVA, EVOH and PVA/PMDS have been individually investigated. The fabricated ZnO film has a sheet resistance of 2.5 x 10^4 Ω/□ and a thickness of 2.35 μm. After 60 days, the resistivity of ZnO NP film passivated with EVA or water molecules increased by a factor of 10^6, while the resistivity of ZnO NP passivated with EVOH and PVA/PDMS only doubled. Re-exposing the films to UV light in an atmospheric environment achieves a 10^4 order of magnitude reduction in resistance for films passivated with EVA and water molecules, whereas films passivated with EVOH experience only a 20% reduction in resistivity. The effect of the UVVH process will also be discussed in this chapter.

4.1 SEM of ZnO NPs film

The SEM image was taken using the Zeiss NVision 40 system. **Figure 4.1** shows the scanning electron microscope (SEM) image of the ZnO NPs film thickness of 2.35 µm and its porous form. The film was made using two sizes of ZnO NPs (100 nm:20 nm = 1:1) and was deposited on the glass by spin-coating the premade nanoparticle solutions at 2000 rpm for 20 seconds. The figure shows two nanoparticles differing in size. The larger, relatively blocky nanoparticles have a size of approximately 100 nm, while the smaller, relatively flocculent nanoparticles measure about 20 nm. It is evident from the figure that the two nanoparticle sizes adhere well to each other, with the smaller particles effectively encapsulating the larger ones. The SEM image was taken by Amanda Green.

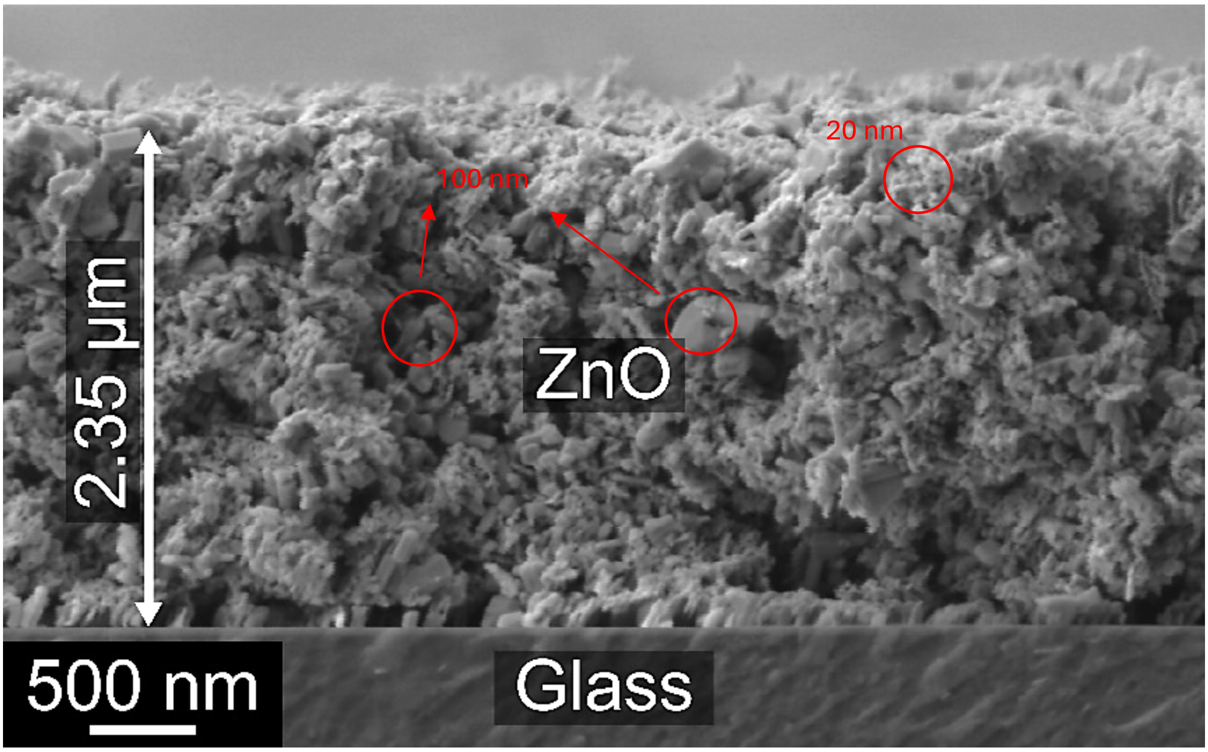

Figure 4.1: Cross-sectional SEM image of the solution-processed ZnO NP film on a glass substrate. The SEM image was taken by Amanda Green.

4.2 IV Characterization and Electrical stability of the UVVH-treated ZnO NPs film with different passivation

To avoid the influence of ambient light, all ZnO NPs samples were stored in the dark at room temperature, and measurements were performed in a dark setting. The resistance of the thin film was measured using a Keithley 2636B and Keysight B1500A source measurement unit with a Polytec MSA-400 MEMS probe station. The principles of both measurements were introduced in the previous chapter. Electrical results were obtained from two samples, with 5 measurements taken from each unless otherwise stated. All the data in the plots show the average value.

Figure 4.2a shows the resistance values of the interdigital device with the unprocessed ZnO NP film obtained for different UV-vacuum-heating processing times with measurements were taken immediately after the process. The initial resistance of the unprocessed film was 200 MΩ but drops to 5 kΩ after 10 minutes and drops further to 1.3 kΩ after 60 minutes. **Figure 4.2b** summaries the ZnO sheet resistance under different EVOH thickness after 1 and 60 days. With thinner EVOH film (10 to 40 µm), the sheet resistance was significantly increased after 60 days but for the 80 µm EVOH film passivation, the sheet resistance was stable.

Figure 4.3 shows the change in ZnO sheet resistance over time calculated from the results of the interdigitated device. The W/L ratio of the ZnO NP film is 105, and its film sheet resistance is calculated from $R_{sh} = R \times W/L$ where R is the measured resistance. The 10-80 µm EVOH represents the different passivation film thicknesses. The thickness of the EVA film is 0.8 mm. All the passivation processes are under combined UV-vacuum-heating condition. The water molecule passivated ZnO film had a sheet resistance of 0.21 MΩ/□ immediately after processing which increased to 10 GΩ/□ after one day, and finally settled at 20 GΩ/□. The resistance of the device passivated by EVA was initially around 42 kΩ/□ and this settled to 5 GΩ/□ after 3 days. The initial resistances of EVOH passivated ZnO films are: 14 kΩ/□, 12 kΩ/□, 31 kΩ/□, 68 kΩ/□ for EVOH thickness of 10, 20, 40 and 80 µm respectively. After 60 days these values had increased to 4.0 GΩ/□, 2.6 GΩ/□, 7.8 MΩ/□ and 13 kΩ/□. Table 4.1 summarizes the response of all devices following re-exposure to 365 nm UV light after 60 days.

The resistance of the devices with water passivation and EVA passivation decreased by 10^4 times after being irradiated by UV light for 10 seconds. Devices passivated with EVOH are less responsive to UV exposure. The sheet resistance would decrease by a factor of 1000 for EVOH thickness of 10 to 20 µm. However, the sheet resistance of EVOH thicknesses of 40 µm and 80 µm is reduced by a factor of 50 and 1.4. The negligible resistivity change in the device with the 80 µm thick passivation layer is due to the lack of adsorbed oxygen molecules on the surface of the ZnO NP film. This can be attributed to the thicker EVOH film reducing the UV absorption on the ZnO film.

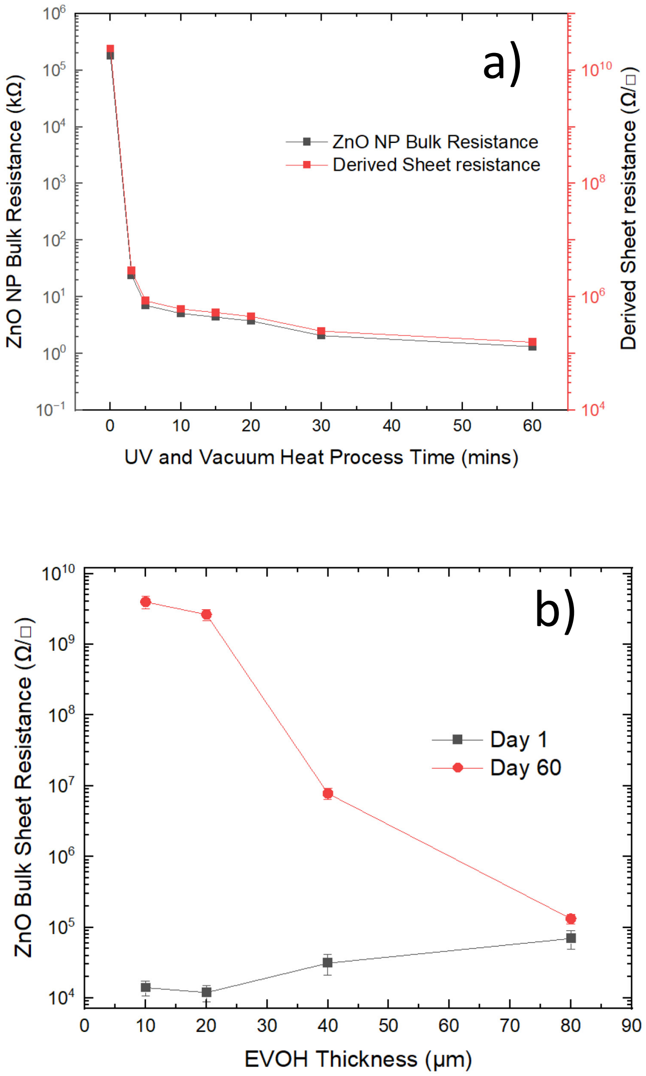

Figure 4.2: a) The resistance of interdigitated device without any passivation obtained after different UV-vacuum-heating times. The samples were exposed to the 365 nm wavelength UV

and heated to 190 °C in 10^{-2} mbar vacuum condition. b) ZnO NP bulk sheet resistance with different EVOH passivation thickness measured on Day 1 and Day 60. The lines joining the dots are for the eye guide, showing the change in bulk and sheet resistance with time and EVOH thicknesses.

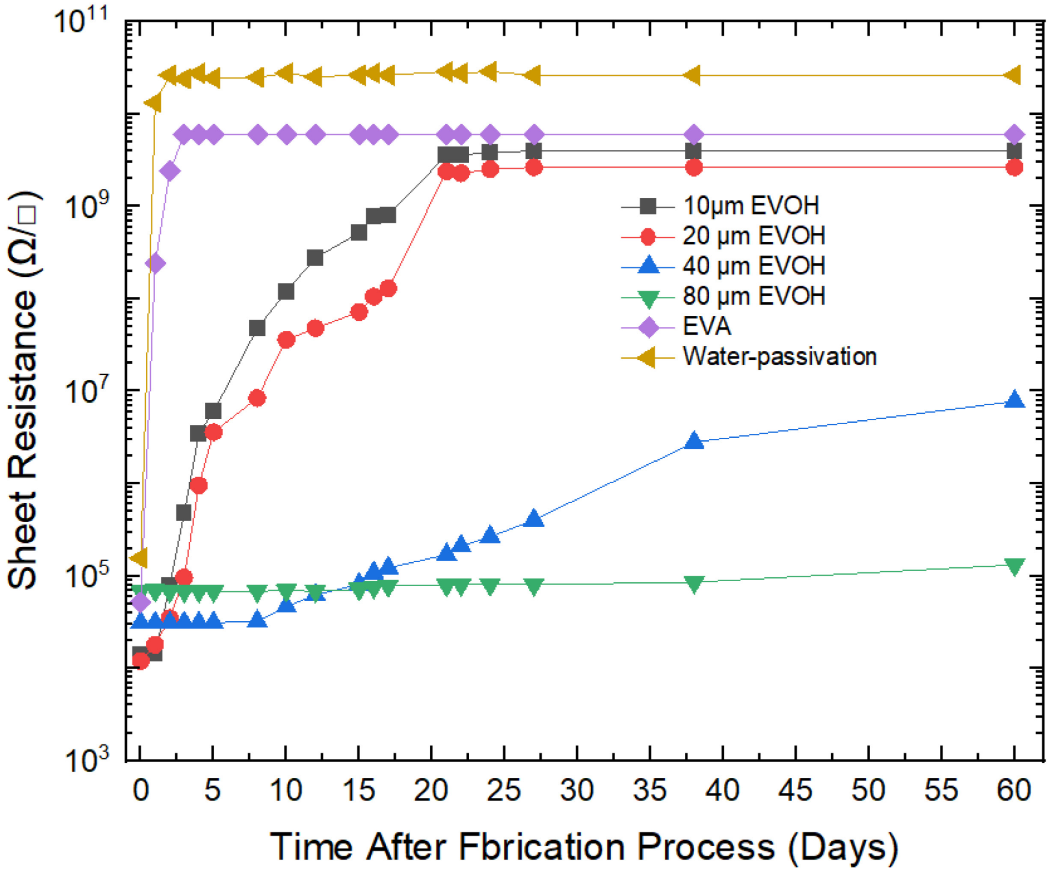

Figure 4.3: Measured time-dependent sheet resistance changes. The sheet resistance is calculated from the measured resistance of the device to its W/L ratio (**See Appendix A**). The lines joining the dots are only for eye guidance.

The I-V curve of the unpassivated and the passivated ZnO NPs film on the interdigitated silver electrode is shown in the following figures (**Figures 4.4, 4.5, and 4.6**). The interdigitated electrode structure was introduced in Chapter 3, with an effective channel width (W) and length (L) as shown in the schematic diagram **Figure 3.2a and 3.2b** in Chapter 3 with a W/L ratio of 90 ± 5 mm : 0.85 ± 0.06 mm = 105. The as-deposited ZnO NP film exhibits high resistivity and hysteresis, and the EVOH passivated ZnO NP film without a UV-vacuum-heat process shows a low current level but no significant hysteresis. The passivated ZnO NP film fabricated with the UV-vacuum-heat process shows a significantly higher current level and lower hysteresis.

The hysteresis phenomenon was also discussed in the previous literature review chapter. Greenham et al. [138] observed a similar phenomenon, attributing it to the adsorption and desorption of oxygen molecules on the surface of ZnO. A comparison of **Figures 4.4** and **4.5** reveals that the hysteresis phenomenon is considerably diminished in the presence of a passivation layer. This reduction may result from the passivation layer's ability to isolate the oxygen molecules from the ZnO nanoparticles, thereby hindering the desorption and re-adsorption of oxygen on the surface of the ZnO nanoparticles. Furthermore, a comparison of **Figures 4.5 and 4.6** indicates that while applying the passivation layer leads to a relative reduction in the resistivity of the ZnO nanoparticle film, the resistivity of the film after UVVH treatment is decreased to a greater extent.

Table 4.1: Resistance response for 365 nm UV of interdigitated devices stored for 60 days in darkness after processing.

Interdigitated devices with different passivation	**Initial ZnO sheet resistance after processing (Ω/☐)**	**ZnO sheet resistance after 60 days stored in darkness (Ω/☐)**	**Sheet resistance after re-exposure to 30 mW/cm^2 UV for 10 seconds (Ω/☐)**
10 μm EVOH	1.03×10^4	4.64×10^9	3.91×10^6
20 μm EVOH	1.23×10^4	3.26×10^9	1.93×10^6
40 μm EVOH	2.31×10^4	2.21×10^6	4.31×10^5
80 μm EVOH	6.00×10^4	1.11×10^5	0.88×10^5
800 μm EVA	4.56×10^4	5.78×10^9	1.82×10^5
Water passivation	6.31×10^4	2.42×10^{10}	6.08×10^6

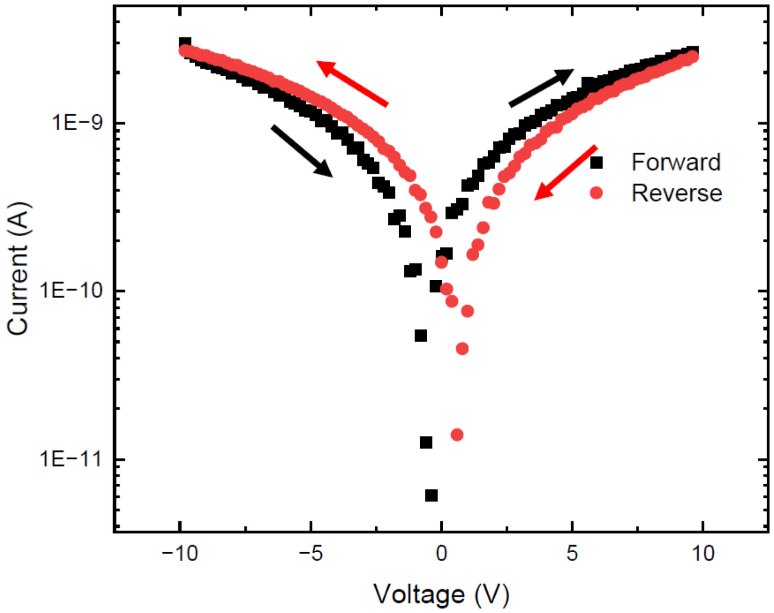

Figure 4.4: Measured I-V curve for the ZnO NP film with the interdigitated silver electrode, without EVOH passivation or UVVH process.

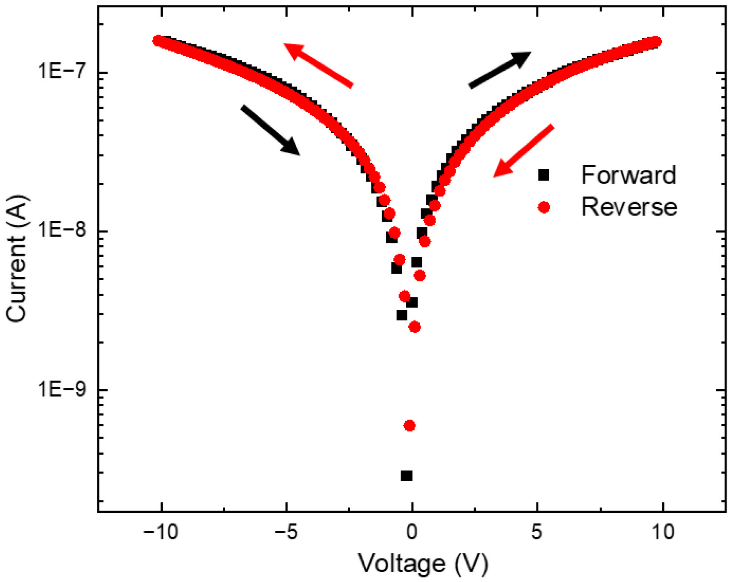

Figure 4.5: Measured I-V curve for the ZnO NP film with the interdigitated silver electrode, with EVOH passivation but without UVVH process.

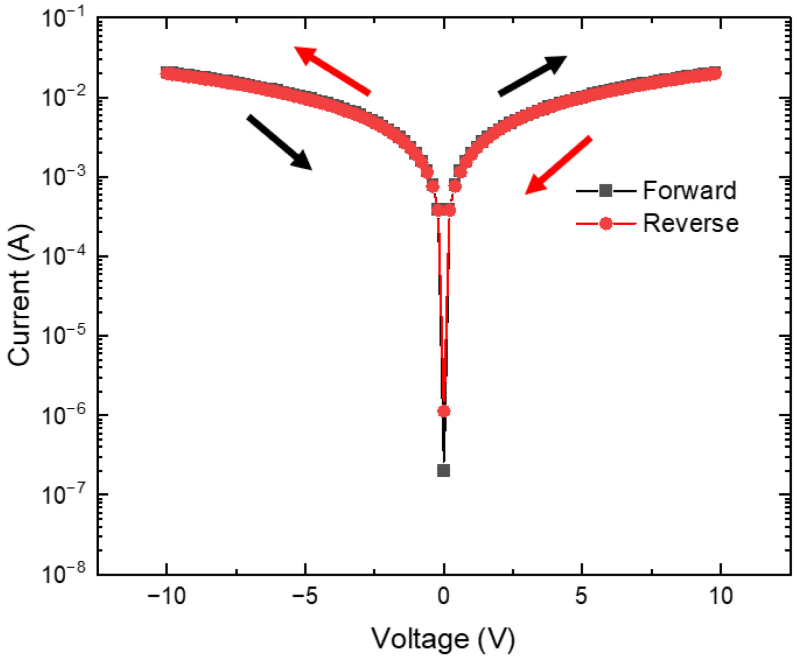

Figure 4.6: Measured I-V curve for the ZnO NP film with interdigitated silver electrode, with EVOH passivation and UVVH process.

It can be seen from **Table 4.2** that the resistivity of ZnO deposited from solution is significantly higher than that deposited from clean room. The resistivity of solution-processed ZnO NP film is 3 to 5 orders of magnitude higher than that of films deposited using other techniques. Variations in resistivity are further influenced by specific solution and post-processing methodologies used. The resistivity of ZnO NP film passivated by EVOH and with UV-vacuum-heat process shows similar resistivity with the ALD deposited ZnO film and significantly lower than other deposition methods. This may be due to the deposition of oxygen molecules on the surface of ZnO nanoparticles, which restricts the movement of electrons inside them [91]. However, the light conditions during the measurement and the stability of the material over time are not given in the literature. No matter how it is deposited, if ZnO is exposed to air for a certain period of time, its resistance will rise due to the contact with air. So, to ensure the stability of the device, ZnO must be passivated. According to the previous study [22], Al_2O_3 and HfO_2 insulator layer are used to protect the ZnO channel. However, the fabrication process of this layer is complex and requires several steps in the cleanroom. In principle, the protection layer should be as thin as possible to ensure the sensitivity of the device.

Table 4.2: Comparison of ZnO Films Deposited by Different Methods

Deposition method	**Sheet resistance (Ω/□)**	**Thickness (nm)**	**Carrier concentration (cm^{-3})**	**Resistivity (Ω.cm)**
ALD[139]	1.3×10^5	80	1×10^{17}	1.04
Atmospheric pressure chemical vapour deposition[140]	1.8×10^7	300	6.55×10^{14}	2460
Solution-processed ZnO with N2 annealed [141]	9.9×10^8	100	1.7×10^{14}	9900
Solution-processed ZnO with O2 annealed [141]	3.8×10^{10}	100	1.6×10^{14}	380000
Ink-jet printed ZnO [60]	5×10^9	81		40500
ZnO film in this work with EVOH passivation	2.5×10^4	2350	2.28×10^{17}	5.8

As shown in **Figure 4.7**, the time-dependent results for the PVA/PDMS passivated ZnO NPs film are similar to those for the EVOH passivated one. This device employs the previously mentioned interdigitated silver electrodes. A PVA aqueous solution is drop-cast onto the surface of the ZnO NPs film and subsequently dried. Following this, pre-stirred PDMS at a 10:1 ratio is spin-coated onto the ZnO NP film at a speed of 3000 rpm. The manufacturing process is completed with a UVVH treatment. PVA serves as an oxygen-isolating polymer and contains a substantial number of hydroxyl groups. After the ZnO NPs undergo UVVH treatment, the PVA passivation layer can maintain low resistivity over an extended period. This observation underscores the critical role of the passivation layer's oxygen-isolating properties. Similar to EVOH, PVA's abundant hydroxyl groups may enhance its adhesion to ZnO NPs. The thickness of the PVA/PDMS film is only 30 μm, yet the resistivity of the passivated ZnO NPs remains almost unchanged for up to 3 months. This stability may be attributed to PVA's superior oxygen isolation performance. However, due to its water-soluble nature, PVA does not adequately fulfil the passivation requirements in aqueous solutions.

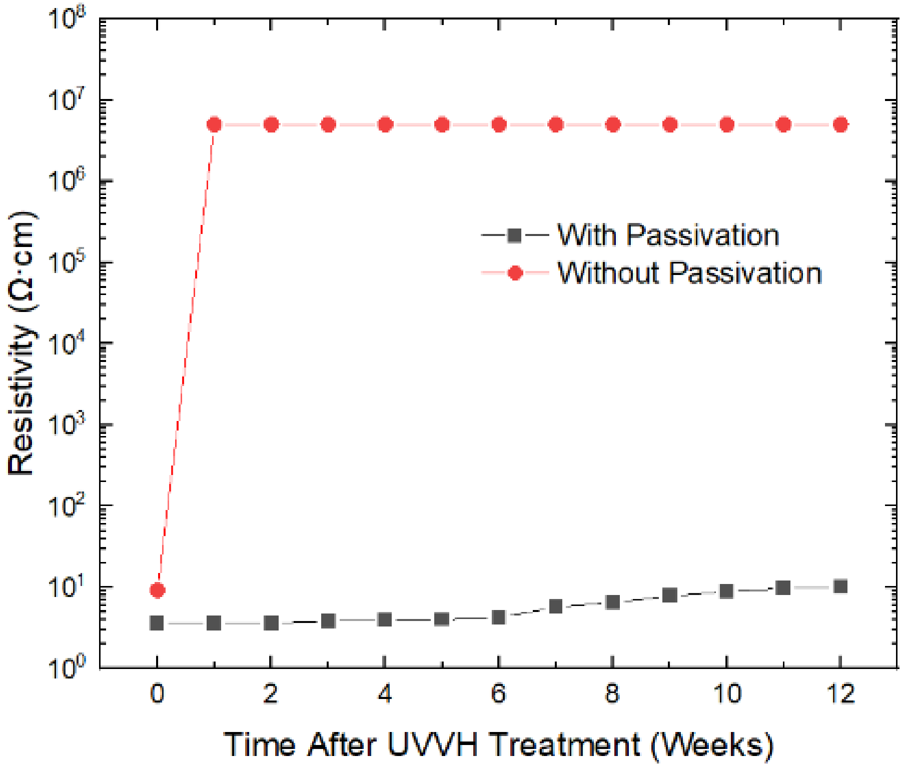

Figure 4.7: The resistivity (derived from interdigitated devices) 12 weeks after UVVH treatment for PVA/PDMS passivated and non-passivated ZnO NP film.

4.3 TLM and Hall measurement results

The sheet resistance of the unprocessed ZnO film (without UV-vacuum-heat process) taken by TLM immediately after deposition (see **Figure 4.8**) was 12 GΩ/□ and the contact resistance was 100 MΩ. The processed ZnO with water molecule passivation had a sheet resistance of 9 MΩ/□ and a contact resistance of 0.2 MΩ. The processed ZnO with EVA passivation exhibited a sheet resistance of 30 kΩ/□ and a contact resistance of 0.6 kΩ. The processed ZnO with the 10 µm thick EVOH passivation had a sheet resistance of 25 kΩ/□ and contact resistance of 0.5 kΩ. These results show broad agreement with the resistivity measurements obtained from the interdigital devices (see **Table 4.1**).

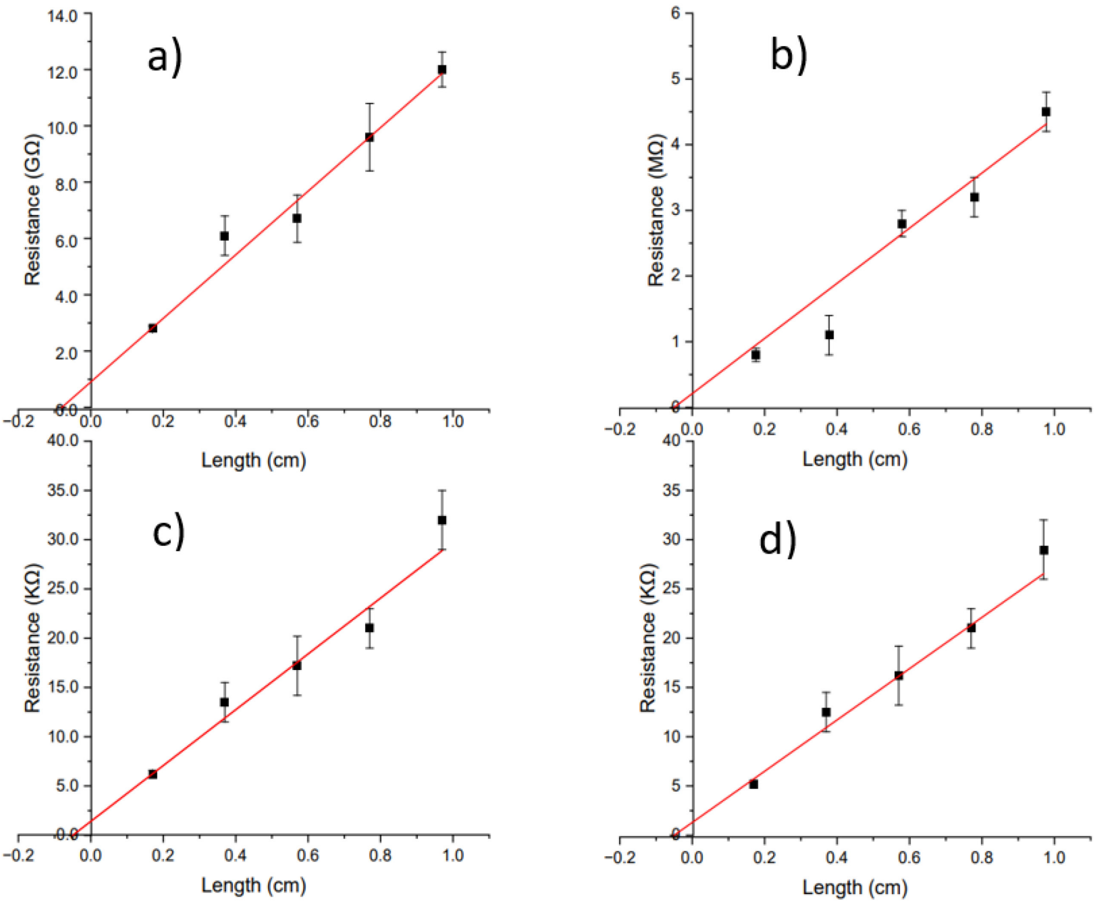

Figure 4.8: TLM for the ZnO NPs film with 1 cm width and 0.2 to 1 cm length a) as deposited b) with 365 nm vacuum UV and water c) with UVVH EVA passivation d) with UVVH EVOH passivation. The slope of the red line represents the sheet resistance of the film. The intercept of y-axis is twice the contact resistance of the silver electrode and the semiconductor film. The intersection of the x-axis is the transmission length.

The resistivity and carrier concentration of the thin film are measured using an HL5500 Hall measurement system. **Figure 4.9** illustrates the Hall effect measurement results for ZnO NP films categorised by the presence or absence of passivation and the UVVH treatment. The resistivity and carrier concentration of the passivated ZnO NP with UVVH treatment are 3.63 Ω·cm and 1.37 x 10^{17}/cm^3, respectively. The values of the passivated film without UVVH treatment are 6115 Ω·cm and 2.83 x 10^{15}/cm^3. The values of the non-passivated film with UVVH treatment are 16.76 Ω·cm and 4.21 x 10^{16}/cm^3. The values of the non-passivated film without UVVH treatment are 3.21 x 10^6 Ω·cm and 2.13 x 10^{13}/cm^3.

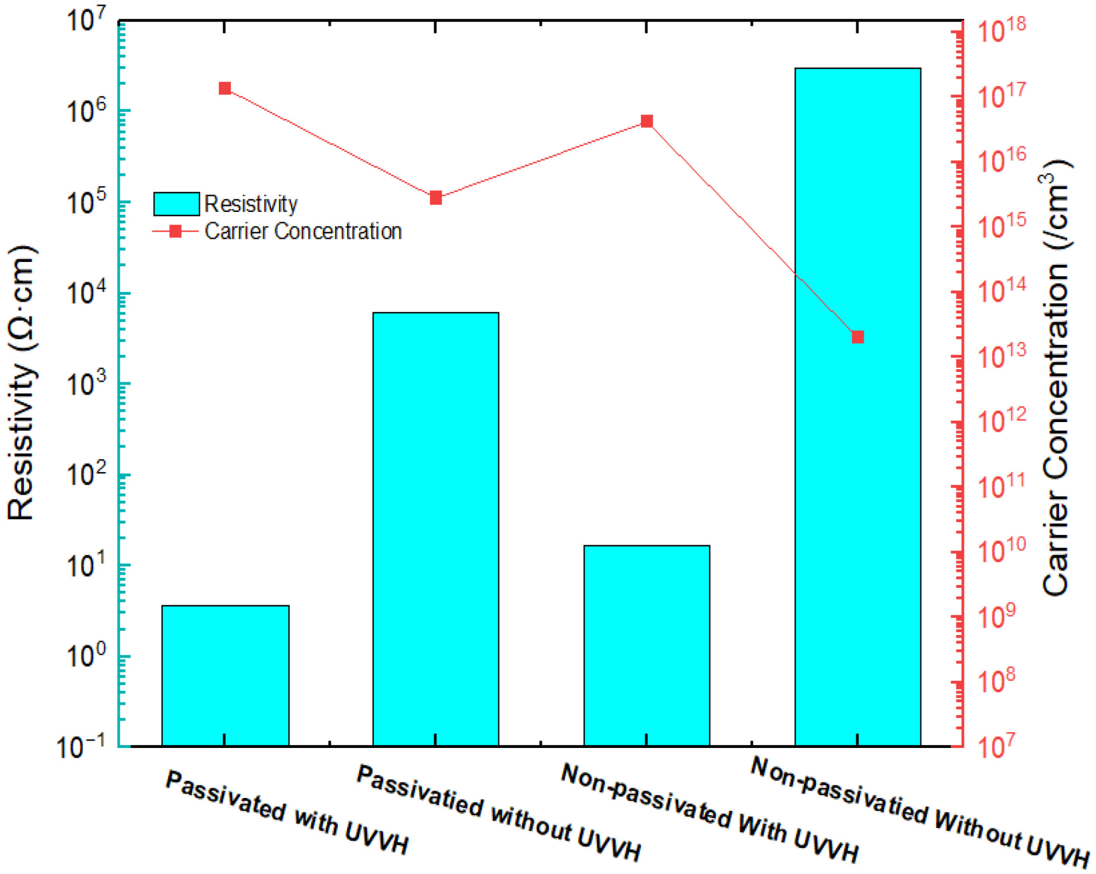

Figure 4.9: Hall measurement result for the ZnO NP film with and without passivation or UVVH treatment

4.4 Discussion of UVVH treatment – surface oxygen molecules adsorption and released

It has been observed that reducing the oxygen partial pressure during the fabrication process increases the conductivity of ZnO. This can be due to the lower oxygen partial pressure resulting in more oxygen vacancies in the ZnO lattice structure. Oxygen vacancies have long been considered to be one reason why ZnO exhibits n-type semiconducting properties [52]. The calculation based on first principles shows that oxygen vacancies are located at very deep energy levels, are not shallow donors, and cannot, therefore, provide n-type conduction [52] [142]. However, recent research shows that the oxygen vacancies on the surface of the ZnO NP easily absorb the oxygen molecule from the ambient environment and then trap the electron in the nanoparticle [117].

According to the theoretical model proposed by Saputra et al,[117] the ZnO surface with oxygen vacancies, or zinc oxygen dimer vacancies, can quickly adsorb oxygen molecules and convert them into two individual oxygen atoms. The oxygen atoms will trap the free electron and become oxygen ions, thereby reducing the carrier concentration inside the ZnO film itself and increasing its resistivity.

Experiments investigating the electrical characteristics of nano ZnO under UV light exposure and in the presence of water have yielded a consistent hypothesis which is oxygen molecules adhere to the ZnO NP, binding with electrons [24], [91], [93]. Ultraviolet (UV) light can transiently release ionized oxygen molecules from the surface of ZnO NPs, thereby increasing the majority carrier concentration, with water molecules facilitating the maintenance of this concentration. The following equation can be used to define this phenomenon [25], [91], [94]:

$$O_2\,(g) + e^- \rightarrow O_2^-\,(ad) \qquad (4.1)$$

$$hv \rightarrow e^- + h^+ \qquad (4.2)$$

$$O_2^-\,(ad) + h^+ \rightarrow O_2\,(g) \qquad (4.3)$$

$$H_2O + 2Zn + O_v \rightarrow 2(Zn - OH) + V_o + 2e^- \qquad (4.4)$$

Where O_2 (g) and O_2^- (ad) are oxygen molecule in the gas phase and adsorbed oxygen molecule on the ZnO surface, hv is the UV energy, e^- and $h^+$are electron and hole. O_V is the oxygen in lattice, Zn - OH represents the zinc atoms with adsorbed hydroxyl groups, V_o represents the oxygen vacancy. When ZnO is exposed to ultraviolet light, its internal electrons transition and leave holes in the valence band, forming electron-hole pairs. The formed holes migrate to the ZnO surface and neutralize the electrons bound by the oxygen molecules, thereby releasing the oxygen molecules, and leaving behind the electrons that have transitioned. The carrier concentration increases accordingly, and the resistivity of the ZnO decreases macroscopically. When the UV exposure is stopped, the oxygen molecules in the ambient environment will combine on the surface of ZnO to begin to reduce the carrier concentration again. Vidor et al [24] shows that if the ZnO is exposed to a higher relative humidity environment, the resistance of the ZnO will decrease significantly. After exposure to UV and moisture, if it is stored in a high humidity environment, the ZnO NP film will maintain a greater carrier concentration and lower resistance than a device stored in a dry environment [24]. This is due to the water molecules adsorbed on the surface of ZnO which reduce the number of oxygen molecules adsorbed on its surface. However, the water molecules cannot be easily retained on the surface of the ZnO and will evaporate unless a high environmental humidity prevents this.

Figure 4.10 presents the schematic diagram explaining the impact of ZnO NPs surface exposure to 365 nm UV radiation in vacuum condition, as described from literature [24], [118], [119]. The released oxygen molecules in gas phase diffuse into the environment. In this process, applying heat enhances the release rate of oxygen molecules.

The presence of the vacuum diminishes the concentration of released oxygen molecules at the ZnO NP surface. **Figure 4.10** also illustrates the transient use of water molecules as a passivation layer at the ZnO NP surface; however, this effect is short-lived as the water molecules evaporate, leading to oxygen re-adsorption. The lower path in **Figure 4.10** illustrates the application of EVOH polymer passivation to prevent oxygen molecule re-adsorption, preserving the ZnO electron concentration. In addition, the passivation layer with lower oxygen permeability maintains the higher ZnO electron concentration for a longer duration. Regarding the effect of water molecules on the conductivity of ZnO film, Liau et al [94] also proposed that water molecules will be dissociated into hydroxyl groups after contacting and adsorption on the ZnO film surface and increase the electron concentration [94]. The research of Rawal et al on the interaction between water molecules and ZnO NP proposed that the dangling bonds exist on the surface of ZnO NP will dissociate the adsorbed water molecules [143].

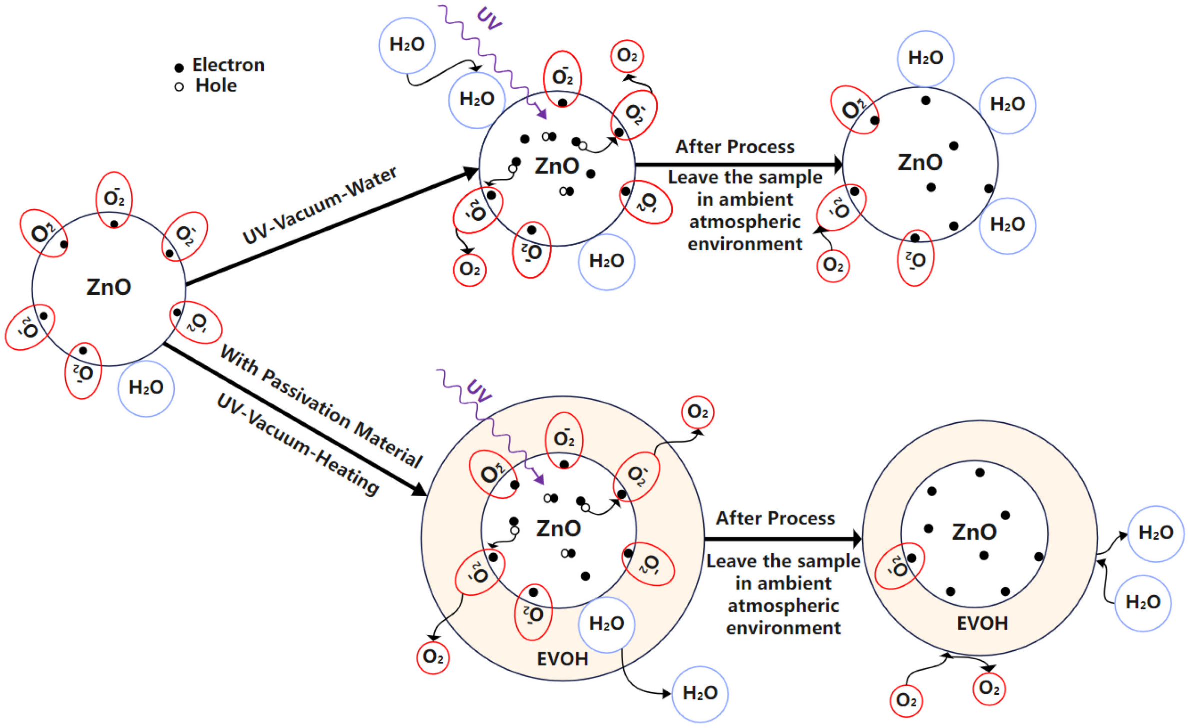

Figure 4.10: Schematic diagram of the release of carriers bound by oxygen on the ZnO surface by UV exposure in vacuum condition. Top path (derived from literature [24], [118], [119]) shows the interaction of water molecules attached to the surface of the nanoparticles and after leaving in ambient atmospheric condition, the oxygen molecules readily re-absorbed on the surface of ZnO. The bottom path shows the polymer passivation material (EVOH) that are more effective in preventing oxygen from being re-adsorbed.

X-ray photoelectron spectroscopy (XPS) was used to examine the surface composition of both non-passivated and passivated ZnO films. The XPS measurement was taken and in collaboration with Ben. Rowlinson. An $Al_{K\alpha}$ X-ray source with a photon energy of 1486.6 eV is used. All spectra have had standard C1s surface charging corrections applied at 284.8 eV.

The non-passivated sample has been left in ambient conditions for 60 days. The passivated sample uses a thickness of approximately 800 nm of EVOH, which is processed using the UV-vacuum-heating treatment, immediately before being placed in the XPS vacuum chamber. The EVOH layer is etched using an Ar ion gun in-situ until the Zn2p and O1s spectral peaks are present in the survey measurement. High-resolution XPS characterisation of the O1s and Zn2p regions are then made. The Zn2p spectra for the passivated and non-passivated samples are shown in **Figure 4.11**, with O1s spectra shown in **Figure 4.12**.

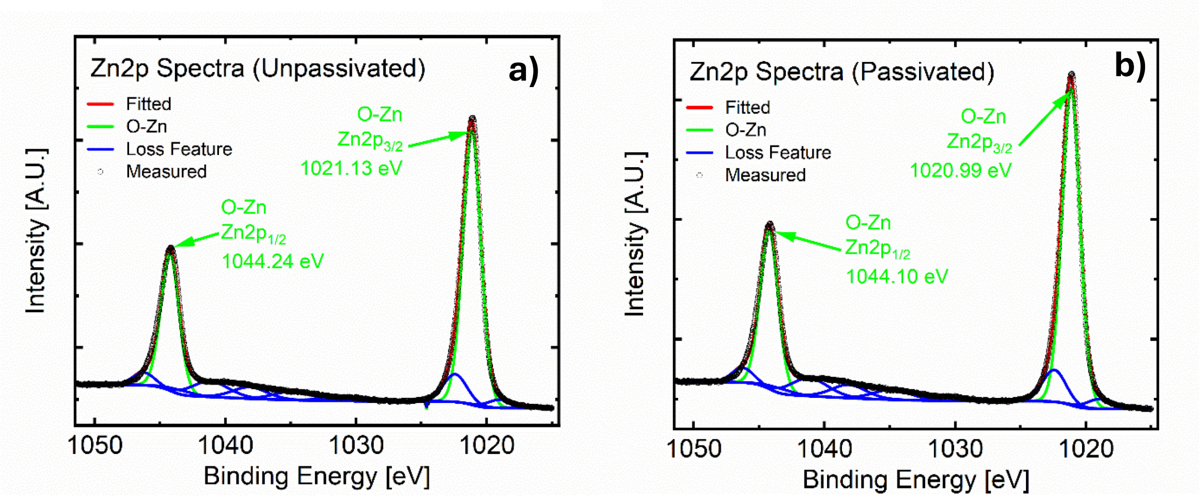

Figure 4.11: Measured XPS results for Zn2p and O-Zn spectral peaks for a) unpassivated ZnO NP film b) passivated ZnO NP film.

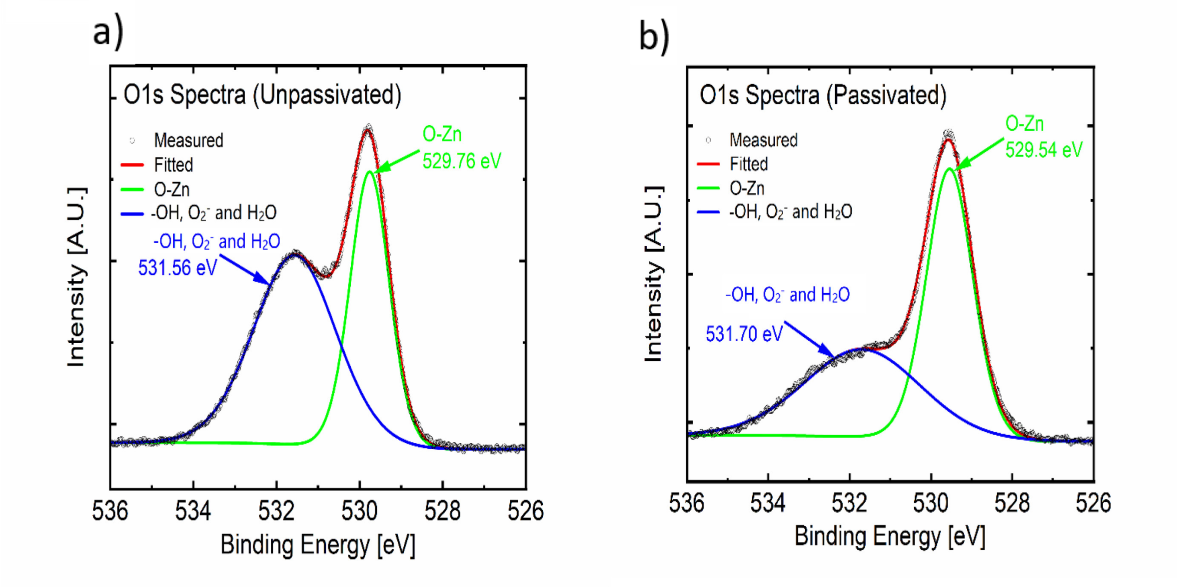

Figure 4.12: Measured O 1s XPS spectra of ZnO NP film, a) without EVOH passivation and UV-vacuum-heat process b) with the passivation and the UV-vacuum-heat process.

The de-convoluted core level O1s spectrum in **Figure 4.12a** for a non-passivated EVOH sample shows a distinct primary peak at 529.76 eV, characteristic of the O-Zn bond. A secondary peak at 531.56 eV is attributed to a combination of surface O_2^- , H_2O, and -OH hydroxyl groups that arise from atmospheric moisture adsorption [144], [145]. The EVOH-passivated sample in **Figure 4.12b** has a primary peak at 529.54 eV and a broad secondary peak at 531.70 eV, arising from O-Zn bond and -OH groups, respectively. Secondary peaks in core level O1s are often ascribed to oxygen vacancies, although there is recent evidence by Frankcombe et al. [144] that suggests little evidence of oxygen defects in the bulk region of ZnO and more likely to be due to interaction of the hydroxyl from H_2O or surface oxygen on the ZnO surface. As such, the secondary peak at higher binding energies of 531.56 eV for the non-passivated sample and 531.70 eV for the EVOH-passivated sample are interpreted as -OH groups, with a characteristic binding energy 1-2 eV higher than that of the O-Zn bond. 1 The atomic ratio of O-Zn to -OH at the measured surface is 40.8% O-Zn to 59.2% -OH for the non-passivated sample versus 55.4% O-Zn to 44.6% -OH for the EVOH-passivated. This indicates a reduction in the concentration of -OH groups, surface O_2^- and H_2O in the EVOH-passivated sample and demonstrates the effectiveness of simultaneous UV-vacuum-heat treatment.

The TLM results are summarized in **Figure 4.13** with the full datasets being supplied in the supplementary material section. **Figure 4.13a** shows the sheet resistance of the different passivation methods when processed under UV-vacuum conditions. The water passivation reduced the ZnO sheet resistivity by approximately 10^3 times compared to the unpassivated ZnO NP, which is consistent with chemical equations 4.1 to 4.4. The use of UV-vacuum-water process increases the condensation of the water vapor on the surface of the ZnO NP film, leading to a lower sheet resistance compared to Vidor et al. [24] in which their ZnO was processed at atmospheric pressure. Notably, the TLM results for the two polymer passivation layers yielded similar results reducing the resistance by approximately 5×10^5 times which is consistent with results from the interdigitated devices shown in Table 4.1. In contrast, for the water passivated ZnO NP film the TLM results do not agree with the interdigitated device due to the timing of the measurements. The interdigitated device was measured immediately after processing, whereas the TLM structure was measured 1 hour after the UV-vacuum-water process. The delay in the TLM measurement causes re-adsorption of oxygen, increasing the ZnO NP sheet resistance. The UV-vacuum-water process has a greater oxygen permeability through the polymer layers, which leads to a higher initial sheet resistance. **Figure 4.13b** shows the contact resistance of the as-deposited, UV-vacuum-water treated ZnO NPs, EVA and

EVOH passivated ZnO NPs. A consistent transfer length of 0.05 mm extracted from the TLM results for all ZnO NP passivated films indicates a reliable ohmic contact between the solution-processed ZnO NPs and the silver electrodes. These contacts are unaffected by the passivation materials or the UV-vacuum treatment process.

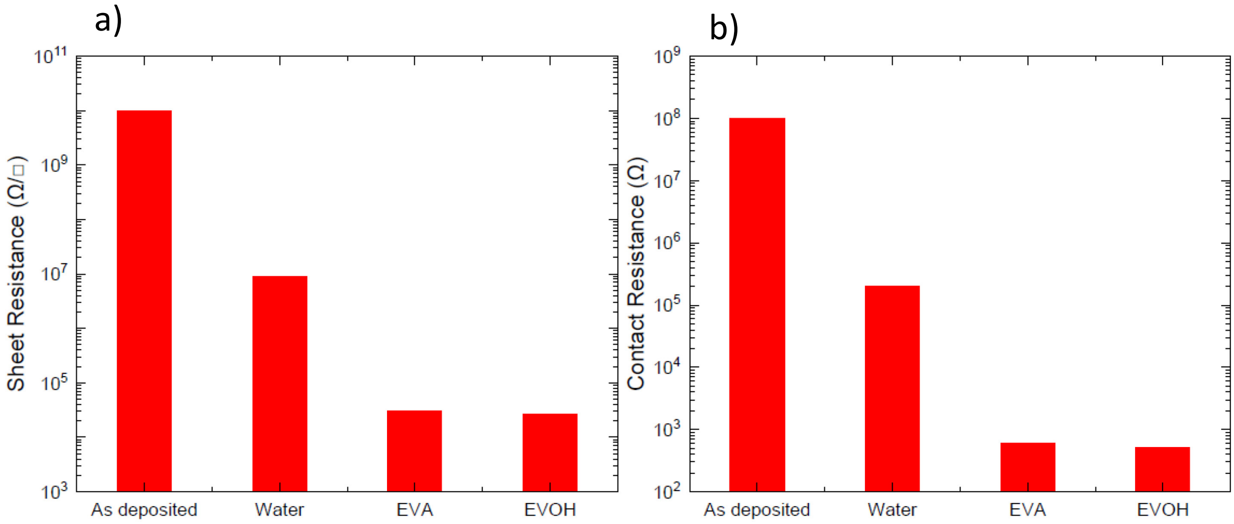

Figure 4.13: a) Sheet resistance and b) contact resistance results extracted from TLM measurement.

Regarding the ZnO NP film's long-term electrical stability investigation, the electron carrier concentration of the EVA passivated ZnO NP film reduces to a stable level after 4 days. This is due to the higher level of oxygen permeability of EVA compared with EVOH (the oxygen transmission rate of EVA is 180 cm^3 mm/ m^2 day atm [129], while the rate of EVOH is 0.1 cm^3 mm/ m^2 day atm[129]). Also, the bond between the ZnO film and the EVA is not as strong as for the EVOH due to the different processing methods with the EVA being applied as a dry film and then heated to 190 °C. The hydroxyl functional groups in EVOH enable a much stronger bond to the ZnO surface and contribute to the lower sheet resistance of the EVOH passivated ZnO NP films.

As shown in Table 4.1, upon re-exposure to UV light after 60 days, the resistivity of ZnO NPs passivated by EVA remained lower than that of unpassivated films when measured one minute after re-exposure. This indicates that the oxygen molecules are very quickly re-adsorbed on the surface of the unpassivated films whereas the EVA does slow down the reabsorption process.

Although EVOH significantly reduces oxygen transmission rates, it only limits oxygen migration to the ZnO NP film surface, and its film thickness has a significant impact on its effectiveness. For EVOH films of 10 μm and 20 μm thickness, the resistance begins to increase after 2 days, underscoring the inability of these thin layers to provide adequate passivation. The 80 μm thick EVOH-ZnO device exhibited minimal resistance increase even after 60 days, demonstrating superior stability. Note that the initial resistance of thicker EVOH passivated interdigitated ZnO devices tends to be higher. This could be attributed to reduced UV illumination efficacy in removing oxygen molecules from the ZnO surface during passivation. Additionally, the DMSO solvent used in the EVOH solution does etch the ZnO film during the passivation process, resulting in thinner film thicknesses. The thicker the EVOH, the longer the ZnO is exposed to the DMSO before it evaporates, resulting in higher initial resistance compared with thinner EVOH layers.

The conductivity of the film can be influenced by the carrier concentration and the mobility. As shown in the SEM image of **Figure 4.1**, the porous nature of ZnO NP film allows oxygen molecule to incorporate into it, resulting in surface depletion. This effect reduces the carrier concentration and mobility while considerably increasing film resistivity. The photoresponse of the ZnO NP film can be explained by [146], (i) the rapid photogeneration and recombination of electron-hole pairs, and (ii) the slow adsorption of the oxygen molecule. With the passivation and UV-vacuum-heat process, secondary recombination can be very slow, as a result, the ZnO NP film has a higher carrier concentration and mobility.

4.7 Conclusions of Chapter 4

This chapter has demonstrated a novel fabrication method that enhances the electrical properties of solution-processed ZnO NP film using UV exposure and heating the sample in a vacuum environment. This method has reduced the resistance of the solution processed ZnO NP film to levels comparable with chemical or physical vapor deposited films. This enhancement can achieve long-term stability with a solution processed EVOH passivation layer of 80 μm thickness. The resistivity of the film was reduced to 5.9 Ω·cm, which is comparable to the vapor deposition film. The fabrication method proposed in this paper can initially minimise the influence of oxygen on ZnO NP and slow down any subsequent adsorption effect. In the comparison of the two passivation materials (EVA and EVOH), it can be concluded that it is beneficial for any passivating polymer to have hydroxyl functional groups to bond closely to the ZnO surface and contribute to the reduction in resistance. The oxygen transmission rate through the passivation layer could be further improved by adding inorganic materials that have lower oxygen transmission rates. The inclusion of glass flakes or nanoparticles, for example, would make the path the oxygen molecules travel much longer. The addition of such materials will, however, alter the mechanical properties of the passivating film. Solution processing is inexpensive, and the materials used are environmentally sustainable. ZnO films are widely used to monitor UV and to as a chemical sensor to detect reducing substances. One drawback of using the thick EVOH passivation layer is the reduced sensitivity to these measurements, and the EVA passivation may be better suited to photoresistor applications. Low-resistivity solution-processed ZnO NPs can be particularly sensitive to substances that dissociate due to hydrogen bonding, making them suitable for use in biochemical sensors and field effect transistors.

Chapter 5

Characterisation of the ZnO NPs diode-like pH sensor

Introduction

The pH value of human body fluids serves as a crucial biological indicator with significant implications for clinical diagnosis. The normal pH range of human blood is between 7.3 and 7.5. A pH level below 7.3 is indicative of acidosis, while a pH level above 7.5 suggests alkalosis [26]. In the context of cancer diagnosis, the extracellular environment of cancerous cells exhibits a slightly lower pH than normal cells due to its acidic nature [34]. Nonetheless, the sensitivity of traditional pH sensors is limited by the Nernst limit (59 mV/pH), which can restrict diagnostic efficacy. Consequently, overcoming the Nernst limit to develop high-sensitivity pH sensors has garnered considerable research interest. Recent advancements have focused on developing pH sensors that utilize metal oxides, such as ZnO [29], RuO_2 [30], WO_3 [31] and IrO_2 [32] as sensing layers.

According to the results from section 4, the UVVH process can significantly diminish the resistivity of ZnO NPs. Additionally, passivation with ethylene vinyl alcohol (EVOH) polymer considerably enhances electrical stability. The UVVH process effectively removes ionised oxygen molecules adsorbed on the surface of ZnO, exposing a more significant number of adsorption sites, which increases the operational efficiency of ZnO NP pH sensors.

This chapter presents a novel pH sensor utilising UVVH-treated solution-processed ZnO NPs devices beyond the Nernst limit. The device demonstrates diode-like electrical behaviour, with its threshold voltage exhibiting a dependency on the pH of the tested solution. The operating principle is also analysed, and a mathematical model is presented to characterise its electrical behaviour. Two types of ZnO NPs films (100 nm and 100/20 nm) were both tested and the results will be shown in the following section. According to Yujian et al. work [106], When the amount of hydrogen ion species participating in the reaction is greater than the number of electrons transferred due to the chemical reaction, the sensitivity of the device will exceed the Nernst limit. The mechanism of the ZnO NPs diode-like device is due to adsorbed ionised oxygen molecules, where the number of electrons transferred is less than the number of hydrogen ions involved, so the sensitivity exceeds the Nernst limit.

5.1 Contact angle measurement of the ZnO NPs film after UVVH treatment.

In solution sensing, the more hydrophilic property can make the detection material more easily interact with the detection substance in the solution, thereby achieving better sensitivity. Since the 100/20nm mixed film is more hydrophobic, the pure 100nm ZnO film is more suitable for solution detection. In solution pH sensing, higher wettability enhances the film's ability to adsorb charges from the solution more effectively. When the contact angle is less than 90°, the material is generally considered to be hydrophilic and easily wetted. When the contact angle is greater than 90°, the material is generally considered to be hydrophobic and not easily wetted [147].

The contact angle measurement was shown in the following figures. **Figure 5.1** depicts the contact angle measurements for ZnO NPs across varying conditions. Specifically, **Figure 5.1** illustrates the contact angle of the as-deposited ZnO NPs film, and the contact angles for ZnO NPs films following UVVH treatment at 120 °C and 180 °C, respectively. Post-UVVH treatment, the contact angle increased, indicating a significant reduction in the surface energy of the ZnO NPs. This reduction is attributed to removing chemical functional groups, such as adsorbed oxygen molecules or hydroxyl groups, from the ZnO NPs surface during the UVVH process. A high wettability is vital for solution sensing, as it enhances the adsorption of target substances onto the ZnO NPs film, thereby inducing changes in electrical properties. Through the comparison between the 100 nm ZnO film and 100/20 nm mixture film, the 100 nm ZnO film shows higher wettability than the mixture film. This may be because the 100 nm ZnO film has more porous structure which allowed the water molecule to contact with the surface better. The ZnO NPs film without UVVH treatment showed a contact angle close to zero regardless of particle size. After UVVH treatment at 120 °C, the contact angle of the ZnO NPs mixed film was 49°, and the contact angle of the 100 nm ZnO NPs film was 25°. After UVVH treatment at 180 °C, the contact angle of the 100/20 nm film was 116°, and the contact angle of the 100 nm film was 94°.

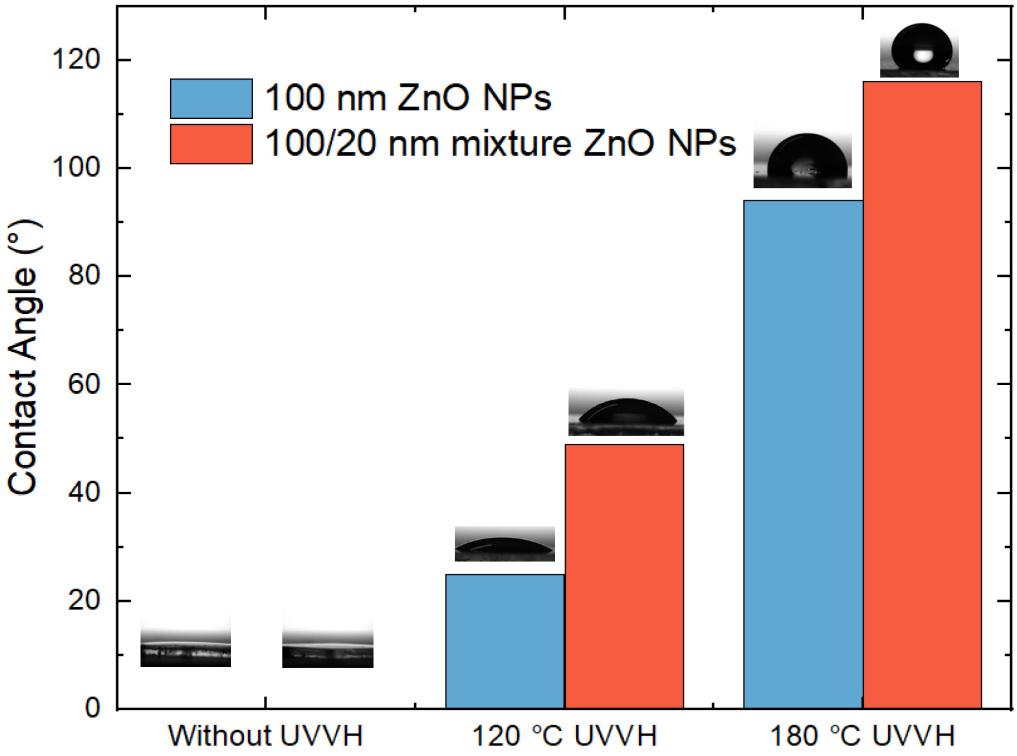

Figure 5.1: Contact angle results for 100nm and 100/20 nm ZnO NPs film with different UVVH temperature conditions. The contact angle was measured by KRÜSS DSA30.

5.2 Devise structure

Figure 5.2 shows the structure and the measurement setup of the device. During the UVVH process, ionised oxygen adsorbed onto the surface of ZnO NPs is removed, forming low-resistivity zinc oxide (LR ZnO). The subsequent application of EVOH passivation preserves this low resistivity level by hindering the re-adsorption of oxygen molecules from the ambient atmosphere. In contrast, regions lacking EVOH passivation undergo oxygen re-adsorption following UVVH treatment, forming the surface depletion layer and leading to high-resistivity zinc oxide (HR ZnO) development [41], [92], [148]. The operational area of the pH sensor is situated at the interface between the LR and HR ZnO NPs. Owing to the porous structure of the nanoparticle film, the pH solution can permeate through the film, allowing it to directly contact the edge of the LR ZnO region, functioning as a liquid electrode. This can be proved by similar IV results in measuring 400 µL water or PBS buffer resistance using the carbon electrode with and without the ZnO, TiOx, and SiO2 multilayer on its top (**Figure 5.3 and 5.4**), where liquid permeates through the NPs film and contacts the electrode. Upon immersion in a solution, ZnO NPs facilitate the re-adsorption of water molecules onto their surface, forming surface hydroxyl groups [94], [149]. The surface hydroxyl groups interact with ions present in the solution, leading to the generation of an electrical potential [150]. The underlying mechanism of surface charging involves the adsorption of protons or hydroxide ions by the hydroxyl functional groups on the oxide surface [34], [100]. Specific hydrogen ion binding sites on the ZnO surface will be protonated in an acidic environment, establishing a positive charge. In alkaline conditions, the adsorption of hydroxide ions occurred. It leads to the development of a negative charge. The point of zero charge (PZC), defined as the pH at which the net charge on the surface is minimised, is observed at approximately pH 9 [150]. This means, when the pH value of the solution is less than 9, the ZnO NPs surface predominantly exhibits a positive charge, whereas, at pH value exceeding 9, the surface is primarily characterised by negative charges.

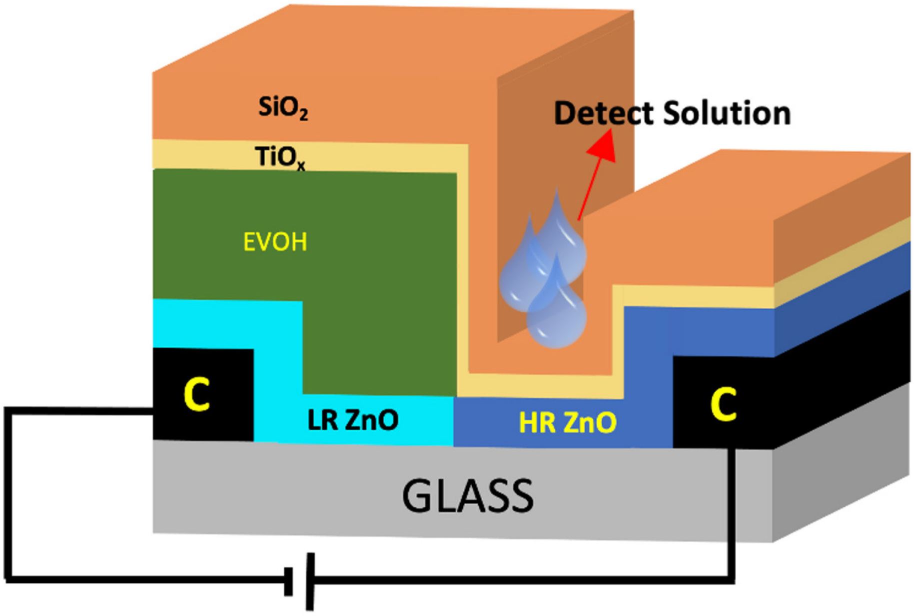

Figure 5.2: The structure of the diode-like ZnO NPs pH sensor. During the measurement the positive terminal of the source meter was connected the HR ZnO part and the negative was connected to the LR ZnO part.

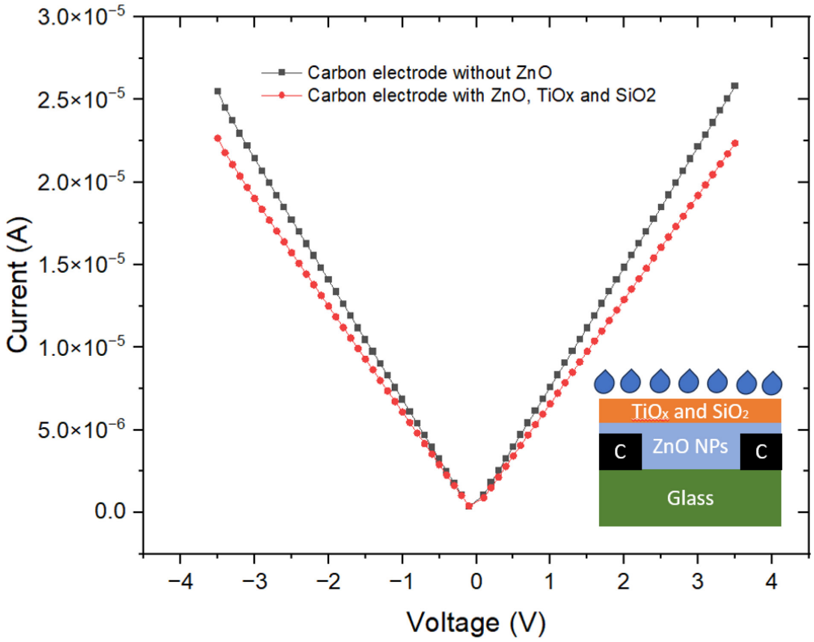

Figure 5.3: IV curve for the water used for pH solution using the carbon electrode (same as the pH sensor) with and without the ZnO NPs.

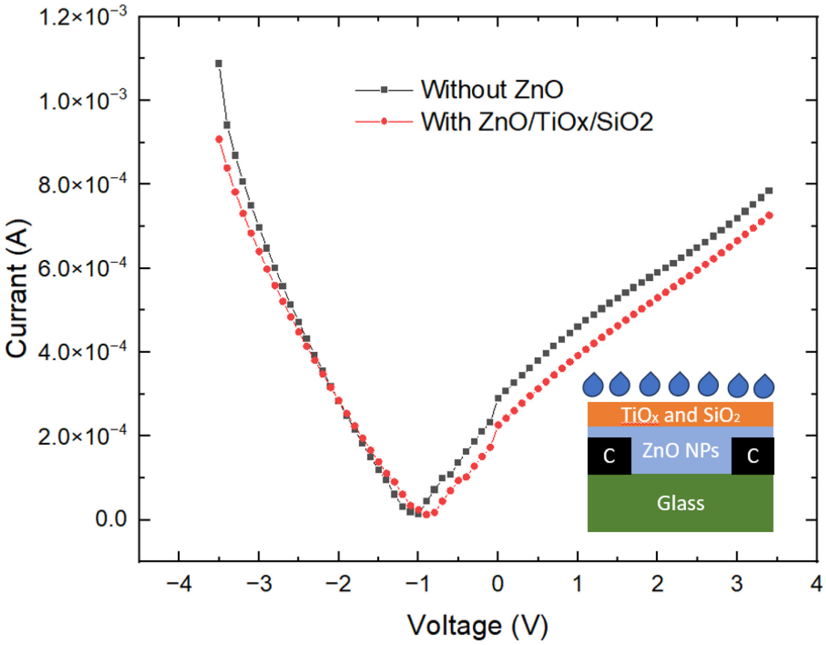

Figure 5.4: IV curve for the PBS buffer used for pH solution using the carbon with and without the ZnO NPs.

5.3 pH measurement results

The Film fabricated by 100 nm ZnO particles

All the IV measurements were taken in darkness. The current-voltage (IV) characteristics of the sensor were measured using a Keithley 2401 Source Meter Unit (SMU). Each reading was taken five minutes after applying the pH solution to the detection area. Following measurements and evaporation of the pH solution, the sensors were rinsed with deionised water in preparation for subsequent testing. Each measurement was followed by drying in vacuum. The error bar of the pH curve was obtained by repeating measurement-drying-measurement three times.

For the pH measurement, a 50 µL aliquot of the pH solution was applied to the detection region of the devices, and a 5-minute interval was allowed to ensure sufficient adsorption of ions by the ZnO NPs. **Figure 5.5** displays the linear-scale current-voltage (I-V) characteristics of the ZnO NPs pH sensor using 100 nm nanoparticles, with the corresponding logarithmic scale depicted in the **Figure 5.6**. The ZnO NPs devices exhibit diode-like I-V characteristics. The voltage sweep was conducted from -1.5 V to 3 V in 0.1 V increments. The ZnO NPs devices

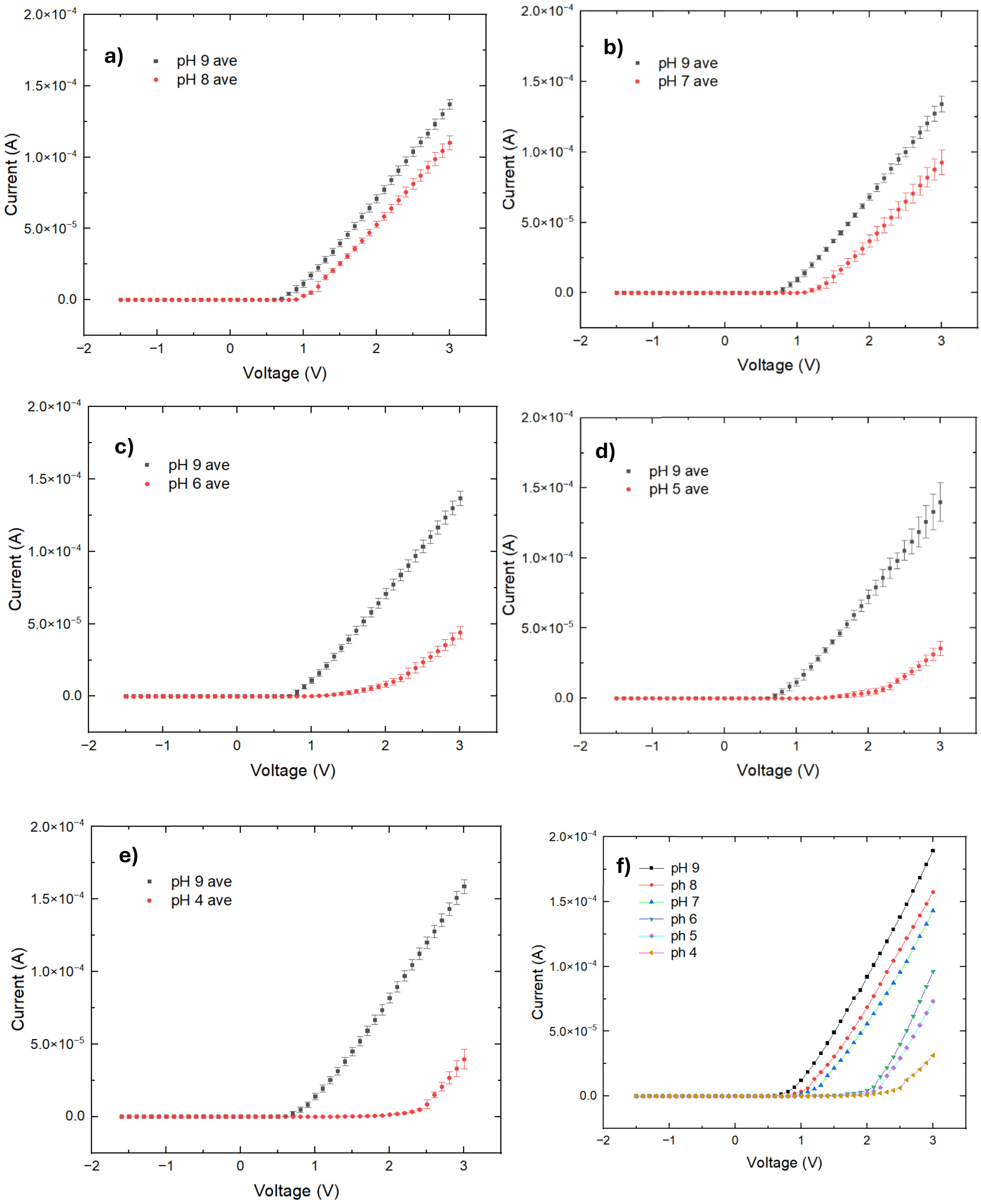

Figure 5.5: a) - e) Diode-like pH sensor behaviour for five devices. They all start with measuring pH 9 as the reference and then the target pH level. The threshold voltage increases as the pH level applied to the device decreases. **f)** One device measures different pH solutions.

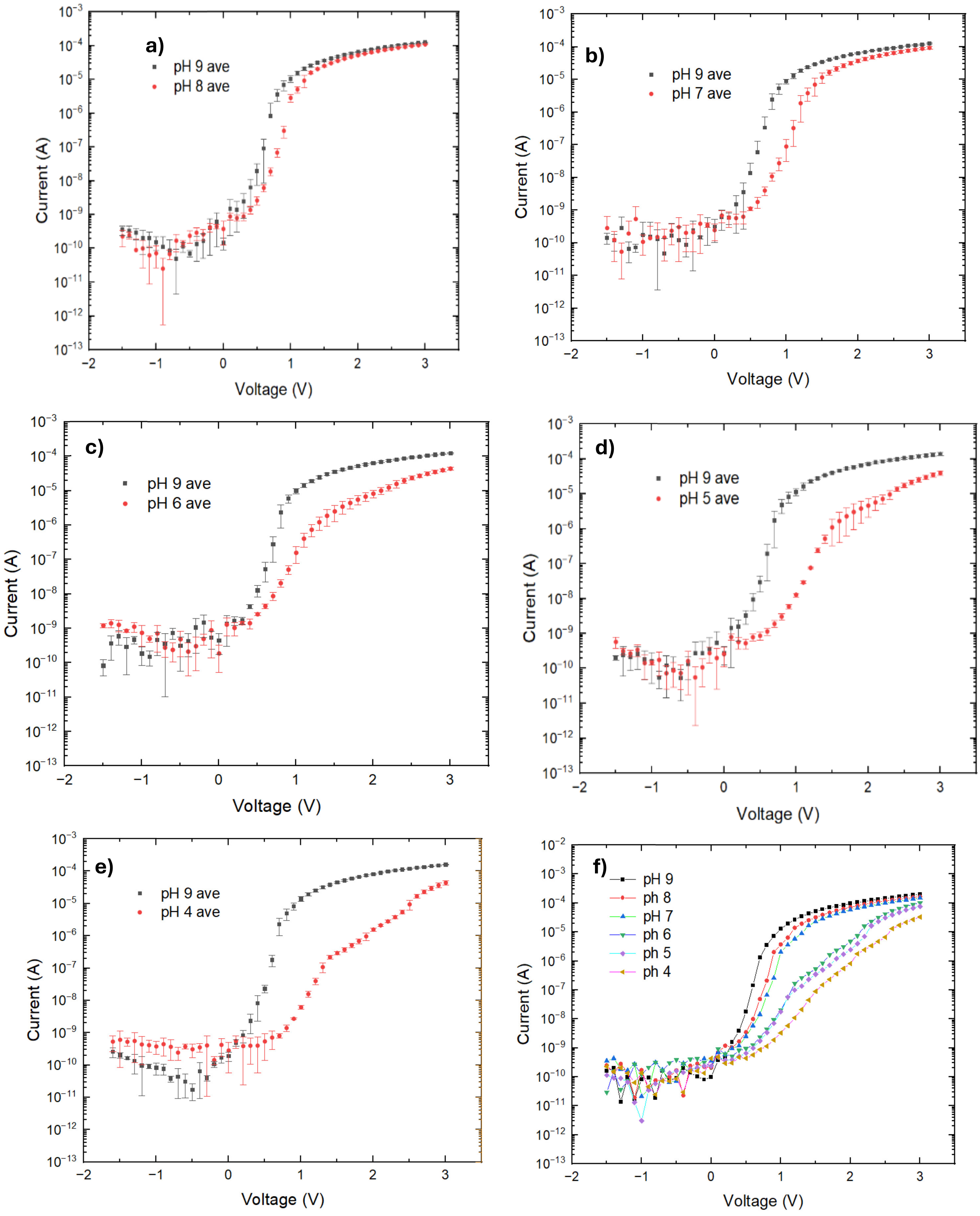

Figure 5.6: a) - f) Logarithmic scale IV curve for the ZnO NPs (100 nm) pH sensor.

show the diode-like IV characteristic. The voltage sweep was set from -1.5V to 3V with a 0.1V step.

Figures 5.5a–5.5e depict individual pH sensing measurements from five distinct devices. Each pH condition was measured thrice through titration and drying to obtain average values. According to Fortunato's study on WO3 nanoparticle pH sensors [31], where pH 9 was employed as the initial measurement point due to the minimal output voltage at this pH. Initial measurements of this work similarly utilised pH 9. This choice is attributed to the minimum surface potential observed in ZnO nanoparticles at approximately pH 9. For the pH 9 measurement, the diode-like devices exhibit an off-state current on the order of 10^{-9} A and a turn-on current of approximately 10^{-4} A, achieving an on/off ratio of 10^{5} at 2.5 V. The threshold voltage for detecting pH 9 is consistently 0.31 V across all devices, increasing progressively as the pH level decreases. **Figure 5.5f** illustrates pH detection using a single device across various solutions. The threshold voltage transitions from 0.47 V to 2.31 V as the pH decreases from 9 to 4, corroborating the pH measurement results across all devices. The current at 2.5V decreases from 1.1×10^{-4} A to 6×10^{-6} A.

The subthreshold slope is a critical parameter that characterizes the influence of gate voltage on the channel current of a field-effect transistor. Additionally, it serves as a measurement indicator for diode devices, elucidating the relationship between forward bias voltage and current [151]. The IV characteristic curves, presented on a logarithmic scale in **Figure 5.6**, illustrate the current variations of the ZnO NPs diode-like pH sensor within the subthreshold range. Notably, as the pH of the measured solution decreases, the subthreshold slope of the device correspondingly decreases. As summarised in **Figure 5.7**, for pH values ranging from 9 to 4, the observed subthreshold slope values are: 129 ± 5 mV/dec, 160 ± 13 mV/dec, 214 ± 8 mV/dec, 285 ± 15 mV/dec, 321 ± 21 mV/dec, and 375 ± 17 mV/dec. These findings suggest that, at lower pH levels, the effect of voltage on the device's channel current diminishes. The underlying mechanism will be elaborated upon in sections 5.4 and 5.5.

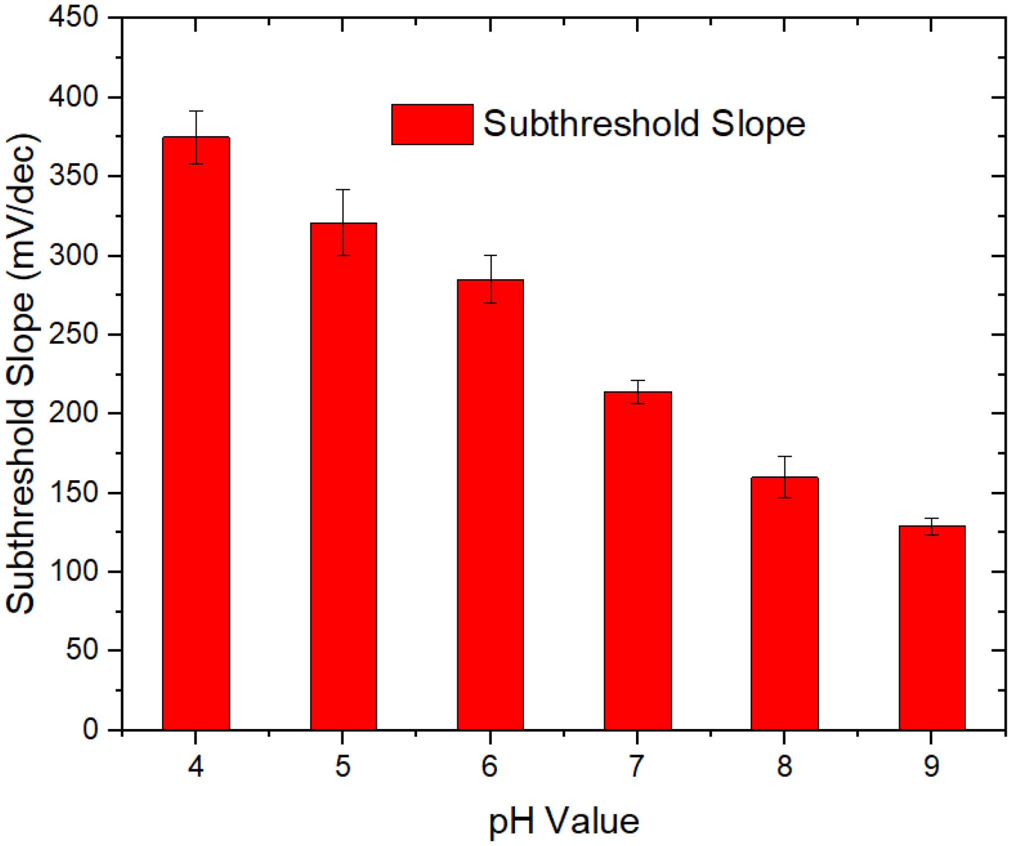

Figure 5.7: The subthreshold slope changes for ZnO NPs diode-like pH sensor.

The Film fabricated by mixed 100 nm and 20 nm ZnO particles

The measurement is the same with the 100 nm film. **Figure 5.8** displays the linear-scale current-voltage (I-V) characteristics of the ZnO NPs pH sensor using 100/20 nm nanoparticles, with the corresponding logarithmic scale depicted in the **Figure 5.9**. The measurement protocol is the same with the 100 nm device. For the pH 9 measurement, the diode-like devices exhibit an off-state current on the order of 10^{-8} A and a turn-on current of approximately 8 x 10^{-5} A, achieving an on/off ratio of 8 x 10^{3} at 2.5 V, which is smaller than the 100 nm ZnO NPs film. The average error bar of 100/20 nm film (> 20%) is also much larger than the 100 nm one (<5%). **Figure 5.8** shows the error range in the turn-on state, while **Figure 5.9** shows the error range in the subthreshold state. In the subthreshold region, the slope of the 100/20 nm film is

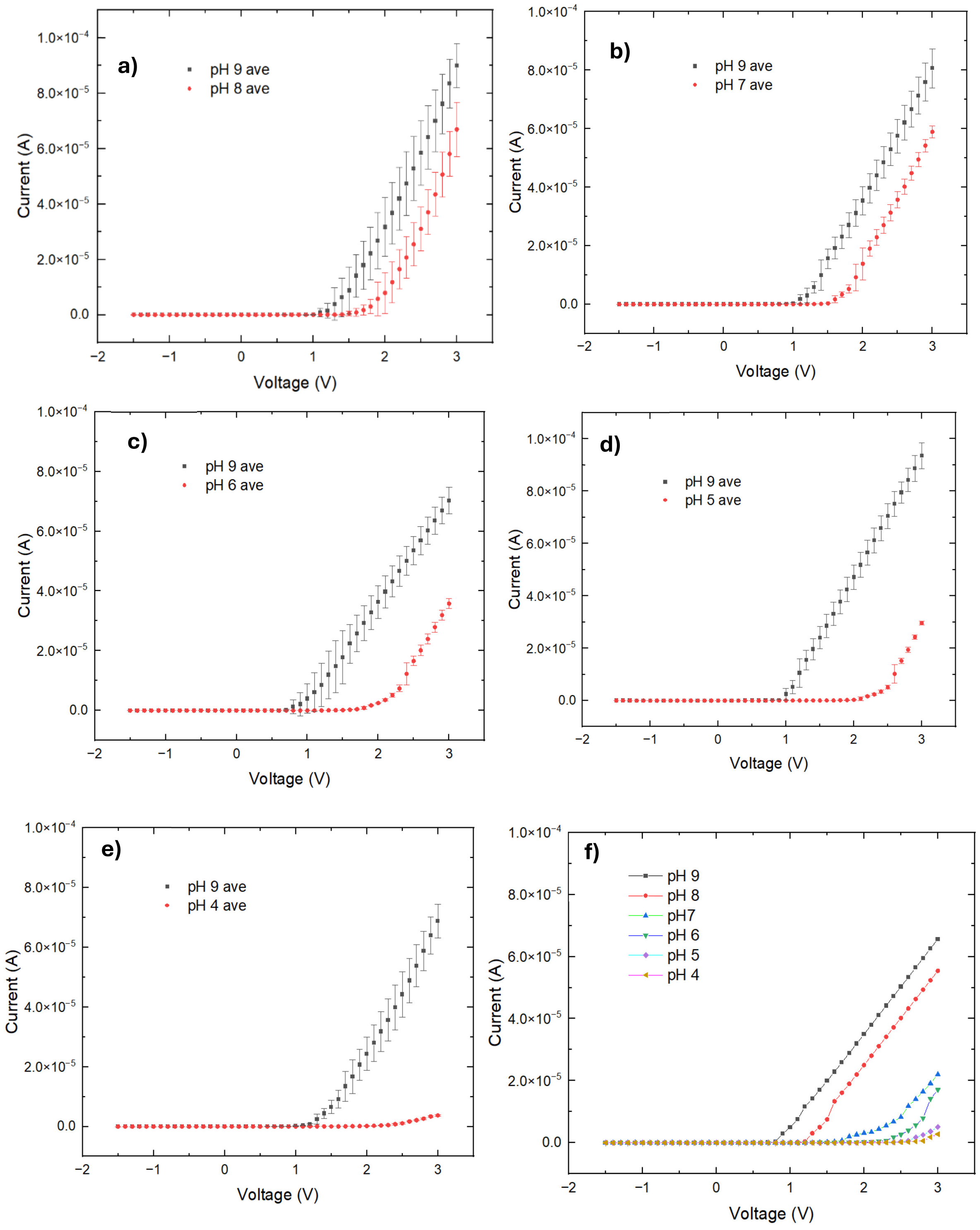

Figure 5.8: a)-f) IV response for the diode-like pH sensor using 100/20 nm ZnO NPs semiconductor film. The current error bar at the turn-on region is much larger than the 100 nm films.

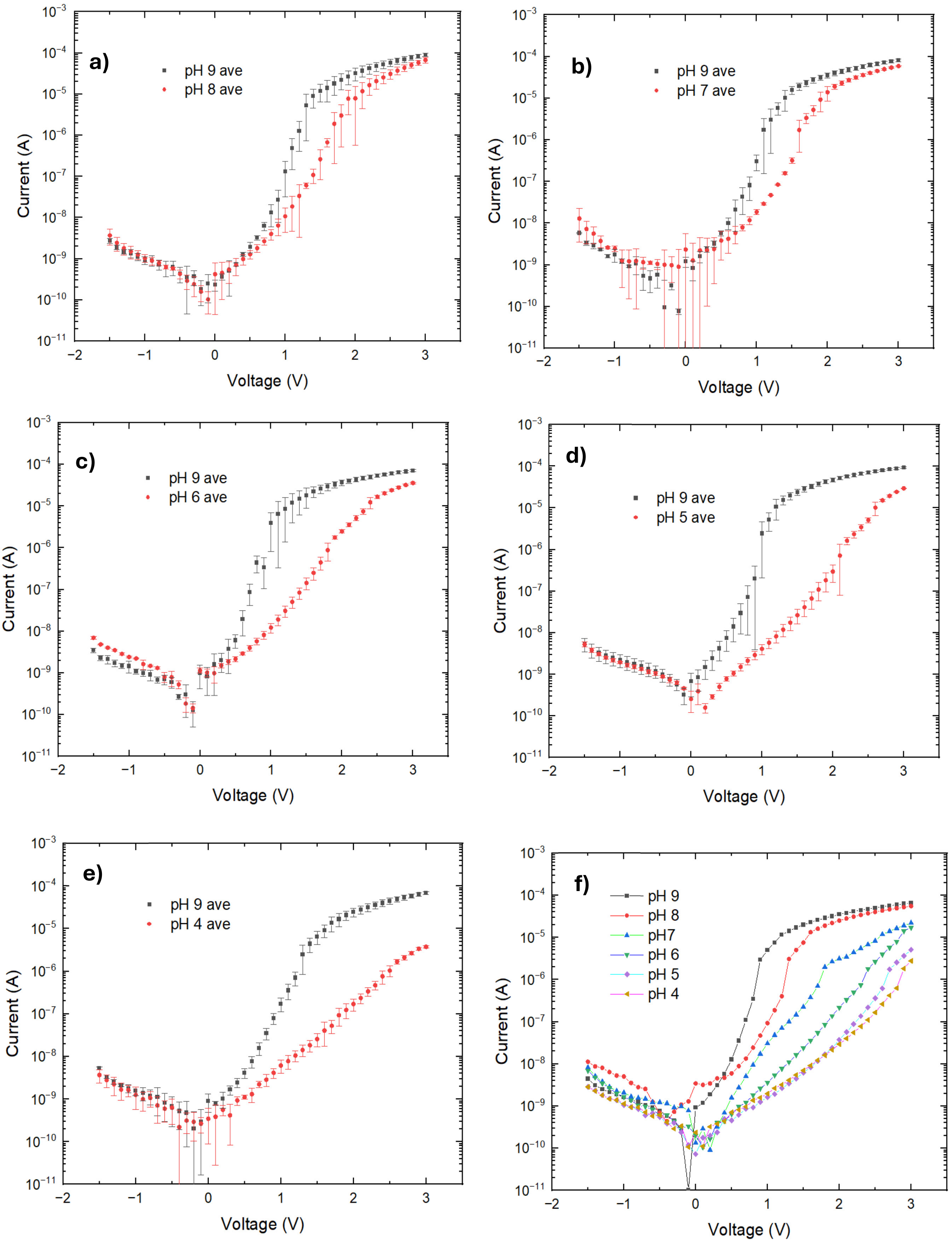

Figure 5.9: a)-f) Logarithmic scale IV curve for the ZnO NPs (100/20 nm mixture) pH sensor. The curve. The error bar at sub-threshold region is also much large than the 100 nm films.

smaller than that of the 100 nm film, which indicates that the 100/20 nm film is less sensitive to voltage than the 100 nm film.

These disadvantages may be due to the instability of its electrical properties during the measurement process. In a solution environment, the surface of ZnO NPs will adsorb ions in the solution and form surface charges. Driven by the electric field, these smaller nanoparticles are more likely to undergo electrophoresis, thereby affecting the contact between particles at the LR-HR interface and affecting its resistivity. The 100 nm ZnO NPs shows better electrical performance and stability than the 100+20 nm ZnO NPs film. So that, in the following section, the device are all based on 100 nm ZnO NPs films.

5.4 IV Characterization and Discussion of the LR-HR ZnO NPs interface

To demonstrate that the intrinsic properties of the diode-like ZnO NPs enable characterisation in both solid and liquid electrode environments, **Figure 5.10** presents the diode-like electrical characterisation of UVVH-treated ZnO NPs in a liquid-free electrode environment. The fabrication process is detailed in the previous chapter 3 (**Figure 3.12**). Following the deposition of ZnO NPs and EVOH with subsequent UVVH treatment, a carbon electrode solution was printed onto the high-resistance (HR) ZnO NPs (without EVOH) and dried at room temperature. Voltage was swept from -10 V to 10 V, yielding a turn-off current of 3.9×10^{-9} A at -10 V and a turn-on current of 3.5×10^{-4} A at 10 V, resulting in an on/off ratio of approximately 10^5. The threshold voltage was observed at 4.9 V. The diode-like behavior of LR-HR ZnO NPs is due to its inherent properties, not due to chemical reactions with water molecules or substances in the solution. Regardless of whether it is in a solution environment or not, the interface will show diode-like electrical characteristics.

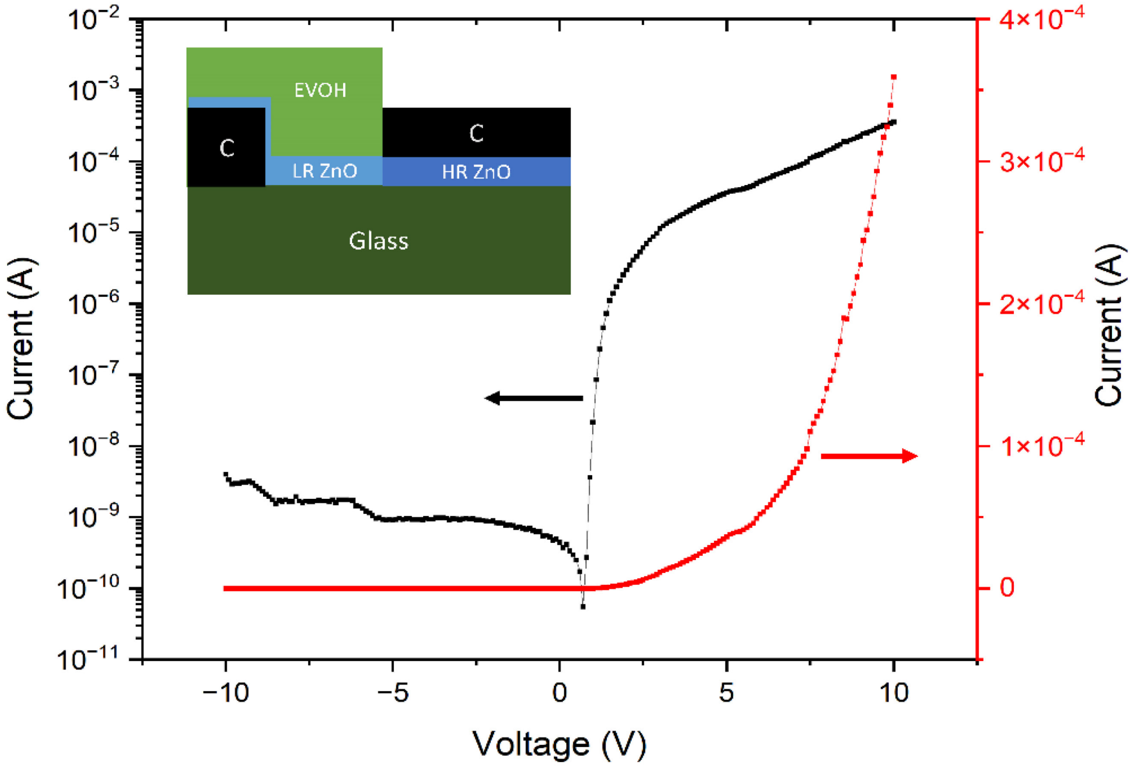

Figure 5.10: The intrinsic diode-like behaviour of the LR-HR ZnO NPs interface with a solid carbon electrode.

The pH sensing mechanism of ZnO can be attributed to the adsorption of the ions onto the ZnO NPs, forming charged functional groups on its surface. [34], [100], [152] When studying the effect of surface adsorption on the electrical properties of ZnO NPs, the oxygen molecules adsorbed on the surface of ZnO NPs are a factor that cannot be ignored because the amount of surface adsorption will significantly affect the resistivity of ZnO NPs.[25], [41], [153], [154] The following formula can express the relationship between the resistivity of ZnO NPs and the surface-adsorbed oxygen: [41], [93], [96].

$$O_2\ (g) + e^- \rightarrow O_2^-\ (ad) \qquad (5.1)$$

Where O_2 (g) represent oxygen molecules in the atmosphere, e^- represents the free electron in the ZnO NPs, and O_2^- (ad) represents the ionised surface adsorbed oxygen molecules.

Figure 5.11 illustrates the proposed mechanism of carrier transport underlying the diode-like behaviour and pH-sensing properties of ZnO NPs. **Figure 5.11a** depicts the state after UVVH treatment. ZnO NPs at the LR-HR interface re-adsorb oxygen molecules onto their surface.

These re-adsorbed oxygen molecules trap electrons and acquire negative charges, forming a low-conductivity surface depletion layer between the electrodes (pH solution) and the LR ZnO NPs film. Based on Greenham et. al,[61], [155], [156], applying varying offset voltages to both ends of ZnO NPs influences the adsorption and desorption dynamics of ionised oxygen molecules on their surface. This phenomenon is hypothesised to result from the migration of positively charged oxygen vacancies within the ZnO NPs under the applied bias voltage. This migration modulates the surface adsorption charges, consequently altering the resistance of the ZnO NPs.

As shown in **Figure 5.11b**, under a forward bias, the negatively charged adsorbed ionised oxygen molecules migrate away from the interface between the LR ZnO NPs and the electrode. This reduces the depletion layer at the interface between the LR ZnO NPs and the electrode, facilitating electron transfer from the LR ZnO to the electrode and turning the device on. **Figure 5.11c** shows that when a reverse bias is applied, the adsorbed ionised oxygen molecules migrate into the LR ZnO NPs, expanding the depletion layer at the interface between the LR ZnO NPs and the electrode. This enlarged depletion layer inhibits electron transfer, effectively turning the device off.

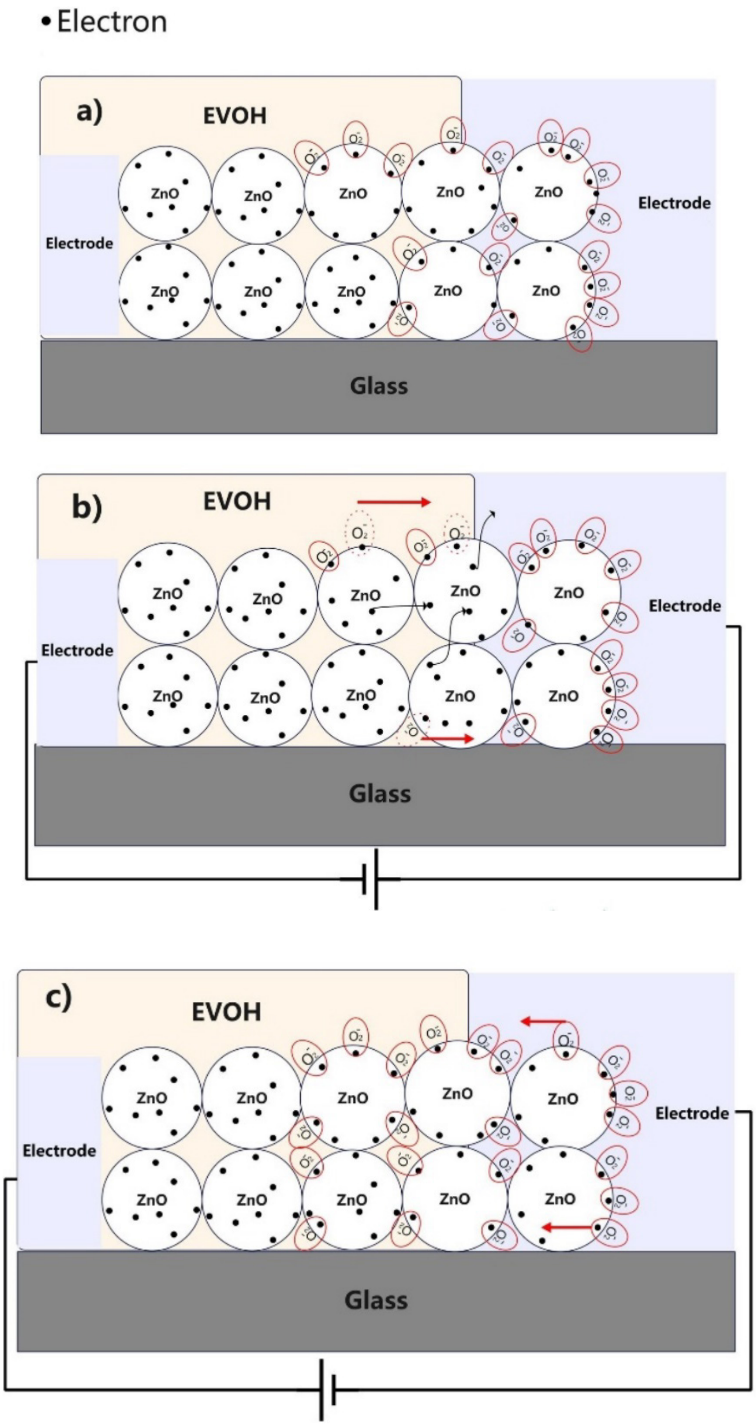

Figure 5.11: Carrier transport process for the ZnO NPs diode-like behaviour **a)** The carrier status without a bias voltage. After UVVH, the ZnO NPs at the LR-HR interface re-adsorb the oxygen molecules on its surface. The re-adsorbed oxygen molecules trap the electron and are negatively charged, forming a low conductivity surface depletion layer between the electrodes and the LR ZnO NPs film **b)** With forward bias applied, the negatively

charged adsorbed ionized oxygen molecules migrate to the positive side, out of the LR ZnO NPs, and the depletion layer between the LR ZnO NPs and the electrode is reduced. The electrons can freely transfer from the LR ZnO to the electrode, and the device is turned on. **c)** With the reverse bias applied, the adsorbed ionized oxygen molecules migrate into the LR ZnO NPs, increasing the depletion layer between the electrode and the LR ZnO NPs, and the device is turned off.

5.5 Titration curve

Figure 5.12 illustrates the titration curve of the device, showing a sensitivity of 360 ± 11 mV/pH unit for the threshold voltage shift. Besides, the threshold voltage of the intrinsic diode device is higher than that of the pH-sensing device. This discrepancy is attributed to the suboptimal contact between the second carbon electrode, printed on the HR region, and the low-resistance (LR) ZnO NPs compared to the liquid electrode. Consequently, adsorbed ionised oxygen molecules at the LR ZnO/electrode interface require more energy to migrate, increasing the threshold voltage.

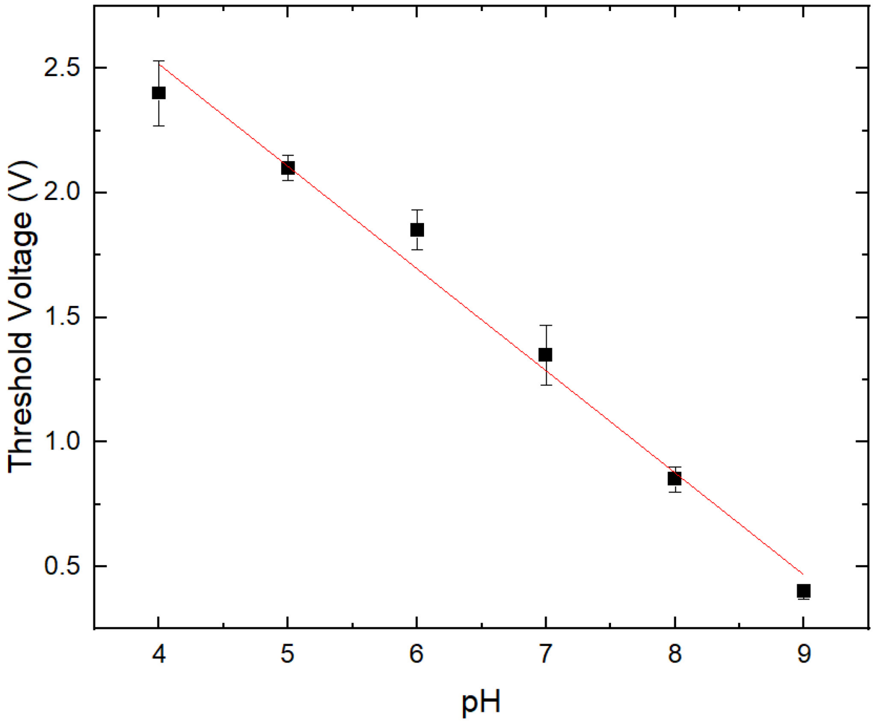

Figure 5.12: The titration curve shows the sensor's sensitivity is 360 ± 11 mV/pH.

5.6 Time depends on measurement and pH sensing mechanism

Figure 5.13 depicts the time-dependent current response of a ZnO NPs-based pH sensor under an applied forward bias voltage of 2.5 V. Measurements were recorded five minutes after introducing the pH solution to the sensor. The reason for choosing 2.5 V is that it exceeds the threshold voltage for all pH measurements based on previous measurements. Higher voltages may cause electrophoresis of ZnO NPs, making the measurement results inaccurate. After the voltage is applied, the device stabilizes in about 20 seconds and continues to measure for 40 seconds.

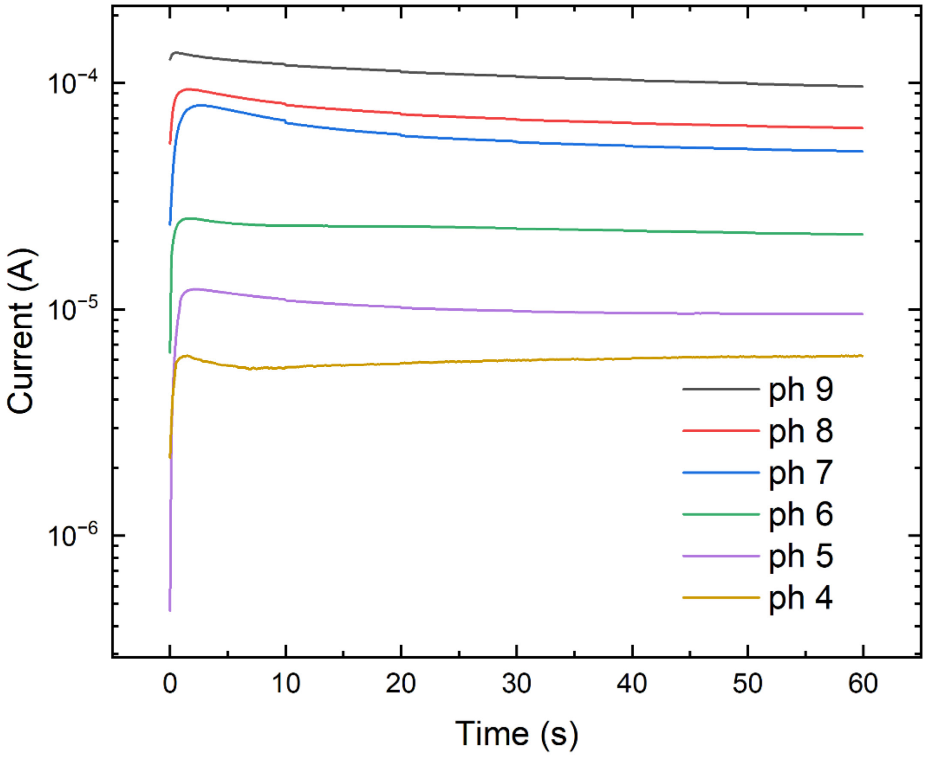

Figure 5.13: The time-dependent measurement for the ZnO NPs pH sensor shows a stable character. The voltage between the electrodes was set as 2.5V.

Figure 5.14 shows the equivalent circuit diagram of the ZnO NPs pH sensor. R_{LR} and R_S represent the resistance of low-resistance ZnO NPs and the solution, respectively. R represents the resistance of the high resistivity ZnO NPs. C and Cs represent the capacitance of the LR-HR interface and the solution. The diode represents the interface between the LR ZnO NPs and the HR ZnO NPs. From this figure, it can be inferred that the current flowing through the sensor under forward voltage bias can be written as:

$$I = V/(R_{LR} + R_S + R_{inter}) \tag{5.2}$$

R_{LR} and R_s are fixed values determined through prior measurements of the material's resistivity. R_{inter} is determined by the adsorbed ionised oxygen molecule, which can be affected by the voltage across the sensor and the pH value of the measured solution.

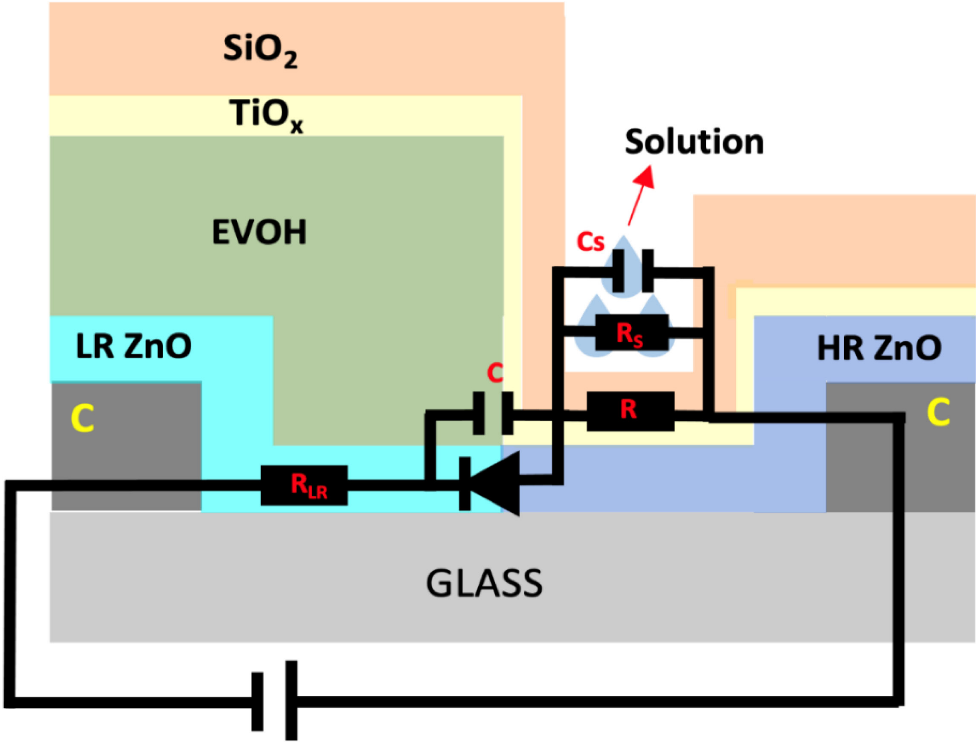

Figure 5.14: The schematic diagram of the ZnO NPs pH sensor structure and the equivalent circuit. R_{LR} and R_S represent the resistance of low-resistance ZnO NPs and the solution, respectively. R represents the resistance of the high resistivity ZnO NPs. The diode represents the interface between the LR ZnO NPs and the HR ZnO NPs.

Figure 5.15 presents the proposed pH-sensing mechanism. Upon adsorption of hydrogen ions from the pH solution, electrostatic interactions form between the positively charged hydrogen ions and the negatively charged adsorbed ionised oxygen molecules. During forward bias application, these interactions impose a higher energy barrier for migrating ionised oxygen molecules, increasing the device's threshold voltage. A higher hydrogen ion concentration (lower pH value) strengthens this electrostatic force, further elevating the threshold voltage and enhancing the resistivity of the interface.

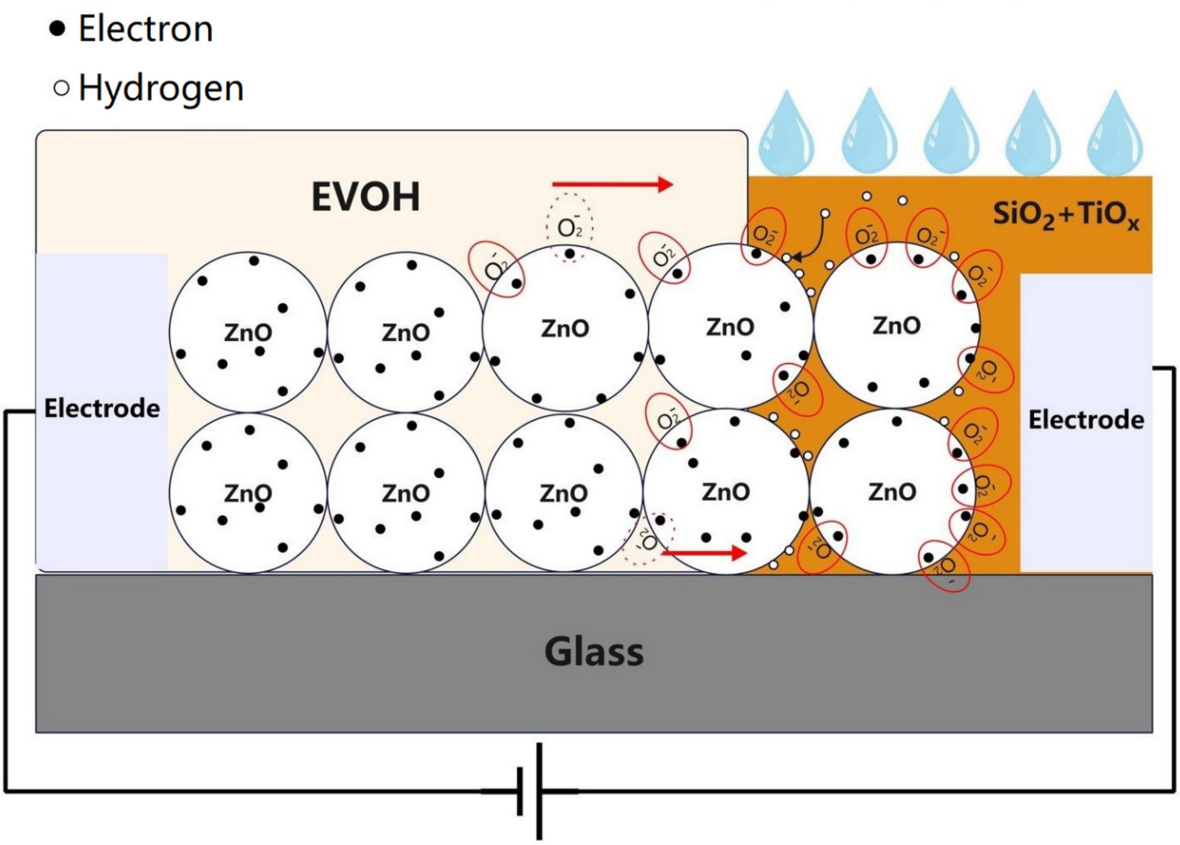

Figure 5.15: With the surface hydrogen ion adsorption, the positive hydrogen ions and adsorbed ionised oxygen molecules form electrostatic forces and attract each other. While applying the forward bias voltage, the ionised oxygen molecules require more energy to migrate, increasing the threshold voltage.

To elucidate the relationship between the hydrogen ion concentration in the solution and its adsorption on the ZnO NPs, the Freundlich adsorption isotherm was employed as a suitable model to describe multilayer adsorption on heterogeneous surfaces [157], The Freundlich isotherm is expressed as follows: [158]

$$\frac{X}{m} = K_f \times C_{eq}^{1/n} \tag{5.3}$$

Here, x is the adsorbed mass of the adsorbate, m represents the mass of the adsorbent, and C_{eq} represents the adsorbate equivalent concentration in the solution. K_f and n are the Freundlich parameters. The Freundlich isotherm describes the relationship between the adsorbate-to-adsorbent mass ratio and the equilibrium concentration of the adsorbate. Since the mass of ZnO NPs and the adsorbed hydrogen ions is negligible compared to the pH solution mass, the equilibrium concentration of hydrogen ions is effectively equivalent to the initial solution concentration. The mass of adsorbed hydrogen ions can thus be written as:

$$x_H = K_f \times C_{eq}^{1/n} \times m_{a-ZnO} \tag{5.4}$$

x_H is the mass of adsorbed hydrogen ions, and $m_{a\text{-}ZnO}$ is the mass of LR ZnO NPs at the interface. The PZC of ZnO NPs is approximately at pH 9; when the nanoparticles are exposed to a solution with a pH below this threshold, their surface charge becomes positively charged. In this context, hydrogen ions are capable of interacting with the surface of the metal oxide, leading to surface compensation effects. The dynamics of adsorption and desorption of ionized oxygen molecules on the ZnO NPs can be modulated by the electric field applied to the film [61], [155], [156]. The adsorption of hydrogen ions onto the surface of ZnO NPs induces the attraction of adsorbed ionised oxygen molecules, thereby increasing the energy required for their migration. It has been proposed that the density of the counter ions adsorption site is proportional to the density of the potential-determining ion on the metal oxide surface, with counter ions compensating for the potential-determining ions to form ion pairs [100]. Consequently, a higher degree of hydrogen ion adsorption leads to an increased amount of remaining adsorbed ionised oxygen molecules under a fixed forward voltage bias. It is hypothesised that the amount of adsorbed ionised oxygen molecules is proportional to the amount of adsorbed hydrogen ions under these conditions.

$$n_{ox} \propto \frac{x_H}{M_H} \times N_A \tag{5.5}$$

$$n_{ox} = \frac{a \times K_f \times C_{eq}^{1/n} \times N_A \times m_{a-ZnO}}{M_H} \tag{5.6}$$

n_{ox} represents the amount of the remaining adsorbed ionized oxygen molecules. M_H represents the molar mass of hydrogen ions. N_A represents the Avogadro constant. Parameter *a* serves as the fitting constant, balancing the adsorbed oxygen molecules and hydrogen ions. Given the electrostatic nature of the interaction between the hydrogen ions and adsorbed ionised oxygen molecules, the value of *a* is influenced by the forward bias voltage. Ideally, an increase in the forward bias breaks this interaction and reduces the value of a. While the presence of adsorbed ionised oxygen molecules is known to increase the resistivity of ZnO NPs films, the precise quantitative impact requires further investigation and validation. An interpretation suggests that adsorbed ionised oxygen molecules enhance carrier scattering within the material, consequently diminishing carrier mobility. Furthermore, carrier mobility is inversely proportional to the areal density of these adsorbed ionised oxygen molecules [159], [160]. When the carrier concentration is defined, the relationship between carrier mobility and the density of adsorbed ionised oxygen molecules can be articulated as follows [159]:

$$\frac{1}{\mu_{(N_{ox})}} = \frac{N_{ox}}{C_{(n)}} + \frac{1}{\mu_0} = \frac{n_{ox}}{A_{nps} \times C_{(n)}} + \frac{1}{\mu_0} \tag{5.7}$$

Here $\mu_{(N_{ox})}$ represents the carrier mobility of adsorbed ZnO NPs. N_{ox} is the areal density of the adsorbed ionised oxygen molecule, representing the carrier mobility at the interface. A_{nps} is the total surface area of the ZnO NPs. μ_0 corresponds to the pristine mobility of ZnO NPs without adsorption, the same as the LR ZnO NPs. The coefficient $C_{(n)}$ reflects the scattering characteristics resulting from adsorption, which is influenced by carrier concentration and adsorption properties. Given that the resistivity $\rho = 1/n_e\mu q$, where n_e is the carrier concentration and q is the elementary charge. Resistance $R = \rho L_{cross}/A_{cross}$, where L_{cross} and A_{cross} are the length and cross-sectional area of the ZnO NPs interface. So, the resistance of the ZnO NPs with adsorbed ionized oxygen molecules can be expressed as:

$$R_{inter} = \frac{L_{cross}}{A_{cross} \times A_{nps} \times n_e \times q \times C_{(n)} \times M_H} \times a \times K_f \times C_{eq}^{1/n} \times N_A \times m_{a-ZnO} + \frac{L_{cross}}{A_{cross} \times n_e \times q \times \mu_0} \tag{5.8}$$

From equation (5.8), the term $L_{cross}/(A_{cross} \times n_e \times \mu_0 \times q)$ can be interpreted as an extension R_{LR} in the LR-HR interface. Allowing it to be incorporated into R_{LR}. Extract the coefficient $L_{cross} /(A_{cross} \times A_{nps} \times n_e \times q \times C_{(n)} \times M_H)$, and a coefficient $b = L_{cross} /(A_{cross} \times A_{nps} \times n_e \times q \times C_{(n)} \times M_H)$ is defined. By substituting Equation (5.8) into Equation (5.1), the relationship between the forward bias current and the hydrogen ion concentration is established.

$$I = \frac{V}{R_{LR} + R_s + a \times \mathrm{b} \times K_f \times C_{eq}^{1/n} \times N_A \times m_{a-ZnO}} \tag{5.9}$$

According to the circuit shown in **Figure 5.14**. The sum of R_{LR} and R_s is set as 15 KΩ, calculated by the film resistance from the fully passivated film. The results are consistent with the value from the resistivity calculation. **Figure 5.16** correlates the current at the 60th second with proton concentration, providing further insight into the influence of surface hydrogen ion adsorption on the electrical properties of ZnO NPs-based devices. The fitted curve is generated by equation 5.9 under 2.5 V forward bias. The coefficient of determination (r^2) of the fitting curve is 0.98, which proves that the correlation between the fitting curve and the actual data is very high. It is worth mentioning that the fitting curve only considers the effect of ion adsorption on the electrical properties of ZnO NPs and does not consider the impact of ions generated by chemical reactions on the overall current. It is not applicable in strong acid and base environments. The fitting function may not be suitable for high bias voltage. The higher voltage can cause the electrolysis of water, which can lead to the device being unstable.

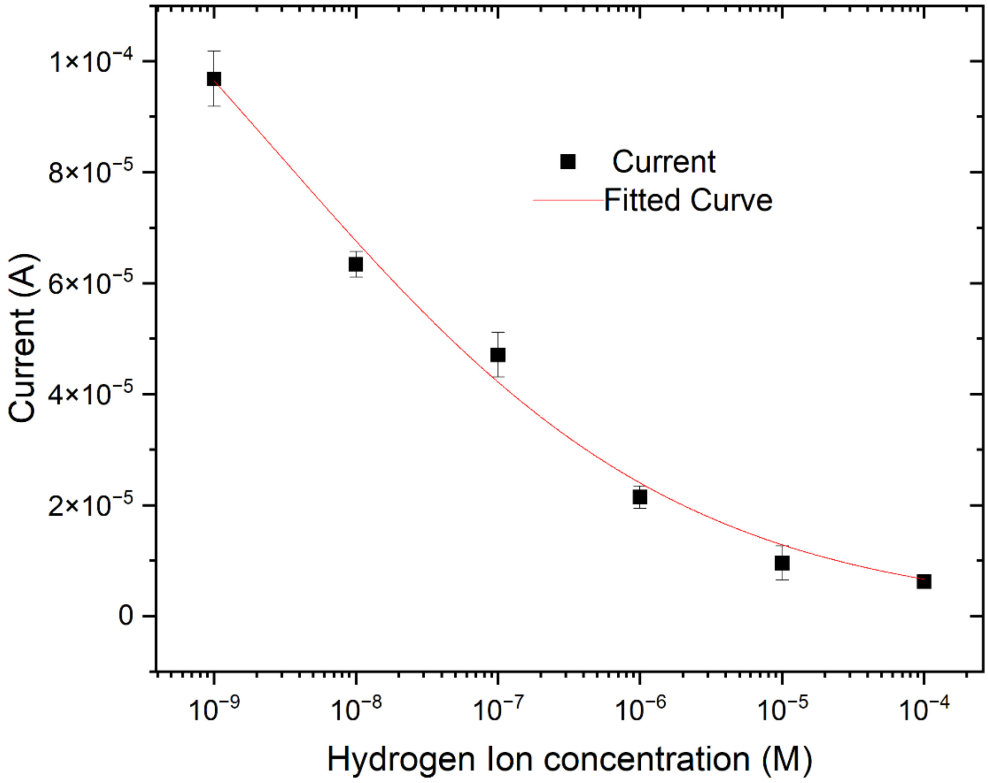

Figure 5.16: The current value from a for each pH measurement at 60th second, and the fitted curve is obtained from the derived equation 5.9.

The fitting coefficient results: n = 3.24 ± 0.16; $a \times \mathrm{b} \times K_f \times N_A \times m_{a-ZnO} = 7.04 \times 10^6 \pm 2\times10^5$, with the hydrogen ion concentration as mg/L. Because the thickness of the film measured by SEM is between 1.8 to 2.2 μm and the particle diameter is assumed as 100 nm. Some of the fitting parameters can be estimated. The mass of total ZnO NPs providing adsorption sites is estimated to be between 2×10^{-8} to 6×10^{-8} g, which is calculated from the volume and the density, and the surface area is estimated to be 3×10^{-7} to 7×10^{-7} m^2. From the datasheet of ZnO NPs (see **Appendix B**), the surface area shows a value of 10 to 25 m^2/g, which is consistent with the calculation (12 to 35 m^2/g). The carrier concentration is estimated to be 2×10^{17} to 8×10^{17} cm^{-3}, and the coefficient $C_{(n)}$ reflecting the scattering characteristics can be estimated between 10^{13} to 10^{14} $V^{-1}s^{-1}$. From these estimations, $a \times K_f$ can be calculated between 0.5 to 23.

5.7 Simulation circuit

Figure 5.17 illustrates the simulation circuit derived from the equivalent circuit depicted in **Figure 5.14** for the UVVH-treated ZnO NPs pH sensor. The circuit was simulated using Multisim software. The term RTiO_SiO2 denotes the resistances of high-resistivity (HR) ZnO NPs, while ZnO_interface refers to the interface between low-resistivity (LR) ZnO and HR ZnO. The ideality factor was varied from 1 to 6, resulting in a distinct shift in the threshold voltage. The ideality factor, or emission coefficient, is a parameter within the diode mathematical model, where an ideality factor of 1 signifies an ideal diode. A higher ideality factor is typically associated with carrier recombination in diodes, characterising the process by which conductive electrons lose energy.[161] In the context of the ZnO NPs pH sensing mechanism, an increased concentration of hydrogen ions leads to a greater number of ionised oxygen molecules and enhanced electron scattering, decreasing the kinetic energy of the electrons during drifting. **Figure 5.18** presents the simulation results, demonstrating that the IV characteristics are closer to the lower pH detection with a higher ideality factor.

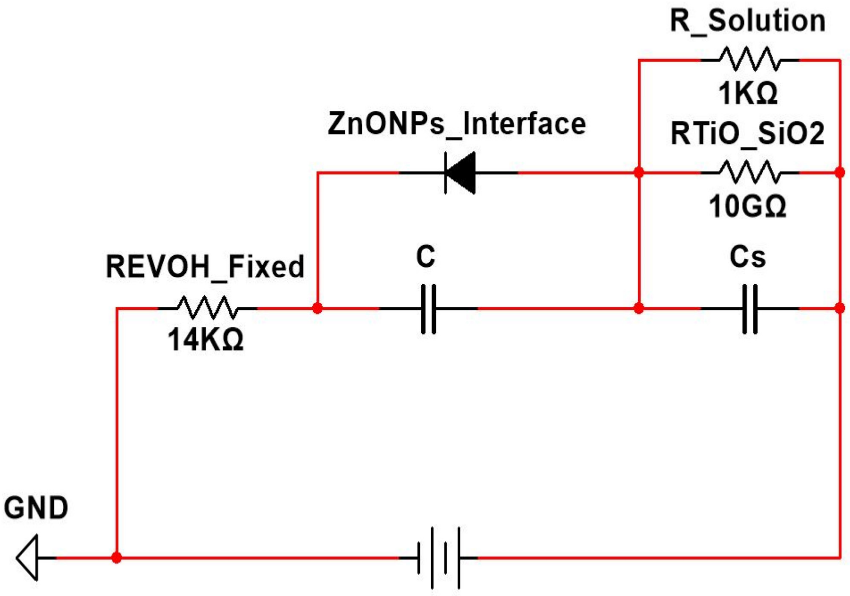

Figure 5.17: Simulation circuit for diode-like ZnO NPs pH sensor.

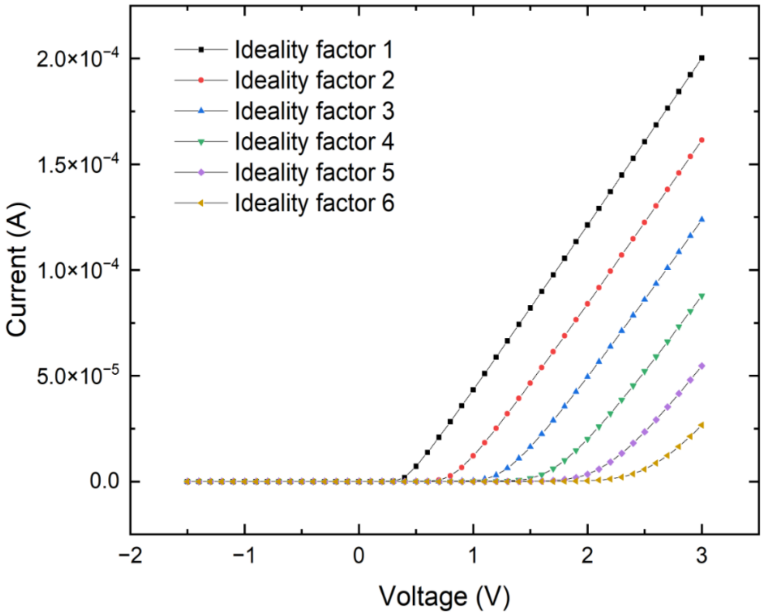

Figure 5.18: The IV character of the simulation circuit with varying forward emission coefficients. The IV range of the ideality factor from 1 to 6 is consistent with sensor IV response with the pH range of the test solution from pH 9 to pH 4.

Shambel et al. proposed that as the diode's internal resistance decreases, the diode's ideality factor increases [162]. This is consistent with what is mentioned in this chapter. As hydrogen ions and adsorption occur, the internal resistance of the ZnO Diode-like pH sensor increases, which changes its IV curve and increases the ideality factor. As can be seen from **Figure 5.18**, when the ideality factor is 1, its IV characteristic curve is similar to that of the solution detecting pH 9. When the ideality factor is 6, its characteristic curve is identical to that of pH 4.

5.8 Repeatable use for the ZnO NPs diode-like pH sensor

Figure 5.19 illustrates the second pH measurement of the ZnO NPs sensor, spanning a range from pH 9 to pH 4. Following the initial measurement from pH 9 to pH 4, the device underwent re-treatment via the UVVH process for 2 hours. The current level at 3 V exhibited similarity to the initial usage. However, in comparison to the first measurement, although the threshold voltage reverted, it remains elevated relative to the initial usage.

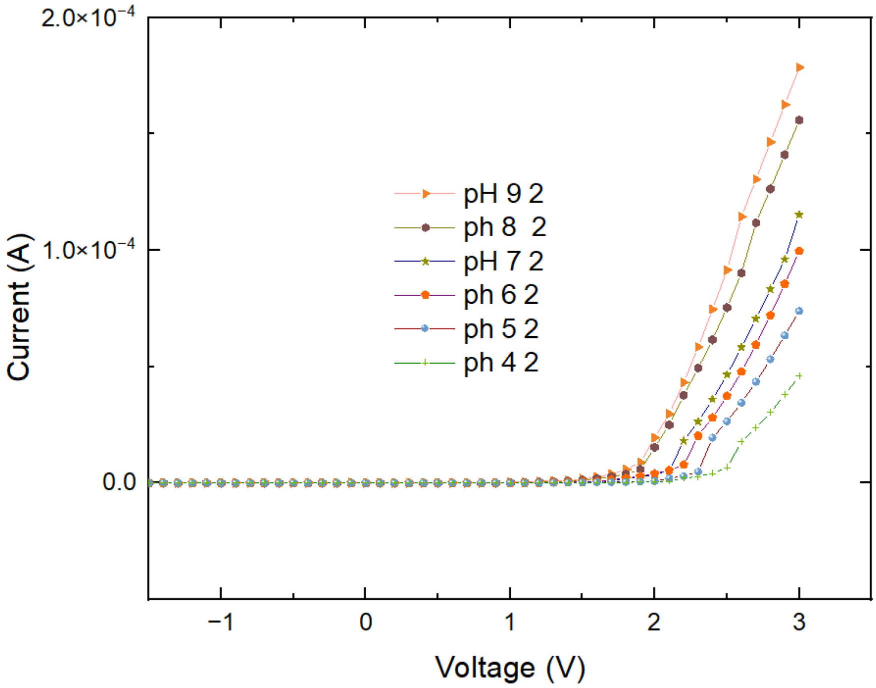

Figure 5.19: Repeatable use for the ZnO NPs diode-like pH sensor testing. After the first time measurement from pH 9 to pH 4, the device was retreated by the UVVH process. Although the threshold voltage shifts back, it's still more significant than the first-time detection.

This anomaly may be attributed to the migration of ZnO NPs as a consequence of the electrophoresis phenomenon. The increased interparticle distance likely resulted in a greater adsorption of oxygen molecules onto the particle surfaces. Additionally, in an acidic environment, ZnO is known to undergo specific chemical reactions that may enhance the availability of adsorption sites on its surface. Despite not achieving complete recovery, the device demonstrates potential for sustainable application, and strategies for enhancing its reusability will be a focus of future research.

5.9 Memory effect of the diode-like ZnO NPs

The intrinsic diode-like ZnO NPs also show memory effect. The result is shown in **Figure 5.20**. The electrode on the HR-ZnO part is changed to a commercial silver nanowire for better connection to the LR-HR interface. The scan was from -10 V to 10 V and then backwards. The device shows both diode behaviour and memory effect. The memory effect still requires further investigation. One possible explanation is that when a high forward voltage bias is applied to the device, the adsorbed ionised oxygen molecules will accumulate in the HR-ZnO NPs part. The resistance at the interface will remain small until the reverse bias is applied, which will cause the adsorbed ionised oxygen molecule to move back to the LR-ZnO part, leading to high resistance at the interface. This behaviour shows a very low rest current and may apply to the memristor in the future.

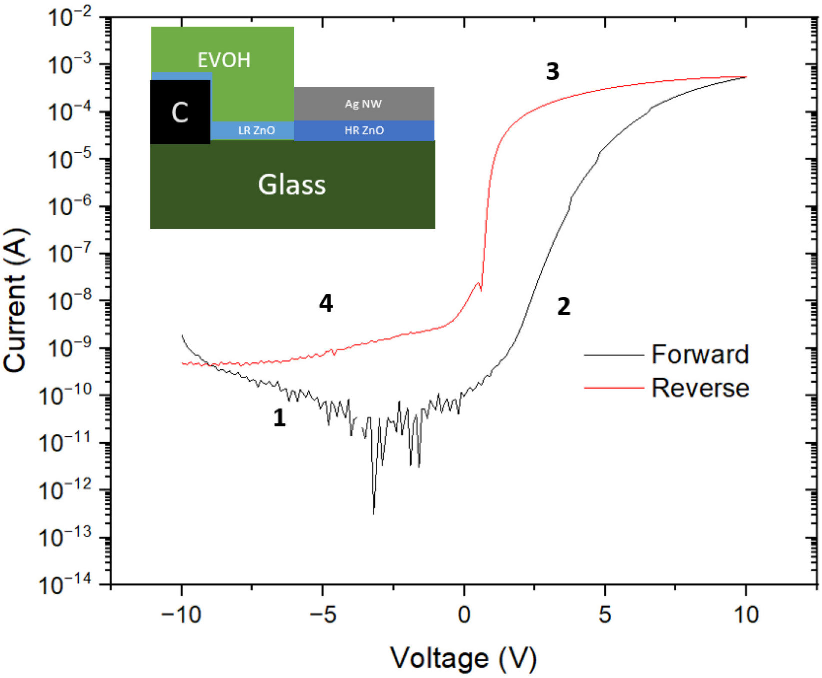

Figure 5.20: Memory effect of diode-like ZnO NPs device.

5.10 Conclusions of Chapter 5

This chapter presents a novel pH sensor utilising UVVH-treated solution-processed ZnO NPs, exhibiting a sensitivity of 360 ± 11 mV/pH. The sensor demonstrates diode-like behaviour, with an on-off ratio of 10^5. A plausible working principle for the sensor is proposed, indicating that the device's threshold voltage increases from 0.47 V to 2.31 V as the pH of the solution decreases from 9 to 4. The current formula derived from the adsorption isotherms aligns well with the experimental data. The observed diode characteristics are attributed to the migration of ionised oxygen molecules adsorbed on the surface of ZnO NPs. The subsequent adsorption of hydrogen ions inhibits this migration, with the reduction directly proportional to the concentration of hydrogen ions in the solution. The simulation results of the circuit diagram closely correlate with the actual measurement outcomes, further validating the proposed principle. Given its high pH sensitivity, this device demonstrates significant potential for applications such as cancer cell detection. Additionally, the solution-based manufacturing process, coupled with a maximum processing temperature of 120°C, indicates potential application in flexible electronic sensors.

Chapter 6

Conclusions and Future Work

This thesis demonstrated a novel fabrication method that enhances the electrical properties of solution-processed ZnO nanoparticle film by using exposure to 365 nm UV light in a vacuum. The resistance of the solution-processed ZnO film has been decreased by a factor of 10^6, which is comparable to ALD-deposited ZnO films. This enhancement can be stable in the long term with the application of a solution-processed EVOH passivation layer of 80 µm thickness. The fabricated ZnO film has a sheet resistance of 2.5×10^4 Ω/□ and a thickness of 2.35 µm. The EVOH passivation layer enhanced film stability, protecting it when exposed to the ambient environment. The resistivity of the ZnO NPs layer with EVOH passivation remains unchanged after 60 days in the ambient environment. The fabrication method proposed in this paper can initially minimise the influence of oxygen on ZnO NP and radically slow down any subsequent effect. Through the comparison of the different passivation materials, it can be concluded that it is beneficial for any passivating polymer to have hydroxyl functional groups to adsorb the ZnO surface and the passivation layer must be of suitable thickness to be effective. The oxygen transmission rate through the passivation layer could be further improved in the future by the addition of inorganic material which have lower oxygen transmission rates. The inclusion of glass flakes or nanoparticles, for example, would make the path the oxygen molecules travel much longer. The addition of such materials will, however, alter the mechanical properties of the passivating film. Solution processing is inexpensive, and the materials used are environmentally sustainable.

By using the UVVH process, a highly sensitive ZnO NPs semiconductor pH sensor fabricated using a fully solution-based process that eliminates the need for a high-temperature process.

The sensor demonstrates diode-like electrical characteristics, with its threshold voltage increasing as the pH of the measured solution decreases, yielding a sensitivity of 360 ± 11 mV/pH. The maximum processing temperature is 120°C, and the manufacturing procedure employs a UVVH technique. To ensure the electrical properties of ZnO NPs, a waterproof and oxygen-isolating polymer, EVOH was used to passivate ZnO NPs. From the comparison, the pure 100 nm ZnO NPs film works more stably than the 100/20 nm mixed film. This may be due to the smaller-sized NPs being easily influenced by the electrophoresis effect. The working principle of the sensor, as well as its diode-like characteristics, are closely associated with the adsorption of ionised oxygen molecules on the surface of the ZnO NPs. Finally, the mathematical model derived from the adsorption isotherm effectively correlates with the experimental data. The deposition method mentioned in this study and the maximum annealing temperature of 200 °C can adapt to most flexible substrates. The fully solution-based manufacturing approach shows promising potential for applications in medical sensing and flexible wearable electronics for ion-based detection applications.

Future work

UVVH-treated ZnO nanoparticles (NPs) exhibit distinctive electrical characteristics. By manipulating the number of oxygen molecules adsorbed onto their surfaces, the resistivity of these NPs can be effectively controlled. Future research directions can be summarized as follows:

1. To address the challenge of recycling ZnO NPs in pH sensors, the impact of electrophoresis on the nanoparticles can be mitigated by applying another passivation film, for example, spin-on glass, with moderate permeability at the LR-HR interface, thereby protecting the ZnO NPs. This can reduce the electrophoresis on the NPs, which makes the device more stable and reusable.

2. Given that cancer cells demonstrate increased acidity compared to normal cells, this presents opportunities for advancements in the field of cancer cell diagnostics. Because the pH diode-like sensor has the best sensitivity between pH 7 to pH 6, it has a potential application in cancer cell detection.

3. The adsorption of oxygen on the surface of ZnO NPs can be regulated by employing various materials with differing oxygen permeabilities, thereby controlling their electrical properties. This concept is primarily focused on the memristor characteristics exhibited by diode-like ZnO NPs, enabling data storage and calculations through precise control of the number of adsorbed molecules.

4. Smaller devices typically offer faster processing speeds, and significant integration can be accomplished by utilizing printing techniques for the fabrication of these miniaturized devices. In the domain of flexible wearable integrated circuits, the nonlinear characteristics resulting from the interaction of LR-HR ZnO NPs demonstrate significant potential for applications in logic circuits.

Appendix A Printed ZnO NPs film and Effect of Ti(acac)$_2$

To facilitate the display of the effect of this Ti precursor on the zinc oxide film, the film was made by a dispensing printer. As shown in **Figure A1.1**, The surface cracks of the film formed in the ZnO solvent mixed with Ti(acac) were much smaller than that of the unincorporated part. Both films were made in the same way and dried at the same temperature. Printing traces can be clearly seen in the film without adding surfactant. Films with added surfactant exhibited particle trajectories during drying. It is certain that even a very small amount of Ti(acac) can have a large effect on the geometry of the ZnO film and can make the ZnO film more uniform. However, the specific mechanism of action is still unclear.

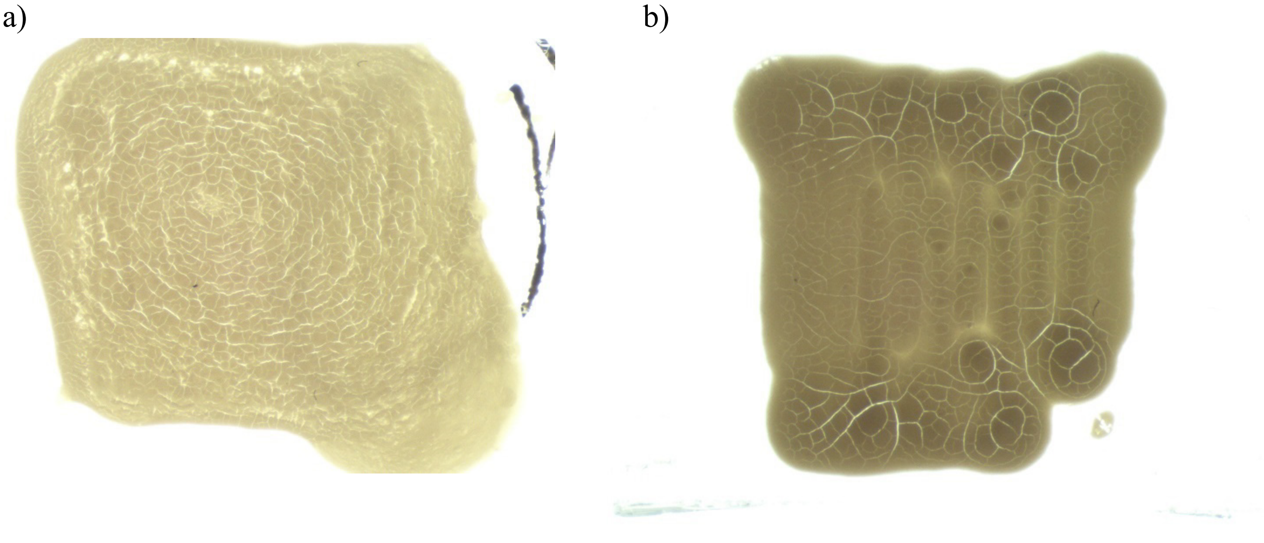

Figure. A1.1: Dispenser printed ZnO NPs film dry in the air using dispensing printer a) with and b)without Ti(acac)

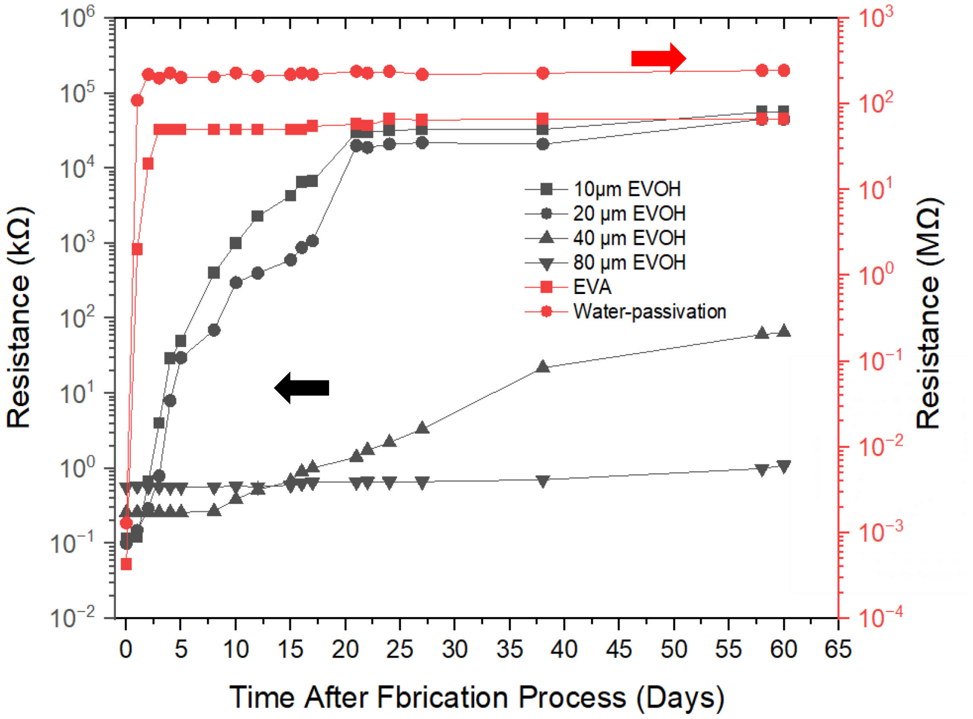

Figure A1.2: Measured time-dependent resistance change of interdigitated devices with different passivation processes. The interdigitated device width is 90 mm, and the length is 0.85 mm. The thickness of the EVOH passivation is from 10 µm to 80 µm. The thickness of EVA film is 800 µm.

Appendix B [Datasheet of ZnO NPs]

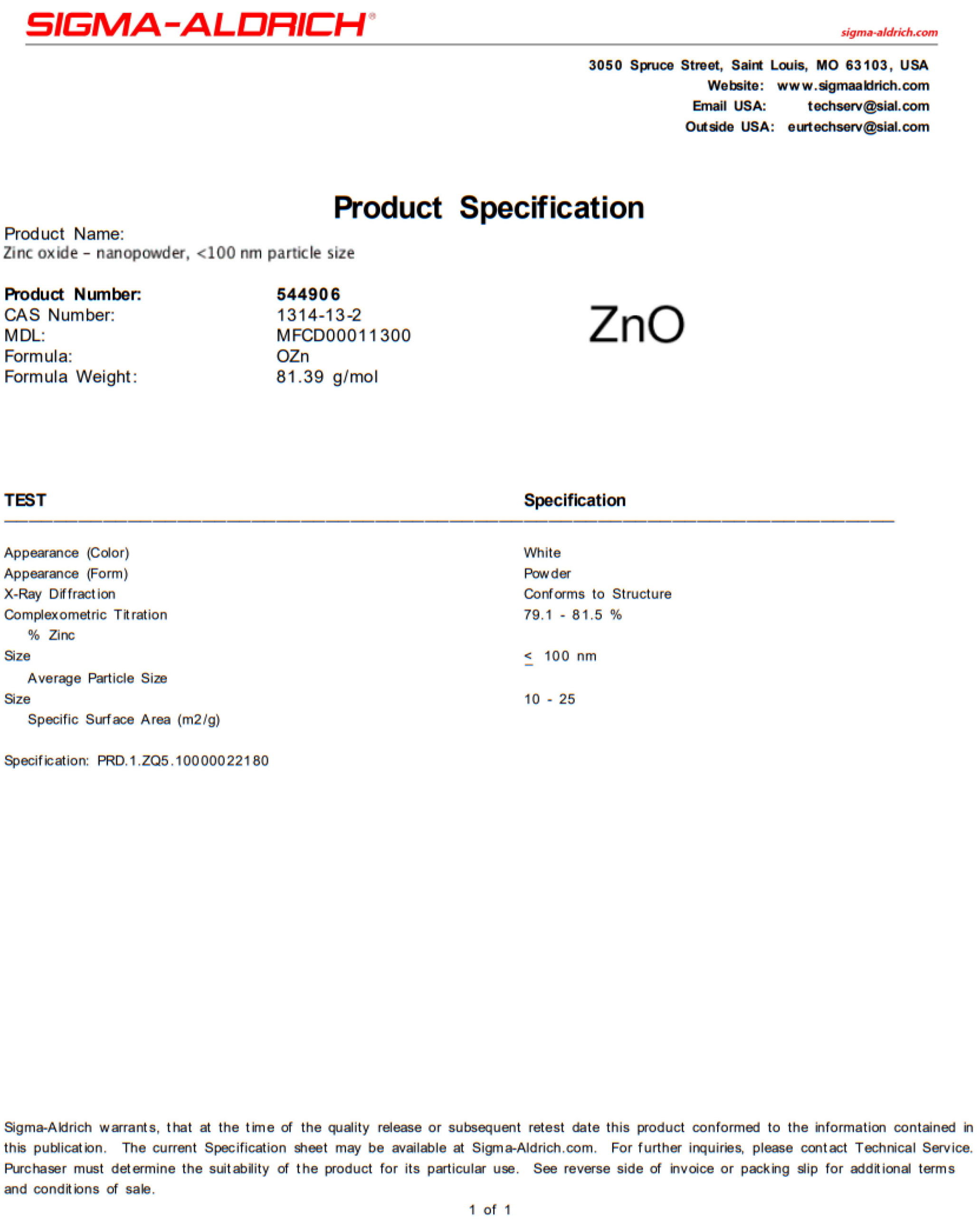

SIGMA-ALDRICH

sigma-aldrich.com

3050 Spruce Street, Saint Louis, MO 63103, USA
Website: www.sigmaaldrich.com
Email USA: techserv@sial.com
Outside USA: eurtechserv@sial.com

Product Specification

Product Name:
Zinc oxide – nanopowder, <100 nm particle size

Product Number: **544906**
CAS Number: 1314-13-2
MDL: MFCD00011300
Formula: OZn
Formula Weight: 81.39 g/mol

ZnO

TEST	Specification
Appearance (Color)	White
Appearance (Form)	Powder
X-Ray Diffraction	Conforms to Structure
Complexometric Titration % Zinc	79.1 - 81.5 %
Size Average Particle Size	≤ 100 nm
Size Specific Surface Area (m2/g)	10 - 25

Specification: PRD.1.ZQ5.10000022180

List of References

[1] S. Tong, J. Sun, and J. Yang, 'Printed Thin-Film Transistors: Research from China', *ACS Appl. Mater. Interfaces*, vol. 10, no. 31, pp. 25902–25924, Aug. 2018, doi: 10.1021/acsami.7b16413.

[2] Y. Pang *et al.*, 'Flexible transparent tribotronic transistor for active modulation of conventional electronics', *Nano Energy*, vol. 31, pp. 533–540, Jan. 2017, doi: 10.1016/j.nanoen.2016.11.042.

[3] T. Takahashi *et al.*, 'Carbon Nanotube Active-Matrix Backplanes for Mechanically Flexible Visible Light and X-ray Imagers', *Nano Lett.*, vol. 13, no. 11, pp. 5425–5430, Nov. 2013, doi: 10.1021/nl403001r.

[4] N. Luo, J. Ding, N. Zhao, B. H. K. Leung, and C. C. Y. Poon, 'Mobile Health: Design of Flexible and Stretchable Electrophysiological Sensors for Wearable Healthcare Systems', in *2014 11th International Conference on Wearable and Implantable Body Sensor Networks*, Jun. 2014, pp. 87–91. doi: 10.1109/BSN.2014.25.

[5] C. Guo, Y. Yu, and J. Liu, 'Rapidly patterning conductive components on skin substrates as physiological testing devices via liquid metal spraying and pre-designed mask', *J. Mater. Chem. B*, vol. 2, no. 35, pp. 5739–5745, Aug. 2014, doi: 10.1039/C4TB00660G.

[6] H.-S. Koo *et al.*, 'Physical chromaticity of colorant resist of color filter prepared by inkjet printing technology', *Appl. Phys. Lett.*, vol. 88, no. 11, p. 111908, Mar. 2006, doi: 10.1063/1.2183816.

[7] S. Arumugam *et al.*, 'Spray-Coated Organic Light-Emitting Electrochemical Cells Realized on a Standard Woven Polyester Cotton Textile', *IEEE Trans. Electron Devices*, vol. 68, no. 4, pp. 1717–1722, Apr. 2021, doi: 10.1109/TED.2021.3059809.

[8] S. Yong, S. Beeby, and K. Yang, 'Flexible Supercapacitor Fabricated on a Polyester-Cotton Textile', *Proceedings*, vol. 68, no. 1, p. 7, Jan. 2021, doi: 10.3390/proceedings2021068007.

[9] M.-M. Laurila *et al.*, 'A Fully Printed Ultra-Thin Charge Amplifier for On-Skin Biosignal Measurements', *IEEE J. Electron Devices Soc.*, vol. 7, pp. 566–574, 2019, doi: 10.1109/JEDS.2019.2915028.

[10] S. Demuru, A. Marette, W. Kooli, P. Junier, and D. Briand, 'Flexible Organic Electrochemical Transistor with Functionalized Inkjet-Printed Gold Gate for Bacteria Sensing', in *2019 20th International Conference on Solid-State Sensors, Actuators and Microsystems Eurosensors XXXIII (TRANSDUCERS EUROSENSORS XXXIII)*, Jun. 2019, pp. 2519–2522. doi: 10.1109/TRANSDUCERS.2019.8808309.

[11] S. Singh, Y. Takeda, H. Matsui, and S. Tokito, 'Flexible PMOS Inverter and NOR Gate Using Inkjet-Printed Dual-Gate Organic Thin Film Transistors', *IEEE Electron Device Lett.*, vol. 41, no. 3, pp. 409–412, Mar. 2020, doi: 10.1109/LED.2020.2969275.

[12] F. Molina-Lopez *et al.*, 'Inkjet-printed stretchable and low voltage synaptic transistor array', *Nat Commun*, vol. 10, no. 1, p. 2676, Jun. 2019, doi: 10.1038/s41467-019-10569-3.

[13] X. Feng, A. Scholz, M. B. Tahoori, and J. Aghassi-Hagmann, 'An Inkjet-Printed Full-Wave Rectifier for Low-Voltage Operation Using Electrolyte-Gated Indium-Oxide Thin-Film Transistors', *IEEE Trans. Electron Devices*, vol. 67, no. 11, pp. 4918–4923, Nov. 2020, doi: 10.1109/TED.2020.3020288.

[14] X. Feng, C. Punckt, G. C. Marques, M. Hefenbrock, M. B. Tahoori, and J. Aghassi-Hagmann, ‘Impact of Intrinsic Capacitances on the Dynamic Performance of Printed Electrolyte-Gated Inorganic Field Effect Transistors’, *IEEE Trans. Electron Devices*, vol. 66, no. 8, pp. 3365–3370, Aug. 2019, doi: 10.1109/TED.2019.2919933.

[15] G. C. Marques *et al.*, ‘Printed Logic Gates Based on Enhancement- and Depletion-Mode Electrolyte-Gated Transistors’, *IEEE Trans. Electron Devices*, vol. 67, no. 8, pp. 3146–3151, Aug. 2020, doi: 10.1109/TED.2020.3002208.

[16] R. A. John *et al.*, ‘Low-Temperature Chemical Transformations for High-Performance Solution-Processed Oxide Transistors’, *Chem. Mater.*, vol. 28, no. 22, pp. 8305–8313, Nov. 2016, doi: 10.1021/acs.chemmater.6b03499.

[17] N. Kumar, J. Kumar, and S. Panda, ‘Back-Channel Electrolyte-Gated a-IGZO Dual-Gate Thin-Film Transistor for Enhancement of pH Sensitivity Over Nernst Limit’, *IEEE Electron Device Letters*, vol. 37, no. 4, pp. 500–503, Apr. 2016, doi: 10.1109/LED.2016.2536359.

[18] P. Kesorn *et al.*, ‘Low Temperature High-k Solution Processed Hybrid Gate Insulator for High Performance Amorphous In-Ga-Zn-O Thin-Film Transistors’, in *2019 26th International Workshop on Active-Matrix Flatpanel Displays and Devices (AM-FPD)*, Jul. 2019, pp. 1–2. doi: 10.23919/AM-FPD.2019.8830627.

[19] J. Reker, T. Meyers, F. F. Vidor, and U. Hilleringmann, ‘Deposition of ZnO nanoparticles for thin-film transistors by doctor blade process’, in *2017 IEEE AFRICON*, Sep. 2017, pp. 634–638. doi: 10.1109/AFRCON.2017.8095556.

[20] T. E. Becker, F. F. Vidor, G. I. Wirth, T. Meyers, J. Reker, and U. Hilleringmann, ‘Time domain electrical characterization in zinc oxide nanoparticle thin-film transistors’, in *2018 IEEE 19th Latin-American Test Symposium (LATS)*, Mar. 2018, pp. 1–6. doi: 10.1109/LATW.2018.8349695.

[21] J. Carvalho *et al.*, ‘Fully Printed Zinc Oxide Electrolyte-Gated Transistors on Paper’, *Nanomaterials*, vol. 9, no. 2, p. 169, Jan. 2019, doi: 10.3390/nano9020169.

[22] J. D. Akrofi *et al.*, ‘Multi-stack insulator to minimise threshold voltage drift in ZnO FET sensors operating in ionic solutions’, *Micro and Nano Engineering*, vol. 8, p. 100066, Aug. 2020, doi: 10.1016/j.mne.2020.100066.

[23] S. Faisal *et al.*, ‘Green Synthesis of Zinc Oxide (ZnO) Nanoparticles Using Aqueous Fruit Extracts of Myristica fragrans: Their Characterizations and Biological and Environmental Applications’, *ACS Omega*, vol. 6, no. 14, pp. 9709–9722, Apr. 2021, doi: 10.1021/acsomega.1c00310.

[24] F. F. Vidor, T. Meyers, U. Hilleringmann, and G. I. Wirth, ‘Influence of UV irradiation and humidity on a low-cost ZnO nanoparticle TFT for flexible electronics’, in *2015 IEEE 15th International Conference on Nanotechnology (IEEE-NANO)*, Jul. 2015, pp. 1179–1181. doi: 10.1109/NANO.2015.7388836.

[25] F. F. Vidor, G. Wirth, F. Assion, K. Wolff, and U. Hilleringmann, ‘Characterization and Analysis of the Hysteresis in a ZnO Nanoparticle Thin-Film Transistor’, *IEEE Transactions on Nanotechnology*, vol. 12, no. 3, pp. 296–303, May 2013, doi: 10.1109/TNANO.2012.2236891.

[26] D. D. Zhou, ‘Microelectrodes for in-vivo determination of pH’, in *Electrochemical Sensors, Biosensors and their Biomedical Applications*, Elsevier, 2008, pp. 261–305. doi: 10.1016/B978-012373738-0.50012-X.

[27] T. Guinovart, G. Valdés-Ramírez, J. R. Windmiller, F. J. Andrade, and J. Wang, ‘Bandage-Based Wearable Potentiometric Sensor for Monitoring Wound pH’, *Electroanalysis*, vol. 26, no. 6, pp. 1345–1353, 2014, doi: 10.1002/elan.201300558.

[28] L. Manjakkal, D. Szwagierczak, and R. Dahiya, ‘Metal oxides based electrochemical pH sensors: Current progress and future perspectives’, *Progress in Materials Science*, vol. 109, p. 100635, Apr. 2020, doi: 10.1016/j.pmatsci.2019.100635.

[29] P.-H. Yang, C.-T. Chan, and Y.-S. Zhang, ‘ZnO Film Flexible Printed Circuit Board pH Sensor Measurement and Characterization’, *IEEE Access*, vol. 10, pp. 96091–96099, 2022, doi: 10.1109/ACCESS.2022.3205320.

[30] M. Taheri, M. Ketabi, A. M. Al Shboul, S. Mahinnezhad, R. Izquierdo, and M. J. Deen, ‘Integrated pH Sensors Based on RuO2/GO Nanocomposites Fabricated Using the Aerosol Jet Printing Method’, *ACS Omega*, vol. 8, no. 49, pp. 46794–46803, Dec. 2023, doi: 10.1021/acsomega.3c06309.

[31] L. Santos *et al.*, ‘WO3 Nanoparticle-Based Conformable pH Sensor’, *ACS Appl. Mater. Interfaces*, vol. 6, no. 15, pp. 12226–12234, Aug. 2014, doi: 10.1021/am501724h.

[32] S.-C. Chou *et al.*, ‘A flexible IrO2 membrane for pH sensing’, *Sci Rep*, vol. 12, no. 1, p. 11712, Jul. 2022, doi: 10.1038/s41598-022-15961-6.

[33] A. Menzel, K. Subannajui, F. Güder, D. Moser, O. Paul, and M. Zacharias, ‘Multifunctional ZnO-Nanowire-Based Sensor’, *Advanced Functional Materials*, vol. 21, no. 22, pp. 4342–4348, 2011, doi: 10.1002/adfm.201101549.

[34] G. K. Mani, M. Morohoshi, Y. Yasoda, S. Yokoyama, H. Kimura, and K. Tsuchiya, ‘ZnO-Based Microfluidic pH Sensor: A Versatile Approach for Quick Recognition of Circulating Tumor Cells in Blood’, *ACS Appl. Mater. Interfaces*, vol. 9, no. 6, pp. 5193–5203, Feb. 2017, doi: 10.1021/acsami.6b16261.

[35] Y.-L. Chu, S.-J. Young, S.-H. Tsai, S. Arya, and T.-T. Chu, ‘High Sensitivity of Extended-Gate Field-Effect Transistors Based on 1-D ZnO:Ag Nanomaterials through a Cheap Photochemical Synthesis as pH Sensors at Room Temperature’, *ACS Appl. Electron. Mater.*, vol. 6, no. 2, pp. 712–723, Feb. 2024, doi: 10.1021/acsaelm.3c01138.

[36] P. Dwivedi, R. Singh, and Y. S. Chauhan, ‘Crossing the Nernst Limit (59 mV/pH) of Sensitivity Through Tunneling Transistor-Based Biosensor’, *IEEE Sensors J.*, vol. 21, no. 3, pp. 3233–3240, Feb. 2021, doi: 10.1109/JSEN.2020.3025975.

[37] S. Nakata, M. Shiomi, Y. Fujita, T. Arie, S. Akita, and K. Takei, ‘A wearable pH sensor with high sensitivity based on a flexible charge-coupled device’, *Nat Electron*, vol. 1, no. 11, pp. 596–603, Nov. 2018, doi: 10.1038/s41928-018-0162-5.

[38] S. Raha and M. Ahmaruzzaman, ‘ZnO nanostructured materials and their potential applications: progress, challenges and perspectives’, *Nanoscale Advances*, vol. 4, no. 8, pp. 1868–1925, 2022, doi: 10.1039/D1NA00880C.

[39] B. D. Rowlinson, J. Zeng, J. D. Akrofi, C. Patzig, M. Ebert, and H. M. H. Chong, ‘Atomic Layer Deposition of Al-Doped ZnO Contacts for ZnO Thin-Film Transistors’, *IEEE Electron Device Letters*, vol. 45, no. 5, pp. 837–840, May 2024, doi: 10.1109/LED.2024.3382408.

[40] M. McKinlay *et al.*, ‘On the Piezoelectric Properties of Zinc Oxide Thin Films Synthesized by Plasma Assisted DC Sputter Deposition’, *Advanced Materials Interfaces*, vol. 11, no. 32, p. 2400252, 2024, doi: 10.1002/admi.202400252.

[41] M. Qu *et al.*, ‘Solution-Processed Low Resistivity Zinc Oxide Nanoparticle Film with Enhanced Stability Using EVOH’, *ACS Appl. Electron. Mater.*, May 2024, doi: 10.1021/acsaelm.4c00355.

[42] D. G. Georgiadou *et al.*, ‘100 GHz zinc oxide Schottky diodes processed from solution on a wafer scale’, *Nat Electron*, vol. 3, no. 11, pp. 718–725, Nov. 2020, doi: 10.1038/s41928-020-00484-7.

[43] F. Liu, A. Christou, R. Chirila, L. De Pamphilis, and R. Dahiya, ‘Stochastic Nature of Large-Scale Contact Printed ZnO Nanowires Based Transistors’, *Advanced Functional Materials*, vol. n/a, no. n/a, p. 2412299, doi: 10.1002/adfm.202412299.

[44] J. Chen *et al.*, ‘A Fully Printed ZnO Memristor Synaptic Array for Neuromorphic Computing Application’, *IEEE Electron Device Letters*, vol. 45, no. 6, pp. 1076–1079, Jun. 2024, doi: 10.1109/LED.2024.3387455.

[45] M. Choi *et al.*, ‘High figure-of-merit for ZnO nanostructures by interfacing lowly-oxidized graphene quantum dots’, *Nat Commun*, vol. 15, no. 1, p. 1996, Mar. 2024, doi: 10.1038/s41467-024-46182-2.

[46] Y.-H. Lin *et al.*, ‘Hybrid organic–metal oxide multilayer channel transistors with high operational stability’, *Nat Electron*, vol. 2, no. 12, pp. 587–595, Dec. 2019, doi: 10.1038/s41928-019-0342-y.

[47] D. Weber, S. Botnaraş, D. V. Pham, J. Steiger, and L. D. Cola, ‘Functionalized ZnO nanoparticles for thin-film transistors: support of ligand removal by non-thermal methods’, *J. Mater. Chem. C*, vol. 1, no. 18, pp. 3098–3103, Apr. 2013, doi: 10.1039/C3TC00576C.

[48] D. Lee *et al.*, ‘All 3D-Printed Flexible ZnO UV Photodetector on an Ultraflat Substrate’, *ACS Sens.*, vol. 5, no. 4, pp. 1028–1032, Apr. 2020, doi: 10.1021/acssensors.9b02544.

[49] P.-Q. Pham *et al.*, ‘Synaptic behavior in analog memristors based on green-synthesized ZnO nanoparticles’, *Ceramics International*, vol. 50, no. 16, pp. 28480–28489, Aug. 2024, doi: 10.1016/j.ceramint.2024.05.154.

[50] J. Fan *et al.*, ‘PEDOT-ZnO Nanoparticle Hybrid Film-Based Memristors for Synapse Emulation in Neuromorphic Computing Applications’, *ACS Appl. Nano Mater.*, vol. 7, no. 5, pp. 5661–5668, Mar. 2024, doi: 10.1021/acsanm.4c00759.

[51] Y. Wang *et al.*, ‘A Digital–Analog Integrated Memristor Based on a ZnO NPs/CuO NWs Heterostructure for Neuromorphic Computing’, *ACS Appl. Electron. Mater.*, vol. 4, no. 7, pp. 3525–3534, Jul. 2022, doi: 10.1021/acsaelm.2c00495.

[52] A. Janotti and C. G. Van de Walle, ‘Fundamentals of zinc oxide as a semiconductor’, *Rep. Prog. Phys.*, vol. 72, no. 12, p. 126501, Dec. 2009, doi: 10.1088/0034-4885/72/12/126501.

[53] S. Wang *et al.*, ‘Fabrication of ZnO Nanoparticles Modified by Uniformly Dispersed Ag Nanoparticles: Enhancement of Gas Sensing Performance’, *ACS Omega*, vol. 5, no. 10, pp. 5209–5218, Mar. 2020, doi: 10.1021/acsomega.9b04243.

[54] J.-C. Jian, Y.-C. Chang, S.-P. Chang, and S.-J. Chang, ‘Biotemplate-Assisted Growth of ZnO in Gas Sensors for ppb-Level NO2 Detection’, *ACS Omega*, vol. 9, no. 1, pp. 1077–1083, Jan. 2024, doi: 10.1021/acsomega.3c07280.

[55] G. Faraji, H. S. Kim, and H. T. Kashi, ‘Introduction’, in *Severe Plastic Deformation*, Elsevier, 2018, pp. 1–17. doi: 10.1016/B978-0-12-813518-1.00020-5.

[56] J.-O. Carlsson and P. M. Martin, ‘Chapter 7 - Chemical Vapor Deposition’.

[57] V. Galstyan, M. Bhandari, V. Sberveglieri, G. Sberveglieri, and E. Comini, ‘Metal Oxide Nanostructures in Food Applications: Quality Control and Packaging’, *Chemosensors*, vol. 6, no. 2, p. 16, Apr. 2018, doi: 10.3390/chemosensors6020016.

[58] L. Jiang *et al.*, ‘Low-Temperature and Solution-Processable Zinc Oxide Transistors for Transparent Electronics’, *ACS Omega*, vol. 2, no. 12, pp. 8990–8996, Dec. 2017, doi: 10.1021/acsomega.7b01420.

[59] W. Liu, H. Dong, D. Wang, and X. Chen, ‘Precursor-based zno nano inks for printed electronics**’, in *2021 IEEE 16th International Conference on Nano/Micro Engineered and Molecular Systems (NEMS)*, Apr. 2021, pp. 144–147. doi: 10.1109/NEMS51815.2021.9451491.

[60] X. Liu, M. Wegener, S. Polster, M. P. M. Jank, A. Roosen, and L. Frey, ‘Materials Integration for Printed Zinc Oxide Thin-Film Transistors: Engineering of a Fully-Printed Semiconductor/Contact Scheme’, *Journal of Display Technology*, vol. 12, no. 3, pp. 214–218, Mar. 2016, doi: 10.1109/JDT.2015.2445378.

[61] C. Li, Y. Vaynzof, G. Lakhwani, G. J. Beirne, J. Wang, and N. C. Greenham, ‘Observation of oxygen vacancy migration in memory devices based on ZnO nanoparticles’, *Journal of Applied Physics*, vol. 121, no. 14, p. 144503, Apr. 2017, doi: 10.1063/1.4979973.

[62] S. Khan, S. Ali, A. Khan, B. Wang, and A. Bermak, ‘Printing Sensors on Biocompatible Substrates for Selective Detection of Glucose’, *IEEE Sensors J.*, vol. 21, no. 4, pp. 4167–4175, Feb. 2021, doi: 10.1109/JSEN.2020.3032539.

[63] W. Wu, ‘Inorganic nanomaterials for printed electronics: a review’, *Nanoscale*, vol. 9, no. 22, pp. 7342–7372, Jun. 2017, doi: 10.1039/C7NR01604B.

[64] W. G. Whittow *et al.*, ‘Inkjet-Printed Microstrip Patch Antennas Realized on Textile for Wearable Applications’, *IEEE Antennas and Wireless Propagation Letters*, vol. 13, pp. 71–74, 2014, doi: 10.1109/LAWP.2013.2295942.

[65] Y. Li, R. Torah, S. Beeby, and J. Tudor, ‘An all-inkjet printed flexible capacitor on a textile using a new poly(4-vinylphenol) dielectric ink for wearable applications’, in *2012 IEEE SENSORS*, Oct. 2012, pp. 1–4. doi: 10.1109/ICSENS.2012.6411117.

[66] D. Godlinski, R. Zichner, V. Zöllmer, and R. R. Baumann, ‘Printing technologies for the manufacturing of passive microwave components: antennas’, *IET Microwaves, Antennas & Propagation*, vol. 11, no. 14, pp. 2010–2015, 2017, doi: 10.1049/iet-map.2017.0042.

[67] F. Wang, P. Mao, and H. He, ‘Dispensing of high concentration Ag nano-particles ink for ultra-low resistivity paper-based writing electronics’, *Sci Rep*, vol. 6, no. 1, p. 21398, Aug. 2016, doi: 10.1038/srep21398.

[68] M. Liu, Z. Ahmed, N. Grabham, S. Beeby, J. Tudor, and K. Yang, ‘An All Dispenser Printed Electrode Structure on Textile for Wearable Healthcare’, *Engineering Proceedings*, vol. 15, no. 1, Art. no. 1, 2022, doi: 10.3390/engproc2022015016.

[69] F. Rasheed, M. Rommel, G. C. Marques, W. Wenzel, M. B. Tahoori, and J. Aghassi-Hagmann, ‘Channel Geometry Scaling Effect in Printed Inorganic Electrolyte-Gated Transistors’, *IEEE Transactions on Electron Devices*, vol. 68, no. 4, pp. 1866–1871, Apr. 2021, doi: 10.1109/TED.2021.3058929.

[70] G. C. Marques *et al.*, ‘Electrolyte-Gated FETs Based on Oxide Semiconductors: Fabrication and Modeling’, *IEEE Transactions on Electron Devices*, vol. 64, no. 1, pp. 279–285, Jan. 2017, doi: 10.1109/TED.2016.2621777.

[71] P. A. Ersman *et al.*, 'Screen printed digital circuits based on vertical organic electrochemical transistors', *Flex. Print. Electron.*, vol. 2, no. 4, p. 045008, Nov. 2017, doi: 10.1088/2058-8585/aa903a.

[72] C. Jiang, X. Cheng, C. P. Tsangarides, Y. Su, H. Ma, and A. Nathan, 'Ultralow-Power All-Inkjet-Printed Organic Thin-Film Transistors for Wearables', in *2020 4th IEEE Electron Devices Technology & Manufacturing Conference (EDTM)*, Penang, Malaysia: IEEE, Apr. 2020, pp. 1–4. doi: 10.1109/EDTM47692.2020.9117953.

[73] Y. Li *et al.*, 'Fully Printed Top-Gate Metal–Oxide Thin-Film Transistors Based on Scandium-Zirconium-Oxide Dielectric', *IEEE Trans. Electron Devices*, vol. 66, no. 1, pp. 445–450, Jan. 2019, doi: 10.1109/TED.2018.2877979.

[74] H. Huang *et al.*, 'Electrolyte-gated transistors for neuromorphic applications', *J. Semicond.*, vol. 42, no. 1, p. 013103, Jan. 2021, doi: 10.1088/1674-4926/42/1/013103.

[75] G. Y. Wang, K. Lian, and T.-Y. Chu, 'Electrolyte-gated field effect transistors in biological sensing: a survey of electrolytes', *IEEE Journal of the Electron Devices Society*, pp. 1–1, 2021, doi: 10.1109/JEDS.2021.3082420.

[76] S. H. Kim, S. H. Lee, Y. G. Kim, and J. Jang, 'Ink-Jet-Printed Organic Thin-Film Transistors for Low-Voltage-Driven CMOS Circuits With Solution-Processed AlOX Gate Insulator', *IEEE Electron Device Letters*, vol. 34, no. 2, pp. 307–309, Feb. 2013, doi: 10.1109/LED.2012.2228461.

[77] T. S. Zhao *et al.*, 'Solution Processed ZnSnO Thin-film Transistors with Peroxide-Aluminum Oxide Dielectric', in *2019 International Conference on IC Design and Technology (ICICDT)*, Jun. 2019, pp. 1–4. doi: 10.1109/ICICDT.2019.8790915.

[78] C. Liu, Q. Tian, and L. Liao, 'Sol–gel precursor inks and films', in *Solution Processed Metal Oxide Thin Films for Electronic Applications*, Elsevier, 2020, pp. 41–61. doi: 10.1016/B978-0-12-814930-0.00004-9.

[79] W. Lee *et al.*, 'High colloidal stability ZnO nanoparticles independent on solvent polarity and their application in polymer solar cells', *Sci Rep*, vol. 10, no. 1, p. 18055, Dec. 2020, doi: 10.1038/s41598-020-75070-0.

[80] Y. Huang, 'Metallic nanoparticle ink formulation development and optimization for electrohydrodynamic ink-jet printing', Master of Science, Iowa State University, 2020. doi: 10.31274/etd-20200902-64.

[81] X. Sun, F. Azad, S. Wang, L. Zhao, and S. Su, 'Low-Cost Flexible ZnO Microwires Array Ultraviolet Photodetector Embedded in PAVL Substrate', *Nanoscale Res Lett*, vol. 13, no. 1, p. 277, Dec. 2018, doi: 10.1186/s11671-018-2701-4.

[82] A. A. G. Santiago *et al.*, 'Development of ZnO/PDMS nanocomposite with photocatalytic/hydrophobic multifunction', *Chemical Physics Letters*, vol. 740, p. 137051, Feb. 2020, doi: 10.1016/j.cplett.2019.137051.

[83] I. Miranda *et al.*, 'Properties and Applications of PDMS for Biomedical Engineering: A Review', *Journal of Functional Biomaterials*, vol. 13, no. 1, Art. no. 1, Mar. 2022, doi: 10.3390/jfb13010002.

[84] K. Sadeghi and M. Shahedi, 'Effect of Zinc Oxide Nanoparticles on Barrier and Mechanical Properties of EVOH Nanocomposite film Incorporating with Plasticizer', *JFNR*, vol. 4, no. 11, pp. 709–712, Dec. 2016, doi: 10.12691/jfnr-4-11-2.

[85] C. Maes, W. Luyten, G. Herremans, R. Peeters, R. Carleer, and M. Buntinx, ‘Recent Updates on the Barrier Properties of Ethylene Vinyl Alcohol Copolymer (EVOH): A Review’, *Polymer Reviews*, vol. 58, no. 2, pp. 209–246, Apr. 2018, doi: 10.1080/15583724.2017.1394323.

[86] J. H. Jang *et al.*, ‘A Novel Approach for the Development of Moisture Encapsulation Poly(vinyl alcohol-co-ethylene) for Perovskite Solar Cells’, *ACS Omega*, vol. 4, no. 5, pp. 9211–9218, May 2019, doi: 10.1021/acsomega.9b00350.

[87] S. Yong, J. Shi, and S. Beeby, ‘Wearable Textile Power Module Based on Flexible Ferroelectret and Supercapacitor’, *Energy Technology*, vol. 7, no. 5, p. 1800938, 2019, doi: 10.1002/ente.201800938.

[88] M. Naskar, D. H M, and M. K P, ‘Influence of Nano Zinc Oxide on EVA Encapsulant Material for Photovoltaic Applications’, in *2021 IEEE 5th International Conference on Condition Assessment Techniques in Electrical Systems (CATCON)*, Dec. 2021, pp. 186–189. doi: 10.1109/CATCON52335.2021.9670503.

[89] D. Hiscott, M. Cvetkovska, M. A. Mumin, and P. A. Charpentier, ‘Light Downshifting ZnO-EVA Nanocomposite Greenhouse Films and Their Influence on Photosynthetic Green Algae Growth’, *ACS Appl. Polym. Mater.*, vol. 3, no. 8, pp. 3800–3810, Aug. 2021, doi: 10.1021/acsapm.1c00396.

[90] M. A. Y. Barakat and A. E.-A. A. El-Wakil, ‘Preparation and characterization of EVA/ZnO composites as piezoelectric elements for ultrasonic transducers’, *Mater. Res. Express*, vol. 8, no. 10, p. 105304, Oct. 2021, doi: 10.1088/2053-1591/ac29fb.

[91] Y. Li, F. Della Valle, M. Simonnet, I. Yamada, and J.-J. Delaunay, ‘Competitive surface effects of oxygen and water on UV photoresponse of ZnO nanowires’, *Appl. Phys. Lett.*, vol. 94, no. 2, p. 023110, Jan. 2009, doi: 10.1063/1.3073042.

[92] Y. Jin, J. Wang, B. Sun, J. C. Blakesley, and N. C. Greenham, ‘Solution-Processed Ultraviolet Photodetectors Based on Colloidal ZnO Nanoparticles’, *Nano Lett.*, vol. 8, no. 6, pp. 1649–1653, Jun. 2008, doi: 10.1021/nl0803702.

[93] C. B. Jacobs *et al.*, ‘UV-activated ZnO films on a flexible substrate for room temperature O2 and H2O sensing’, *Sci Rep*, vol. 7, no. 1, Art. no. 1, Jul. 2017, doi: 10.1038/s41598-017-05265-5.

[94] L. C.-K. Liau and Y.-H. Lin, ‘Effects of electric fields on the conduction of polyvinyl alcohol (PVA)/ZnO films by photoluminescence analysis’, *Journal of Luminescence*, vol. 181, pp. 217–222, Jan. 2017, doi: 10.1016/j.jlumin.2016.08.067.

[95] W. Han, J. Kim, and H.-H. Park, ‘Control of electrical conductivity of highly stacked zinc oxide nanocrystals by ultraviolet treatment’, *Scientific Reports*, vol. 9, Apr. 2019, doi: 10.1038/s41598-019-42102-3.

[96] Y. Guo *et al.*, ‘A new strategy to minimize humidity influences on acoustic wave ultraviolet sensors using ZnO nanowires wrapped with hydrophobic silica nanoparticles’, *Microsyst Nanoeng*, vol. 8, no. 1, Art. no. 1, Nov. 2022, doi: 10.1038/s41378-022-00455-2.

[97] D. J. Graham, B. Jaselskis, and C. E. Moore, ‘Development of the Glass Electrode and the pH Response’, *J. Chem. Educ.*, vol. 90, no. 3, pp. 345–351, Mar. 2013, doi: 10.1021/ed300246x.

[98] M. W. Shinwari, D. Zhitomirsky, I. A. Deen, P. R. Selvaganapathy, M. J. Deen, and D. Landheer, ‘Microfabricated Reference Electrodes and their Biosensing Applications’, *Sensors*, vol. 10, no. 3, Art. no. 3, Mar. 2010, doi: 10.3390/s100301679.

[99] A. U. Alam *et al.*, ‘Polymers and organic materials-based pH sensors for healthcare applications’, *Progress in Materials Science*, vol. 96, pp. 174–216, Jul. 2018, doi: 10.1016/j.pmatsci.2018.03.008.

[100] D. E. Yates, S. Levine, and T. W. Healy, ‘Site-binding model of the electrical double layer at the oxide/water interface’, *J. Chem. Soc., Faraday Trans. 1*, vol. 70, no. 0, pp. 1807–1818, Jan. 1974, doi: 10.1039/F19747001807.

[101] P. D. Batista and M. Mulato, ‘ZnO extended-gate field-effect transistors as pH sensors’, *Applied Physics Letters*, vol. 87, no. 14, p. 143508, Sep. 2005, doi: 10.1063/1.2084319.

[102] H.-H. Li *et al.*, ‘Coaxial-structured ZnO/silicon nanowires extended-gate field-effect transistor as pH sensor’, *Thin Solid Films*, vol. 529, pp. 173–176, Feb. 2013, doi: 10.1016/j.tsf.2012.05.045.

[103] W.-D. Huang, H. Cao, S. Deb, M. Chiao, and J. C. Chiao, ‘A flexible pH sensor based on the iridium oxide sensing film’, *Sensors and Actuators A: Physical*, vol. 169, no. 1, pp. 1–11, Sep. 2011, doi: 10.1016/j.sna.2011.05.016.

[104] R. Haarindraprasad *et al.*, ‘Low Temperature Annealed Zinc Oxide Nanostructured Thin Film-Based Transducers: Characterization for Sensing Applications’, *PLOS ONE*, vol. 10, no. 7, p. e0132755, Jul. 2015, doi: 10.1371/journal.pone.0132755.

[105] Y.-S. Chiu and C.-T. Lee, ‘pH Sensor Investigation of Various-Length Photoelectrochemical Passivated ZnO Nanorod Arrays’, *J. Electrochem. Soc.*, vol. 158, no. 9, p. J282, Jul. 2011, doi: 10.1149/1.3610399.

[106] Y. Bai, R. Zhu, J. Zhao, and G. Cui, ‘Super-Nernstian model based on acid doped polyaniline pH sensor’, *Microchemical Journal*, vol. 203, p. 110715, Aug. 2024, doi: 10.1016/j.microc.2024.110715.

[107] M. Shayesteh *et al.*, ‘N-type doped germanium contact resistance extraction and evaluation for advanced devices’, in *2011 Proceedings of the European Solid-State Device Research Conference (ESSDERC)*, Sep. 2011, pp. 235–238. doi: 10.1109/ESSDERC.2011.6044191.

[108] H. Idriss, ‘On the wrong assignment of the XPS O1s signal at 531–532 eV attributed to oxygen vacancies in photo- and electro-catalysts for water splitting and other materials applications’, *Surface Science*, vol. 712, p. 121894, Oct. 2021, doi: 10.1016/j.susc.2021.121894.

[109] Fitriana, N. L. W. Septiani, D. R. Adhika, A. G. Saputro, Nugraha, and B. Yuliarto, ‘Enhanced NO Gas Performance of (002)-Oriented Zinc Oxide Nanostructure Thin Films’, *IEEE Access*, vol. 7, pp. 155446–155454, 2019, doi: 10.1109/ACCESS.2019.2949463.

[110] S. A. Khan *et al.*, ‘A Full-Range Flexible and Printed Humidity Sensor Based on a Solution-Processed P(VDF-TrFE)/Graphene-Flower Composite’, *Nanomaterials*, vol. 11, no. 8, Art. no. 8, Aug. 2021, doi: 10.3390/nano11081915.

[111] I. R. Kaufmann, O. Zerey, T. Meyers, J. Reker, F. Vidor, and U. Hilleringmann, ‘A Study about Schottky Barrier Height and Ideality Factor in Thin Film Transistors with Metal/Zinc Oxide Nanoparticles Structures Aiming Flexible Electronics Application’, *Nanomaterials*, vol. 11, no. 5, Art. no. 5, May 2021, doi: 10.3390/nano11051188.

[112] P. K. Basu, N. Saha, S. Maji, H. Saha, and S. Basu, ‘Nanoporous ZnO thin films deposited by electrochemical anodization: effect of UV light’, *J Mater Sci: Mater Electron*, vol. 19, no. 6, pp. 493–499, Jun. 2008, doi: 10.1007/s10854-008-9604-6.

[113] L. Wan *et al.*, ‘Effects of Interfacial Passivation on the Electrical Performance, Stability, and Contact Properties of Solution Process Based ZnO Thin Film Transistors’, *Materials*, vol. 11, no. 9, Art. no. 9, Sep. 2018, doi: 10.3390/ma11091761.

[114] S.-J. Seo, S. Yang, J.-H. Ko, and B.-S. Bae, ‘Effects of Sol-Gel Organic-Inorganic Hybrid Passivation on Stability of Solution-Processed Zinc Tin Oxide Thin Film Transistors’, *Electrochem. Solid-State Lett.*, vol. 14, no. 9, p. H375, 2011, doi: 10.1149/1.3603845.

[115] S. K. Garlapati *et al.*, ‘Electrolyte-Gated, High Mobility Inorganic Oxide Transistors from Printed Metal Halides’, *ACS Appl. Mater. Interfaces*, vol. 5, no. 22, pp. 11498–11502, Nov. 2013, doi: 10.1021/am403131j.

[116] F. Verbakel, S. C. J. Meskers, and R. A. J. Janssen, ‘Electronic memory effects in diodes of zinc oxide nanoparticles in a matrix of polystyrene or poly(3-hexylthiophene)’, *Journal of Applied Physics*, vol. 102, no. 8, p. 083701, Oct. 2007, doi: 10.1063/1.2794475.

[117] A. G. Saputro, F. T. Akbar, N. P. P. Setyagar, M. K. Agusta, A. D. Pramudya, and H. K. Dipojono, ‘Effect of surface defects on the interaction of the oxygen molecule with the ZnO(1010) surface’, *New J. Chem.*, vol. 44, no. 18, pp. 7376–7385, 2020, doi: 10.1039/C9NJ06338B.

[118] M. A. Franco, P. P. Conti, R. S. Andre, and D. S. Correa, ‘A review on chemiresistive ZnO gas sensors’, *Sensors and Actuators Reports*, vol. 4, p. 100100, Nov. 2022, doi: 10.1016/j.snr.2022.100100.

[119] H. Ji, W. Zeng, and Y. Li, ‘Gas sensing mechanisms of metal oxide semiconductors: a focus review’, *Nanoscale*, vol. 11, no. 47, pp. 22664–22684, Dec. 2019, doi: 10.1039/C9NR07699A.

[120] A. Pickett *et al.*, ‘UV–Ozone Modified Sol–Gel Processed ZnO for Improved Diketopyrrolopyrrole-Based Hybrid Photodetectors’, *ACS Appl. Electron. Mater.*, vol. 1, no. 11, pp. 2455–2462, Nov. 2019, doi: 10.1021/acsaelm.9b00597.

[121] K.-H. Park, G. D. Han, K. C. Neoh, T.-S. Kim, J. H. Shim, and H.-D. Park, ‘Antibacterial activity of the thin ZnO film formed by atomic layer deposition under UV-A light’, *Chemical Engineering Journal*, vol. 328, pp. 988–996, Nov. 2017, doi: 10.1016/j.cej.2017.07.112.

[122] D. Kim, H. K. Woo, Y. M. Lee, Y. Kim, J.-H. Choi, and S. J. Oh, ‘Controllable doping and passivation of ZnO thin films by surface chemistry modification to design low-cost and high-performance thin film transistors’, *Applied Surface Science*, vol. 509, p. 145289, Apr. 2020, doi: 10.1016/j.apsusc.2020.145289.

[123] Ping Wu *et al.*, ‘Instability Induced by Ultraviolet Light in ZnO Thin-Film Transistors’, *IEEE Trans. Electron Devices*, vol. 61, no. 5, pp. 1431–1435, May 2014, doi: 10.1109/TED.2014.2312947.

[124] X. Wei, S. Kumagai, M. Sasaki, S. Watanabe, and J. Takeya, ‘Stabilizing solution-processed metal oxide thin-film transistors via trilayer organic–inorganic hybrid passivation’, *AIP Advances*, vol. 11, no. 3, p. 035027, Mar. 2021, doi: 10.1063/5.0038128.

[125] A. T. Vai, V. L. Kuznetsov, J. R. Dilworth, and P. P. Edwards, ‘UV-induced improvement in ZnO thin film conductivity: a new in situ approach’, *J. Mater. Chem. C*, vol. 2, no. 45, pp. 9643–9652, Oct. 2014, doi: 10.1039/C4TC01749H.

[126] H.-D. Huang *et al.*, ‘Promising strategies and new opportunities for high barrier polymer packaging films’, *Progress in Polymer Science*, vol. 144, p. 101722, Sep. 2023, doi: 10.1016/j.progpolymsci.2023.101722.

[127] B. A. Morris, '4 - Commonly Used Resins and Substrates in Flexible Packaging', in *The Science and Technology of Flexible Packaging*, B. A. Morris, Ed., in Plastics Design Library. , Oxford: William Andrew Publishing, 2017, pp. 69–119. doi: 10.1016/B978-0-323-24273-8.00004-6.

[128] V. Siracusa, 'Packaging Material in the Food Industry', in *Antimicrobial Food Packaging*, Elsevier, 2016, pp. 95–106. doi: 10.1016/B978-0-12-800723-5.00007-3.

[129] L. W. McKeen, 'Polyvinyls and Acrylics', in *Film Properties of Plastics and Elastomers*, Elsevier, 2012, pp. 219–254. doi: 10.1016/B978-1-4557-2551-9.00010-4.

[130] S. H. Lee, K.-Y. Han, and H. J. Chang, 'Properties of passivation layer formed by solution process on flexible CIGS solar cells', *Molecular Crystals and Liquid Crystals*, vol. 734, no. 1, pp. 47–62, Feb. 2022, doi: 10.1080/15421406.2021.1972213.

[131] K.-J. Heo, G. Tarsoly, J.-Y. Lee, S. G. Choi, J.-H. Koh, and S.-J. Kim, 'Improved Electrical and Temporal Stability of In-Zn Oxide Semiconductor Thin-Film Transistors With Organic Passivation Layer', *IEEE J. Electron Devices Soc.*, vol. 10, pp. 660–665, 2022, doi: 10.1109/JEDS.2022.3194921.

[132] V. Siracusa, 'Food Packaging Permeability Behaviour: A Report', *International Journal of Polymer Science*, vol. 2012, no. 1, p. 302029, 2012, doi: 10.1155/2012/302029.

[133] V. Postica *et al.*, 'Improved Long-Term Stability and Reduced Humidity Effect in Gas Sensing: SiO2 Ultra-Thin Layered ZnO Columnar Films', *Advanced Materials Technologies*, vol. 6, no. 5, p. 2001137, 2021, doi: 10.1002/admt.202001137.

[134] Y. Zhang, Z. Chen, S. Liu, and Y.-J. Xu, 'Size effect induced activity enhancement and anti-photocorrosion of reduced graphene oxide/ZnO composites for degradation of organic dyes and reduction of Cr(VI) in water', *Applied Catalysis B: Environmental*, vol. 140–141, pp. 598–607, Aug. 2013, doi: 10.1016/j.apcatb.2013.04.059.

[135] J. Sebastian *et al.*, 'Preparation and Characterization of ZnSe/EVA Nanocomposites for Photovoltaic Modules', *JMMCE*, vol. 03, no. 04, pp. 215–224, 2015, doi: 10.4236/jmmce.2015.34024.

[136] A. Kubacka, M. L. Cerrada, C. Serrano, M. Fernández-García, M. Ferrer, and M. Fernández-Garcia, 'Plasmonic Nanoparticle/Polymer Nanocomposites with Enhanced Photocatalytic Antimicrobial Properties', *J. Phys. Chem. C*, vol. 113, no. 21, pp. 9182–9190, May 2009, doi: 10.1021/jp901337e.

[137] R. K. Sodhi and S. Paul, 'An Overview of Metal Acetylacetonates: Developing Areas/Routes to New Materials and Applications in Organic Syntheses', *Catal Surv Asia*, vol. 22, no. 1, pp. 31–62, Mar. 2018, doi: 10.1007/s10563-017-9239-9.

[138] C. Li, Y. Vaynzof, G. Lakhwani, G. J. Beirne, J. Wang, and N. C. Greenham, 'Observation of oxygen vacancy migration in memory devices based on ZnO nanoparticles', *Journal of Applied Physics*, vol. 121, no. 14, p. 144503, Apr. 2017, doi: 10.1063/1.4979973.

[139] A. H. Mohamed, N. A. B. Ghazali, H. M. H. Chong, R. J. Cobley, L. Li, and K. Kalna, 'Channel mobility and contact resistance in scaled ZnO thin-film transistors', *Solid-State Electronics*, vol. 172, p. 107867, Oct. 2020, doi: 10.1016/j.sse.2020.107867.

[140] N. Najafi and S. M. Rozati, 'Resistivity Reduction of Nanostructured Undoped Zinc Oxide thin Films for Ag/ZnO Bilayers Using APCVD and Sputtering Techniques', *Mat. Res.*, vol. 21, Mar. 2018, doi: 10.1590/1980-5373-MR-2017-0933.

[141] K. Oura, H. Wada, M. Koyama, T. Maemoto, and S. Sasa, ‘Improved electrical performance of solution-processed zinc oxide-based thin-film transistors with bilayer structures’, *Journal of Information Display*, vol. 23, no. 1, pp. 105–113, Jan. 2022, doi: 10.1080/15980316.2021.2011443.

[142] B. Sanches De Lima *et al.*, ‘Experimental and Theoretical Insights into the Structural Disorder and Gas Sensing Properties of ZnO’, *ACS Appl. Electron. Mater.*, vol. 3, no. 3, pp. 1447–1457, Mar. 2021, doi: 10.1021/acsaelm.1c00058.

[143] T. B. Rawal *et al.*, ‘Interaction of Zinc Oxide Nanoparticles with Water: Implications for Catalytic Activity’, *ACS Applied Nano Materials*, Jun. 2019, doi: 10.1021/acsanm.9b00714.

[144] T. J. Frankcombe and Y. Liu, ‘Interpretation of Oxygen 1s X-ray Photoelectron Spectroscopy of ZnO’, *Chem. Mater.*, vol. 35, no. 14, pp. 5468–5474, Jul. 2023, doi: 10.1021/acs.chemmater.3c00801.

[145] Y. Tu *et al.*, ‘Control of oxygen vacancies in ZnO nanorods by annealing and their influence on ZnO/PEDOT:PSS diode behaviour’, *J. Mater. Chem. C*, vol. 6, no. 7, pp. 1815–1821, 2018, doi: 10.1039/C7TC04284A.

[146] G. Wisz, I. Virt, P. Sagan, P. Potera, and R. Yavorskyi, ‘Structural, Optical and Electrical Properties of Zinc Oxide Layers Produced by Pulsed Laser Deposition Method’, *Nanoscale Res Lett*, vol. 12, no. 1, p. 253, Dec. 2017, doi: 10.1186/s11671-017-2033-9.

[147] V. S. Kulkarni and C. Shaw, ‘Surfactants, Lipids, and Surface Chemistry’, in *Essential Chemistry for Formulators of Semisolid and Liquid Dosages*, Elsevier, 2016, pp. 5–19. doi: 10.1016/B978-0-12-801024-2.00002-9.

[148] H. Dong, W. Liu, Y. Li, X. Chen, and D. Wang, ‘Fully Printed Flexible Zinc Oxide Patch for Wearable UV Light Sensing’, *Advanced Electronic Materials*, vol. 9, no. 12, p. 2300469, 2023, doi: 10.1002/aelm.202300469.

[149] T. Tian *et al.*, ‘Unraveling the Morphology-Function Correlation of Mesoporous ZnO Films upon Water Exposure’, *Advanced Functional Materials*, vol. 34, no. 8, p. 2311793, 2024, doi: 10.1002/adfm.202311793.

[150] X. Wang, T. Sun, H. Zhu, T. Han, J. Wang, and H. Dai, ‘Roles of pH, cation valence, and ionic strength in the stability and aggregation behavior of zinc oxide nanoparticles’, *Journal of Environmental Management*, vol. 267, p. 110656, Aug. 2020, doi: 10.1016/j.jenvman.2020.110656.

[151] T. Mori, J. Ida, S. Momose, K. Itoh, K. Ishibashi, and Y. Arai, ‘Diode Characteristics of a Super-Steep Subthreshold Slope PN-Body Tied SOI-FET for Energy Harvesting Applications’, *IEEE Journal of the Electron Devices Society*, vol. 6, pp. 565–570, 2018, doi: 10.1109/JEDS.2018.2824344.

[152] S. M. Al-Hilli, R. T. Al-Mofarji, and M. Willander, ‘Zinc oxide nanorod for intracellular pH sensing’, *Applied Physics Letters*, vol. 89, no. 17, p. 173119, Oct. 2006, doi: 10.1063/1.2367662.

[153] B. D. Boruah, ‘Zinc oxide ultraviolet photodetectors: rapid progress from conventional to self-powered photodetectors’, *Nanoscale Adv.*, vol. 1, no. 6, pp. 2059–2085, Jun. 2019, doi: 10.1039/C9NA00130A.

[154] F. Verbakel, S. C. J. Meskers, and R. A. J. Janssen, ‘Electronic memory effects in diodes from a zinc oxide nanoparticle-polystyrene hybrid material’, *Applied Physics Letters*, vol. 89, no. 10, p. 102103, Sep. 2006, doi: 10.1063/1.2345612.

[155] C. Li, G. J. Beirne, G. Kamita, G. Lakhwani, J. Wang, and N. C. Greenham, ‘Probing the switching mechanism in ZnO nanoparticle memristors’, *Journal of Applied Physics*, vol. 116, no. 11, p. 114501, Sep. 2014, doi: 10.1063/1.4894823.

[156] J. Wang, B. Sun, F. Gao, and N. C. Greenham, ‘Memristive devices based on solution-processed ZnO nanocrystals’, *physica status solidi (a)*, vol. 207, no. 2, pp. 484–487, 2010, doi: 10.1002/pssa.200925467.

[157] K. G. Akpomie *et al.*, ‘Adsorption mechanism and modeling of radionuclides and heavy metals onto ZnO nanoparticles: a review’, *Appl Water Sci*, vol. 13, no. 1, p. 20, Nov. 2022, doi: 10.1007/s13201-022-01827-9.

[158] A. K. Singh, ‘Nanoparticle Ecotoxicology’, in *Engineered Nanoparticles*, Elsevier, 2016, pp. 343–450. doi: 10.1016/B978-0-12-801406-6.00008-X.

[159] Y. Sato, K. Takai, and T. Enoki, ‘Electrically Controlled Adsorption of Oxygen in Bilayer Graphene Devices’, *Nano Lett.*, vol. 11, no. 8, pp. 3468–3475, Aug. 2011, doi: 10.1021/nl202002p.

[160] J.-H. Chen, C. Jang, S. Adam, M. S. Fuhrer, E. D. Williams, and M. Ishigami, ‘Charged-impurity scattering in graphene’, *Nature Phys*, vol. 4, no. 5, pp. 377–381, May 2008, doi: 10.1038/nphys935.

[161] N. E. Courtier, ‘Interpreting Ideality Factors for Planar Perovskite Solar Cells: Ectypal Diode Theory for Steady-State Operation’, *Phys. Rev. Appl.*, vol. 14, no. 2, p. 024031, Aug. 2020, doi: 10.1103/PhysRevApplied.14.024031.

[162] S. A. Marye, X.-Y. Tsai, R. R. Kumar, F.-G. Tarntair, R. H. Horng, and N. Tumilty, ‘A hBN/Ga2O3 pn junction diode’, *Sci Rep*, vol. 14, no. 1, p. 23484, Oct. 2024, doi: 10.1038/s41598-024-73931-6.